NUMERICAL INVESTIGATION OF EDGE-TONES IN HIGH SPEED JETS

BY

MOHAMED YUNUS MOHAMED ISMAIL

A Thesis Presented to the

DEANSHIP OF GRADUATE STUDIES

KING FAHD UNIVERSITY OF PETROLEUM & MINERALS

DHAHRAN, SAUDI ARABIA

In Partial Fulfillment of the
Requirements for the Degree of

MASTER OF SCIENCE

In

AEROSPACE ENGINEERING

MAY 2014

KING FAHD UNIVERSITY OF PETROLEUM & MINERALS

DHAHRAN- 31261, SAUDI ARABIA

DEANSHIP OF GRADUATE STUDIES

This thesis, written by **MOHAMED YUNUS MOHAMED ISMAIL** under the direction of his thesis advisor and approved by his thesis committee, has been presented and accepted by the Dean of Graduate Studies, in partial fulfillment of the requirements for the degree of **MASTER OF SCIENCE IN AEROSPACE ENGINEERING.**

Dr. Mohammed Khalil Ibrahim (Advisor)

Dr. Ahmed Zafar Al-Garni (Co-Advisor)

Dr. Wael AbdelRahman (Member)

Dr. Esmail M.A. Mokheimer (Member)

Dr. Ahmet Z. Sahin (Member)

Dr. Ahmed Zafar Al-Garni
Department Chairman

Dr. Salam A. Zummo
Dean of Graduate Studies

12/11/14
Date

In The Name of Allah
The Most Beneficent and Most Merciful

To

My Beloved Parents and Sisters

for their

Innumerable Prayers, Motivation and Patience

ACKNOWLEDGMENT

IN THE NAME OF ALLAH, THE MOST BENEFICIENT AND THE MOST MERCIFUL

"So high (above all) is Allah, the Sovereign, the Truth. And, [O Muhammad], do not hasten with [recitation of] the Qur'an before its revelation is completed to you, and say, "My Lord, increase me in knowledge." ***(Surah 20: At'Taha, 114)***

All praises belong to Allah (swt), the Cherisher and Sustainer of the worlds, none is worthy of worship but Him. Peace and blessings of Allah (swt) always be upon our beloved prophet, Muhammad, his family and his companions. I am truly grateful to Allah (swt) for His unbounded blessings always on me and all the members of my family. He is with me in the most difficult of times and always.

I am thankful to King Fahd University of Petroleum and Minerals, for providing a great environment for research. I would like to express my profound gratitude and appreciation to my Advisor Dr. Mohammed Khalil Ibrahim, for his consistent help, guidance, motivation, and attention that he devoted throughout the course of this work. Special thanks to his indigenous discussion over edge-tone and its features.

My sincere and cordial thanks go to Dr. Ahmed Zafar Al-Garni, my Co-Advisor and Chairman of Aerospace Engineering Department. His valuable suggestions, encouragement and useful discussions made this work interesting to me.

Special and sincere thanks also go to my thesis committee members Dr. Wael G. Abdelrahman, Dr. Ahmet Sahin, and Dr. Esmail Mokheimer for their interest, cooperation and constructive advice.

I would also like to acknowledge all AE faculty members, who are involved with my M.S course work. Their knowledge and experience guided me to secure this degree in a very professional manner. I also owe thanks and recognition to my fellow research assistants, course mates, colleagues and friends for their help, motivation and support. Also, I would like to thank Deanship of Research, KFUPM for partially supporting this research work.

Last but not the least; I would like to thank my Parents and Sisters for their innumerable prayers, unconditional love and support. They stood by me in my most difficult of times, and no words of appreciation can fully express my gratitude towards them. So I dedicate this work to my beloved parents and sisters, without their love, affection and encouragement this work would not have been possible. I also thank my brothers-in-law for their support. I pray to Allah (swt) to give us all Guidance and Pardon our sins and grant us Paradise. Ameen.

TABLE OF CONTENTS

LIST OF TABLES

LIST OF FIGURES

NOMENCLATURE

A	surface area *in* (m^2)
C_μ	realizable k-ε model coefficient
E	total energy per unit volume *in* (J/m^3)
G_k	generation of turbulent kinetic energy due to the mean velocity gradients
H	total enthalpy *in (joule)*
$H(f)$	Heaviside function
I	sound intensity *in* (W/m^2)
$\bar{\bar{I}}$	unit tensor
K	wave number
M	Mach number $(=U_0/c)$
M_c	convective Mach number $(=U_c/c)$
Mj	averaged jet Mach number $(=U_j/c)$
Mj_{max}	maximum jet Mach number $(=U_{jmax}/c)$
P_c	interior cell pressure *in* (N/m^2)
P_e	static pressure *in* (N/m^2)
P_f	face pressure *in* (N/m^2)
Q	heat transfer rate *in (W)*
Q''	heat flux *in* (W/m^2)
R	half of the slit width or radius of jet *in (m)*
Re	Reynolds number = $\rho V d/\mu$
S	modulus of average rate of strain tensor
St	Strouhal number
T	temperature *in (K)*
T_{ij}	Lighthill's stress tensor
T_1	downstream time while jet disturbance is carried from slit to edge *in (s)*

T_2	upstream time while acoustic wave is propagated from slit to edge *in (s)*
T_{LOOP}	total feedback-loop time *(T_1+T_2) in (s)*
U	conservative variables
U_0	main jet velocity *in (m/s)*
Uc	jet disturbance convective speed *in (m/s)*
Uj	averaged jet velocity *in (m/s)*
Uj_{max}	maximum jet velocity *in (m/s)*
Us	secondary flow velocity *in (m/s)*
V	velocity *in (m/s)*
V_n	normal velocity *in (m/s)*
Z	acoustic impedance *in ($N.s/m^2$)*
c	speed of sound *in (m/s)*
d	jet slit width or diameter of the jet *in (m)*
e	internal energy *in (J)*
f	edge-tone frequency *in (Hz)*
$\vec{f}_e$	external volume forces
f_{max}	high frequency end of sound spectrum *in (Hz)*
h	stand-off distance *in (m)*
h_0	minimum stand-off distance to create minimum breadth *in (m)*
k	turbulent kinetic energy
l_t	central insertion tube length *in (m)*
$\dot{m}$	mass flow rate *in (kg/s)*
n	stage number
$\hat{n}$	unit normal
p	phase lag
$\dot{q}$	volumetric heat addition per unit mass
r	local point radius, *in (m)*
t_{nl}	nozzle lip thickness *in (m*)
t_{180}	length of flat plate *in (m*)

u	velocity component in x direction
$\bar{u}$	time average velocity component in x direction
u'	fluctuating velocity component in x direction
u_i	fluid velocity component in the x_i direction
u_n	fluid velocity component normal to the surface, $f = 0$
v_i	surface velocity component in the x_i direction
v_n	surface velocity component normal to the surface, $f = 0$

Symbols

Λ	downstream propagation wavelength
λ	upstream propagation wavelength
ρ	density *in* (kg/m^3)
μ	coefficient of viscosity *in (kg/m-s)*
μ_t	eddy viscosity *in (kg/m-s)*
ε	dissipation rate
$\bar{\bar{\tau}}$	viscous shear stress tensor
ν	control volume *in* (m^3)
κ	thermal conductivity *in (W/mK)*
$\Delta(f)$	Dirac delta function
ϕ	angle of wedge *in (deg)*
θ	momentum thickness of jet free shear layer non-dimensionalized by half of the slit width.
σ_{ij}	viscous stress tensor
σ_2	non-dimensional wave number of hydrodynamic disturbances of vortices
$\overline{\Omega_{ij}}$	mean rate of rotation tensor
ω	angular frequency, $\omega = 2\pi f$ *(rad/s)*

Abbreviations

CE/SE	Conservation Element/Solution Element method
CFD	Computational Fluid Dynamics
CPU	Central Processing Unit
DNS	Direct Numerical Simulation
FFT	Fast Fourier Transform
LES	Large Eddy Simulation
MFI	Mass Flow Inlet
NLT	Nozzle Lip Thickness
RHS	Right Hand Side
SPL	Sound Pressure Level *in (dB)*
USA	Unified Solutions Algorithm

THESIS ABSTRACT (ENGLISH)

NAME: MOHAMED YUNUS MOHAMED ISMAIL

TITLE: NUMERICAL INVESTIGATION OF EDGE-TONES IN HIGH SPEED JETS

MAJOR: AEROSPACE ENGINEERING

DATE: MAY 2014

This thesis involves the numerical investigation of edge-tones generated due to high speed jet-edge interactions. 2-D, compressible, unsteady Navier-Stokes commercial CFD code, Fluent, is utilized. Ffowcs-Williams and Hawkings method is used to examine the acoustic data. The results of both laminar and realizable k-ε turbulent flow models predicated the edge-tone frequency fairly well despite the reduction in SPLs for turbulent flow which is attributed to mixing. Since turbulence effect is small on edge-tone frequency and due to the high computational cost associated with the turbulent flows, the parametric study is conducted using the laminar flow model. The effects of Mach number, jet profile, edge shape and nozzle lip are investigated. Compressibility effects are investigated by increasing the Mach number of jet exit to high subsonic level. Results indicate that the edge-tone frequency increases as with increasing Mach number or the angle of wedge and it decreases while nozzle lip thickness increases. Amplitude of the edge-tone increases as with increasing Mach number or the nozzle lip thickness and it decreases as angle of wedge increases. Momentum thickness of jet shear layer has been investigated in depth to find the phase lag value, *p*, for high subsonic speed jets. For high subsonic speed p is found out to be -0.1. The minimum breadth is also analyzed and

value of static pressure time derivative on wedge surface is higher during edge-tone emission and lower for stand-off distance less than or equal the minimum breadth region. The results also indicate that in the minimum breadth region, vortices did not interact with wedge tip that resulted in disappearance of the edge-tone. Feedback loop path study showed that upstream propagation path lies outside the jet. A method is proposed for edge-tone suppression using a central insertion tube with and without lateral microjet injection. The case without microjet injection suppressed edge-tone if the central tube length, $d/l_{t,}$, is greater than or equal 30 percent of stand-off distance. This suppression in edge tone is attributed to the weakness in the interactions between the shear layers at the nozzle exit due to the central tube. That leads to weakening of feedback loop which result in the suppression of edge-tone amplitude. Using this passive control approach the edge-tone amplitude is reduced up to 17 dB when a central insertion tube without injection of length, $d/l_t = 0.375$, is inserted into the jet plume having Mach number of 0.87.

THESIS ABSTRACT (ARABIC)

الاسم : محمد يونس محمد اسماعيل

العنوان : دراسة حسابية لنغمات الحافة الصادرة من النفاثات عالية السرعة

التخصص : هندسة الطيران والفضاء

التاريخ : مايو 2014

تقدم هذه الرساله دراسة حسابية لظاهرة النغمة الصوتية الناتجة عند اصطدام نفاث هوائي ذو سرعة عالية تحت الصوتية بجسم صلب ذو حافة حادة و لذلك تسمى "النغمة الحافية" و تمت الدراسة باستخدام برنامج تجاري لدراسة ديناميكا الموائع بالطرق الحسابية و الذي يقوم على حل معادلات ثنائية الابعاد لنفير و استوكس الغير مستقرة والانضغاطية و اللزجة و تم استخدام طريقة فوكس و يليمز هوكينج لحساب النتائج الصوتية عند نقاط محددة في النطاق الحسابي. كما تمت الحسابات لكل من السريان الصفحي والسريان المضطرب وأظهرت النتائج صدور النغمة في الحالتين وبنفس التردد تقريبا مع اختلاف في السعة او المقدار حيث كانت اكثر مقدارا في حالة السريان الصفحي عنها للسريان المضطرب و ربما يرجع هذا لظاهرة الخلط المصاحبة للسريان المضطرب و الذي بدورة يؤدي الي تخفيض في الضوضاء المنبعثة. و بسبب التأثير الضعيف للسريان المضطرب على التردد و كذلك التكلفة الحسابية العالية المطلوبة له تمت معظم الحسابات في هذه الدراسة باستخدام نموذج السريان الصفحي و تمت دراسة تأثير بعض المتغيرات على تردد و مقدار النغمة الصادرة مثل رقم ماخ و هو الذي يحدد سرعة النفاث و كذلك زاوية الحرف الصلب و سمك جدار البوق الذي ينبعث منه النفاث و سمك الطبقة الجدارية للنفاث و أظهرت النتائج ان تردد النغمة يزداد بزيادة رقم ماخ و كذلك بزيادة زاوية الحرف الصلب و ينخفض التردد بزيادة سمك البوق الذي ينبعث منة النفاث. كما ان مقدار النغمة يزداد بزيادة رقم ماخ و سمك جدار البوق الذي ينبعث منة النفاث و يقل بزيادة زاوية الحرف الصلب. و أظهرت أيضا النتائج الحسابية ان مقدار تأخر الحالة المعرف بالـ Phase Lag في حدود -0.1 و هي قيمة اكبر من القيم المنشورة بالأبحاث المشابهة. كما تم دراسة مجال الدفق للحالات التي كان وضع الحافة فيها مقارب لوضع الحافة عند اختفاء النغمة و الذي تسمي فيه المسافة بين الحافة و بوق خروج النفاث بمسافة الحد الأدنى او ما يعرف بالـ Minimum Breadth ووجد ان الدوامات الصادرة من النفاث لا تصطدم بالحافة في حالة اختفاء

النغمة كما وجد ان معدل تغير الضغط على سطح الحافة ينخفض عند الحافة الصلبة عند اختفاء النغمة عنها في حالة صدور النغمة. وأيضا تمت دراسة اذا ما كنت الموجات الصادرة عن تفاعل النفاث مع الحرف الصلب تنتشر داخل النفاث او خارجه و أظهرت النتائج انها تنتشر خارجه. و في نهاية الرسالة تم اقتراح طريقة لتخفيض الضوضاء الصادر عن النغمة الحرفية و ذلك باستخدام أنبوب مثبت داخل مركز البوق و ممتد لمسافة محددة داخل النفاث و يصدر من نهاية الانبوب نفاثين متناهي الصغر عموديين على اتجاه السريان للنفاث الرئيسي و تمت دراسة تأثير سرعة هذين النفاثين متناهي الصغر و كذلك طول الانبوب الممتد داخل النفاث على مقدار التخفيض في ضوضاء النغمة. و أظهرت النتائج ان النغمة تبدأ في الاختفاء اذا كان طول الانبوب المركزي اكبر من 30% من طول المسافة بين خروج النفاث و الحافة الصلبة في حاله عدم انبعاث النفاثين متناهي الصغر كما أظهرت النتائج ايضا ان التخفيض يصل اقصاة في حالة طول الانبوب المركزي مساوي لـ 2.67 من عرض النفاث و الذي يصل لـ -17 ديسيبل و ذلك لنفاث رئيسي بسرعة ماخ 0.87

CHAPTER 1

INTRODUCTION

1.1 Overview

In modern aviation industry, every day, many commercial aircrafts take-off and land at different countries across the globe, along with undesirable noise pollution to the nearby communities. The noises produced by aircraft components e.g. wings, slats, flaps, and landing gear, etc. are some of the vital sources of sound. Even in fighter / bomber weapons bays, at moderate high speeds, open cavities produce undesirable noises, which can lead to the structural fatigue of internally carried weapons, their suspension equipment, and the structural loads on the parent aircraft [1]. These types of flow-induced noises are also present in transonic wind tunnels, slotted flumes, high-head gates, velocity probes and pressure probes.

1.2 Self-Sustained Oscillations

Andronow *et.al* [2] defined the self-sustained oscillation as “a self-oscillatory system as one that generates a periodic process from a non-periodic source”. Stoker [3] includes the oscillations from the flutter of aircraft wings in the class of self-sustained oscillations since the vibration results through partial conversion of energy from a steady-flow into oscillations. Self-sustained shear oscillations are found in various shear layer impingement configurations, which are responsible for the flow-induced noise and

vibration. It results in unwanted structural loading, and appears in a range of applications, which involves transonic wind tunnels [4], aircraft components [5], slotted flumes [5], high-head gates [5], velocity probes [6] and pressure probes [7]. Flow induced noise sources are one of the complicated flows, which are challenging to simulate.

1.3 Edge-tone Phenomenon

Edge-tone, a typical phenomenon of these self-sustained shear oscillations, is generated when a jet impinges on an edge or the sharp edge corner of a wedge. When the free shear layer near the nozzle lip is excited, a disturbance is initiated and convected downstream and amplified, if the disturbance is unstable, it forms into organized vortices [8]. When these vortices impinge on the edge, pressure waves are generated and propagate upstream to the nozzle lip to produce another disturbance near the nozzle lip. The upstream propagating sound and the downstream convected disturbances constitute a feedback loop. Fig. 1-1 shows the schematic of edge-tone feedback system in which Λ is the downstream propagating wavelength and λ is the upstream propagating wavelength.

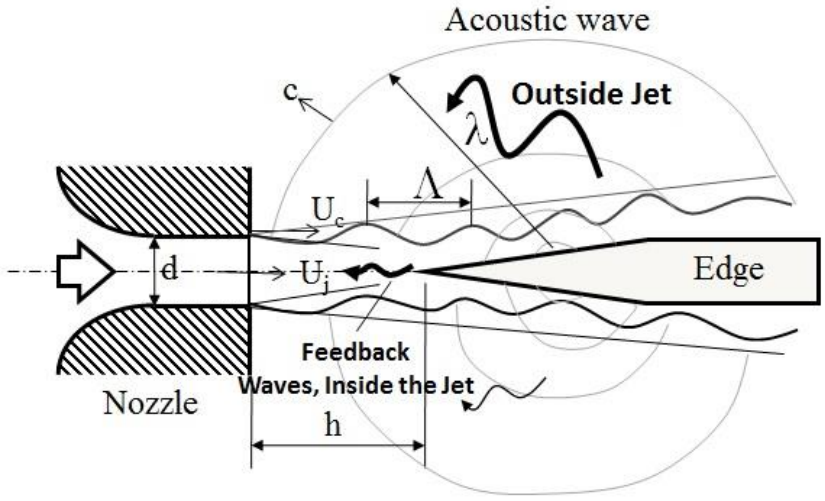

Figure 1-1: Jet-edge impingement system [9]

It is vital to understand the edge-tone mechanism and frequency characteristics from the engineering point of view to propose a flow control technique to suppress edge-tones. Brown [10] revealed many of the important characteristics of edge-tone. The peak amplitude at specific frequency is known as the edge-tone and the associated frequency is known as the edge-tone frequency. Edge-tone frequency changes gradually but sometimes drastically, when the impinging jet velocity or the stand-off distance increased to particular values at which there is a sudden marked irregularity in the vortex pattern which is responsible for the staging. The unexpected alteration of frequency is known as "frequency jump" or "staging phenomenon". These stages are termed as stage 1, 2, 3, and 4 in the order of increasing frequencies and its Strouhal number based on slit width are 0.1, 0.2, 0.3 and 0.4, respectively [10]. The slit width of Brown's experimental data is 1 mm and the jet velocity is 17.5 m/s.

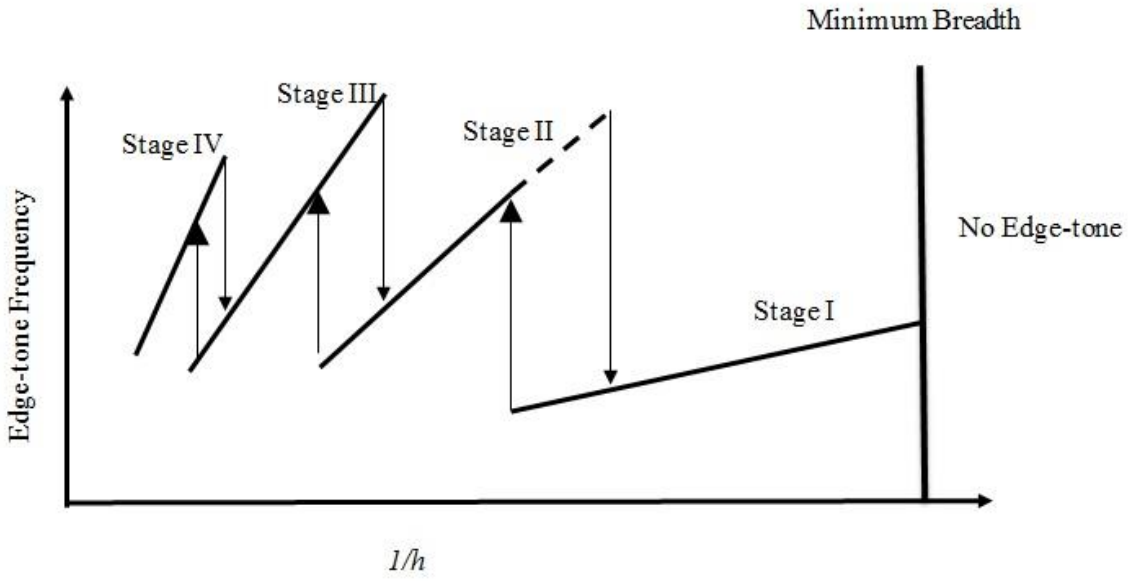

Figure 1-2: Staging phenomenon from Brown's experiment [10]

Four stages are observed in Brown's experiments (stages 1, 2, 3, and 4) as shown in Fig. 1-2. Stage number increased when the Reynolds number of the flow, jet velocity or the

stand-off distance increased. His results showed the hysteresis effects and tonal jumps at specific stand-off distances. Since edge-tone is a loud noise with high amplitude which could lead to structural damage, it is vital to understand the phenomenon to propose a flow control technique to suppress it.

1.4 Powell's Theory

Phase-lock principle determines the edge-tone frequency that states the sum of the time required for the instability waves to travel downstream (from exit of the nozzle to the wedge or wall) and the time required for the feedback acoustic waves to travel upstream (from the wedge or wall to the exit of the nozzle) should be equivalent to a total number of the period of oscillations [11, 12]. Based on this theory, a relation for the edge-tone frequency can be written as follows [9]

$$\frac{h}{\Lambda}+\frac{h}{\lambda}=n \qquad n = 1, 2, 3, ... \tag{1.1}$$

where h is the stand-off distance between the nozzle exit and wedge tip. Λ and λ are the wavelengths of instability waves traveling downstream and upstream, respectively as shown in Fig. 1-1. n is the stage number. One of the important features of edge-tone is the 'minimum breadth', which is the minimum distance needed for the generation of first edge-tone. Krothapalli *et al.* [13] studied the variation of minimum breadth with the jet velocity from low to high subsonic speeds. The reason behind the occurrence of minimum breadth is investigated in this present study.

1.5 Problem Statement

It is essential to note that self-sustained shear layer oscillations are responsible for flow-induced noise. It results in unwanted structural loading, and appears in various applications, which include transonic wind tunnels, aircraft components, slotted flumes, high-head gates, velocity probes and pressure probes. Thus, with respect to the noise suppression, it is vital to know the physics of it production and propagation. Edge-tone phenomenon is one of the fundamental aero-acoustics problems that still need to be understood in depth. The present study is focused on the edge-tone phenomenon by investigating its generation, the staging phenomena and proposing a technique to suppress the high edge-tone amplitude.

1.6 Objective of this thesis

The objectives of the study can be summarized as follows:

a. Study and validate the 2-D computational results with the available published experimental results of a well-known edge-tone flow-field that occurs when a wedge shaped object (traditionally called edge) impinges a plane free jet.
b. Study the effect of compressibility on edge-tone generation, momentum thickness of shear layer, wedge angle, and nozzle lip thickness on edge-tone generation and the staging phenomena. The flow-field of the jet-edge system with stand-off distance less than, equal and greater than the minimum breadth is examined and characterized.
c. Theoretically comparing the computed edge-tone frequencies to the Powell's feedback loop prediction formula and identify whether the upstream propagating

waves are inside or outside the jet.

d. Propose a flow control technique to suppress the edge-tone.

1.7 Methodology

In the numerical simulations, two-dimensional unsteady compressible flow for high speeds ($0.3<M<0.9$) are considered pertinent to a jet impingement on the edge (sharp corner of a wedge). The governing equations of flow and acoustical source data are solved numerically through employing a control volume approach. Fluent CFD code is used to model the flow-field that impinges on the edge and conduct acoustic model simulations. Fluent resolves the Reynolds-averaged Navier-Stokes (RANS) equations, which represents the governing equations for fluid flow, using a finite volume method. The validation of high speed edge-tones is conducted using the compressible laminar model and realizable k-ε turbulence model in FLUENT and compared with the experimental results reported by Krothapalli *et al.* [13].

1.8 Organization of Thesis

This thesis is categorized into 6 chapters. Following this introductory part is chapter 2, which presents the literature review that reports the edge-tone phenomenon and its different features from various and up to date experimental and numerical investigations. Chapter 3 illustrates the basic physics and presents the governing equations used in the present study for laminar flow and turbulent flow as well as the acoustic model. Chapter 4 presents the numerical modeling of various cases developed for simulation in this study. It also contains details about grid generation and the type of grids used for

computations. Chapter 5 presents the results and discussion of simulations. It starts with the validation of high speed edge-tone cases and their staging phenomenon as well as the effect of parameters like compressibility, wedge angle, shears layer thickness, nozzle lip thickness. The flow-field of the jet-edge system with stand-off distance less than, equal and greater than the minimum breadth are examined and characterized. Acoustic feedback loop path also clarified in this chapter too. Suppression concept for the edge-tone is presented and examined in the same chapter. Chapter 6 outlines the conclusion drawn from this research with recommendations for future study.

CHAPTER 2

LITERATURE REVIEW

Understanding the mechanism of edge-tones has been a long standing dilemma in the aero-acoustic and musical acoustic fields and details of edge-tone phenomenon are not totally explained yet. Nevertheless, its characteristics have been obtained by empirical equations based on experimental observations. In this chapter, literature survey of edge-tones is reported. The first primary work is carried by Brown [10], who presented the empirical equation for the frequency of edge-tone as follows:

$$f = 0.466\, j(U - 40)(1/h - 0.07) \tag{2.1}$$

Where f is the frequency in *Hz*, U is the speed of jet in *m/s* and h is the distance between the jet exit and the edge in meters *(m)*. The number j is taken as j=1.0, 2.3, 3.8, 5.4, for stages 1, 2, 3, 4 respectively. For j=1, it means the first stage frequencies and others mean overtones. When jet velocity and stand-off distance are increased the first stage oscillation is excited and its frequency increased gradually until certain stand-off distance then jump to other stage occurs. Brown [10] observed also that the transitions between stages are unstable.

Lighthill [14] conducted research about aerodynamic sound generated by turbulent flows and gave an exact mathematical form for the source of aerodynamic sound. Lighthill

exactly transformed the set of fundamental equations, Navier-Stokes and continuity equations, to an inhomogeneous wave equation in which the source is denoted by the inhomogeneous term at the Right Hand Side (RHS) of the Eq. (2.2):

$$\left(\frac{\partial^2}{\partial t^2} - c_0^2 \nabla^2\right)(\rho - \rho_0) = \frac{\partial^2 T_{ij}}{\partial x_i \partial x_j} \tag{2.2}$$

where the tensor T_{ij} is known as Lighthill's tensor and is determined by

$$T_{ij} = \rho v_i v_j + ((p - p_0) - c_0^2(\rho - \rho_0))\delta ij + \sigma ij \tag{2.3}$$

Here, c_0 is the sound speed in a stagnant acoustic medium, p is the pressure of air with the average p_0, ρ is the density of air with the average ρ_0, and σ_{ij} is the viscous stress tensor. It is considered that the quadrupole source distribution in turbulence produces the sound wave provided by the inhomogeneous term in Right Hand Side (RHS) of Eq. (2.2) and propagates like that in the stagnant acoustic medium, despite of turbulence existence. This comprehension is known as Lighthill's acoustic analogy. Thus the RHS of Eq. (2.2) can be calculated from the result of CFD simulation and the sound propagation can be simulated with an acoustic solver separately from the CFD simulations. Ffowcs-Williams and Hawkings (FWH) acoustic solver (with Lighthill's acoustic analogy) is used in this study for the computational aero-acoustic simulations of the edge-tone. Lighthill's analogy is initially developed for free flows due to unheated jet engines only. FWH analogy is an extended version of Lighthill's analogy which can be applied for bounded shear flows. It considers the effect of solid boundaries by calculating the source

distribution of surface monopole and surface dipole. Hence it is developed from the same assumptions of Lighthill's analogy [15]. An acoustic monopole is a source that radiates sound equally in all directions at same phase. Two monopoles of equal source strength, but opposite phase and separated by a small distance comprise an acoustic dipole. Two identical dipoles, with opposite phase and separated by small distance comprise a quadrupole.

Powell [12] constructed a feedback loop equation predicting the frequency of the edge-tone as follows:

$$f = \frac{n+p}{T_{loop}} = \frac{n+p}{T_1 + T_2} \tag{2.4}$$

where f is the edge-tone frequency, n is the stage number, p is the phase lag which is the amount of phase difference between the upstream and downstream propagation, T_{loop} is the total duration of the feedback loop, T_1 is the time required for the jet to propagate from nozzle exit to the edge, and T_2 is the time required for the acoustic wave to propagate from the edge to nozzle exit, which are defined as follows:

$$T_1 = \int_0^h \frac{dx}{U_c} \text{ and } T_2 = \frac{h}{c} \tag{2.5}$$

where U_c is the jet disturbance convective velocity at the jet center, h is the stand-off distance, and c is the sound speed. Based on theoretical considerations, Powell made three assumptions for the practical use of Eq. (2.4)

1. T_2 is small since speed of sound is much greater than the convective speed of jet disturbance.
2. Convective speed of jet disturbance is constant ($U_c \approx \frac{1}{2}U_j$ from [16, 17]).
3. The phase lag *(p)* is constant with a value of 0.25.

The frequency predicted by Powell's feedback loop equation, Eq. (2.4), with the above assumptions agreed well with the experimental data of Brown [10].

After Lighthill's paper was published, several authors pursued the physical meaning of Lighthill's acoustic analogy for the jet-edge system. Powell [18] indicated the role of vorticity as a sound source with reduced Lighthill's source term. He considered a circular cylinder as edge with diameter less than the slit width (i.e., the width of the stream). He observed when jet impinges on the cylinder, vortex is cast off from it and a circulation about the cylinder occurred, its strength being equal and opposite to that of the newly created vortex at jet slit. It is the induced flow due to the vortex pair which disturbs the jet stream just as it leaves the orifice. He indicated the role of vortex shedding as a sound source.

Curle [19] suggested that edge-tones generated due to the periodic production of vortices created at the edge.

Figure 2-1: Hydrodynamic mechanism proposed by Curle [19]

He proposed that edge-tones mechanism is not due to acoustical reason even though it has resonance effect but it is based on hydrodynamic mechanism without taking any account of the compressibility of fluid as depicted in Fig. 2-1. It explains the jet oscillation during the edge-tone generation in the following sequence: (a) Maximum transverse velocity at edge, produced half-way between alternate vortices. (b) Vortex generated as a result of (a). (c) Slight deflection of jet produced by appearance of free vorticity at (b). The release of vortex (generated at the upper edge of the wedge) from the boundary layer will cause a circulation to be produced at large distances according to Kelvin-Helmholtz theorem. So the hydrodynamic disturbances of the vortex sheet grow exponentially along with the distance due to instability characteristics of shear flow. This causes the jet to be deflected slightly towards the upper edge of the slit. (d) Slight additional vorticity appears above, as a result of (c). (e) Regions of additional weak vorticity amplified due to jet disturbance as they move downstream (the growth of vortex indicated by its size in Fig. 2-1. It can be deduced that vortices of opposite circulation are produced simultaneously at the upper edges of the slit and the wedge, and similarly at the

lower edges, and also that the edge-tone wavelength λ and the edge to slit distance *h* are related by the following empirical equation.

$$h = (i + \frac{1}{4})\lambda \tag{2.6}$$

where *i* is an integer and it is suggested that the value of *i* is such that λ is the edge-tone wavelength which gives maximum amplitude. Independently of this, a semi-empirical expression is obtained by Curle for the velocity with which the vortices move along. A formula for the edge-tone frequency can be deduced and written as [19]

$$f = \frac{1}{2}U_0\left(\frac{i+\frac{1}{4}}{h} - \frac{1}{30d}\right) \tag{2.7}$$

where *d* is slit-width in meters. There is a minimum value of *h* below which this formula is not applicable. Because u/U_0, where *u* represents the velocity of downstream propagating vorticity, is based on some experimental values of Brown all of which are at a value of $h > 1\ cm$ i.e. $h > 10d$. So he expected this formula to be applicable only when $h/d > 10$. The predictions based on the above formula are matching well with the published experimental data of Brown [10].

Krothapalli *et al.* [13] investigated experimentally on edge-tones generated by high speed subsonic air jet issuing from a rectangular nozzle and impinging on a wedge shaped edge.

They studied the ‘minimum breadth’, that is the minimum distance needed to produce the edge-tone and stated that it increased linearly for jet exit Mach numbers ranging from 0.2 to 1 while decreased rapidly for lower Mach numbers up to 0.06. They investigated the influence of these edge-tones on the mixing of multiple nearby rectangular jets. They observed the improved mixing of the multiple jets when one of these jets is impinged on a wedge.

Howe [20] reformulated Lighthill’s equation in terms of the total enthalpy (or stagnation enthalpy) *B* defined by

$$B = \int dh + \frac{1}{2}v^2 \tag{2.8}$$

where enthalpy *h* is given by

$$dh = \rho^{-1}dp + Tds \tag{2.9}$$

Then he end up with a well approximated equation for low Mach number and high Reynolds number flows as follows:

$$\frac{1}{\rho c_0^2}\frac{\partial^2}{\partial t^2}p - \nabla^2 B \approx div(\omega \times v) \tag{2.10}$$

This equation indicates that the sound in terms of *B* is generated due to vortices as shown in RHS of Eq. (2.10). This equation is equivalent to the Lighthill’s equation Eq. (2.2) but the sound source is mentioned in terms of vorticity.

Dougherty *et al.* [21] performed numerical investigation of edge-tones at low speeds using Unified Solutions Algorithm (USA) CFD code with first order time and third order spatial accuracy to verify its ability to predict the edge-tone phenomenon. Their numerical results of unsteady flows agreed very well with Brown's experimental data. Detailed analyses of vortex-acoustic coupling, vortex shedding around wedge are analyzed to know the acoustic nature for eight cases of different stand-off distances.

Kwon [8] analyzed the feedback mechanism of low speed edge-tones with the use of jet-edge interaction model where the reaction of edge is modeled as an array of dipoles which are placed about the central plane of the unstable jet. He proposed the maximum pressure point as effective source point which has been found to be within half a wavelength downstream from the edge tip. He found the phase lag (p) to be associated with the effective source point and to be in the range $-0.5 < p < 0$ that agreed well with the experimental data of Powell and Unfried [22].

Ching Y. Loh [23] conducted Direct Numerical Simulation (DNS) to compute blunt trailing edge-tone noises generated by large scale turbulences. Simulations performed using space-time Conservation Element and Solution Element (CE/SE) method. He considered two cases, known as, flow past a circular cylinder (Aeolian noise problem) and flow past a flat plate of finite thickness. Their numerical data matched well with the published experimental data of Hardin [24] and Heinemann [25].

Andreas Bamberger *et al.* [26] studied the 'stage I' edge-tones experimentally and numerically for low speed jets. Their primary interest is to verify the empirical equation stated by Holger *et al.* [27] in terms of Strouhal number

$$S_d = \frac{f.d}{U_0} = C.(d/w)^n \tag{2.11}$$

where exponent n = 3/2. But in contrast, their numerical and experimental results are suggested $n \approx 1$ and a weak dependence of the empirical equation on the Reynolds number is observed.

Devilliers *et al.* [16] carried out experimental and numerical investigation to analyze the importance of gas density in edge-tone phenomenon with injections of three different gases - air, Neon, and CO_2 into the air. They found that the nozzle length (injection duct) has no influence on the results, if the head losses in the nozzle are considered into account which contradicted the published experimental data [28]. They found that if the edge-tone is produced by injecting one gas into another, it could not be recognized anymore as Karman vortex sheet. To examine this issue, they proposed an analogy by comparing the edge-tone instability with Kelvin-Helmholtz instability waves.

Nonomura *et al.* [17, 29, 30, and 31] numerically investigated the edge-tone mechanism using sixth order Pade type compact finite difference scheme and four stage Runge-Kutta scheme for space and time accuracy, respectively. The effects of jet velocity, nozzle lip thickness and jet profile on edge-tone are studied. They observed that thicker nozzle lip has more intensity of edge-tone sound amplitude. It is because thicker nozzle lip

generates strong reflected wave. For the effect of jet profile on the edge-tone generation they concluded that

1) Staging phenomenon is not affected by jet profile but it is affected by average jet velocity.
2) SPL of edge-tone is affected by both average jet velocity and the jet profile.
3) The phase lag $p = -0.2$.

They explained the relation between vortex formations of jet disturbance and edge-tones. They found that thicker boundary layer of jet profile made more intense vortices located near center-line. They proposed that location of vortex is corresponded to the maximum lateral velocity disturbance located on the center line. Phase-lag is decreased when vortex is near to the jet center-axis (near edge) and they proved that phase lag occurred as a consequence of vortex motion.

They also studied the Mach number effects on edge-tone to verify the acoustic wave propagation in order to validate Powell's feedback loop equation Eq. (2.4). When they increased the Mach number of jet, Strouhal number of edge-tone frequency decreased which confirmed Powell's theory. They observed the following phenomena when Mach number increased independently,

1) The edge-tone phenomenon ceases.
2) The edge-tone frequency of same stage turned to reduce.
3) Higher stage is excited.

They calculated phase lag, *p,* of their numerical cases according to Powell's theory and obtained a constant value of -0.2. Their phase lag, *p,* is in the range proposed by Kwon [8] but differed from Powell's constant value of 0.25. They stated that the phase lag, *p,* is

a constant value of -0.2 for wide range of low Reynolds numbers and subsonic jet speed up to Mach number of 0.5.

Paal, G. and Vaik, I [32, 33] performed high accuracy numerical simulations on the edge-tone phenomenon. They found the point of force action (dominant place of acoustic dipole) is in a range of x_F/h = 1.6 to 2 computed from the edge tip, in contrast to the experimental value of x_F/h = 0.25 by Kaykayoglu *et al.* [34] and its location remain stable despite of the changes in Reynolds number and stand-off distance. They also observed the first stage continued to influence even when the second and third stages appeared. They proposed stand-off distance exponent n = 1 in the empirical equation Eq. (2.11) in contrast to the previous literatures (n = 3/2 by Curle [19], Holger *et al.*, [27]). Bamberger *et al.* [26] agreed that n to be 1. They witnessed a quadratic improvement of mean force with the jet exit velocity. They also studied the edge-tones experimentally and numerically for low Reynolds number up to 1400. They compared the experimental edge-tone frequency computed by taking FFT of pressure signal time history with the numerical simulation by *ANSYS CFX* and has good agreement. They also investigated the dependence of edge-tone frequency on the stand-off distance, mean jet velocity and jet profiles (top hat/thin and parabolic).

Vaik, I. *et al.* [35] conducted numerical investigation of edge-tone mechanism using different softwares. They computed flow-field using *ANSYS CFX* and based on Lighthill's analogy sound sources are calculated from the flow-field. Later, an in-house acoustic code is utilized to compute the acoustic field. For coupling of *2-D* flow - *3-D* acoustics, *3-D* sound source regions are computed by extruding the *2-D* flow-field

simulation results using refracted light through a prism. Then, couplings are performed between *2-D* flow - *3-D* acoustics and *3-D* flow - *3-D* acoustics simulations and proved that the approximation of edge-tone flow is *2-D* is true since a negligible disturbances in *z* direction (perpendicular axis to the flat surface of wedge) is observed in *3-D* flow-field.

Recently, Vaik, I. [36] studied the edge-tone experimentally and numerically. He observed the Reynolds number and stand-off distance dependence of the Strouhal number in the case of parabolic and top hat jet-edge-tones. He also studied the staging phenomenon of edge-tone. In staging phenomenon, he studied stage jump (i.e., edge-tone stable jumps from one stage to another) and mode-switching (i.e., unstable jumps). He found that the phase of the jet disturbance between the nozzle and the wedge does not vary linearly with the distance from the nozzle which means that the convection velocity of the jet disturbance is not constant. He proposed a new developed method by which a 2-D CFD simulation can be coupled to a 3-D acoustical simulation. He also studied the well-known edge-tone phenomenon in flue organ pipe. He found that the strongest and most stable edge-tone oscillation occurred in organ pipe foot model (i.e. an flue organ pipe model in which the air leaves the foot of the organ pipe through the flue forming a planar free jet and this jet interacts with the upper lip causing sound), if the upper lip is placed exactly in the centerline of the jet.

Takahashi *et al.* [37] investigated numerically about 2-D and 3-D edge-tones in terms of aerodynamic sound theory with compressible Large Eddy Simulation (LES). They found a significant difference between Lighthill's sound source and Howe's vortex sound

source in terms of shape and strength near the jet flow. This difference occurred because of the difference in formula between the two types of sound sources: Howe's vortex sound theory is based on the perception that the total enthalpy instead of pressure or air density is true sound. Hence the source producing fluctuation of total enthalpy is different from the generating acoustic pressure.

Ibrahim, M.K. [9] studied the edge-tones in high speed jets experimentally and theoretically. He considered fully expanded sonic jet from circular and square nozzles having same hydraulic diameter to impinge on a wedge of 10°, 20°, 60°, and 180° angles. He observed that minimum breadth for small edge angle is approximately half of its 2-D case. He observed upstream propagating neutral acoustic waves of axisymmetric and helical modes as wedge angle increases while at small wedge angles helical mode is dominant. He proposed a semi empirical formula based on his experimental data for small edge angles. According to Eq. (1.1), the upstream propagating waves produced at wedge tip while he assumed that it is produced at a dominant source point found at a distance Δh from the edge tip. He rewrites Eq. (1.1) by considering $h+\Delta h$ instead of h as shown in Eq. (2.12) and agreed very well with his experimental data.

$$f = \frac{(n+p)U_c}{(h+\Delta h)\left(1+\frac{U_c}{a}\right)} \tag{2.12}$$

where Δh is a function in n and h and it can be empirically calculated from the experimental data as in Eq. (2.13)

$$\Delta h = \frac{0.0290n - 5.7500h + 0.0073}{n+6} \tag{2.13}$$

CHAPTER 3

MATHEMATICAL MODEL

3.1 Governing Equations

The governing equations are basically derived from the three fundamental conservation laws.

1. Continuity Equation (Conservation of Mass)
2. Momentum Equation (Conservation of Momentum)
3. Energy Equation (Conservation of Energy)

Velocity vector $\vec{V}$, thermodynamic pressure p and absolute temperature T are the three primary unknowns (*i.e.* five scalar unknowns if the velocity components (*i.e.*, u, v and w) are calculated separately) to be found by solving the above three conservation equations where pressure and temperature are considered to be the two required independent thermodynamic variables. For other thermodynamic variables that present in the final form of conservation equation they are density ρ, enthalpy H, and the two transport properties: viscosity μ and thermal conductivity κ. Additional unknown is solved by adding the equation of state and the assumption of calorifically perfect gas to make the system solvable.

3.1.1 Continuity Equation

The physical principle behind this fundamental equation is mass can neither be created

nor destroyed. This principle is applied to an infinitesimal fluid element inside a fluid as shown in Fig. 3-1. It indicates that the net mass flow out of fluid element is equivalent to the time rate of decrease of mass inside fluid element. Continuity equation in conservation form is written in Eq. (3.1) where ρ is fluid density, t is time and $\vec{V}$ is fluid velocity [38].

$$\frac{\partial \rho}{\partial t} + \frac{\partial \rho u}{\partial x} + \frac{\partial \rho v}{\partial y} + \frac{\partial \rho w}{\partial z} = 0 \tag{3.1}$$

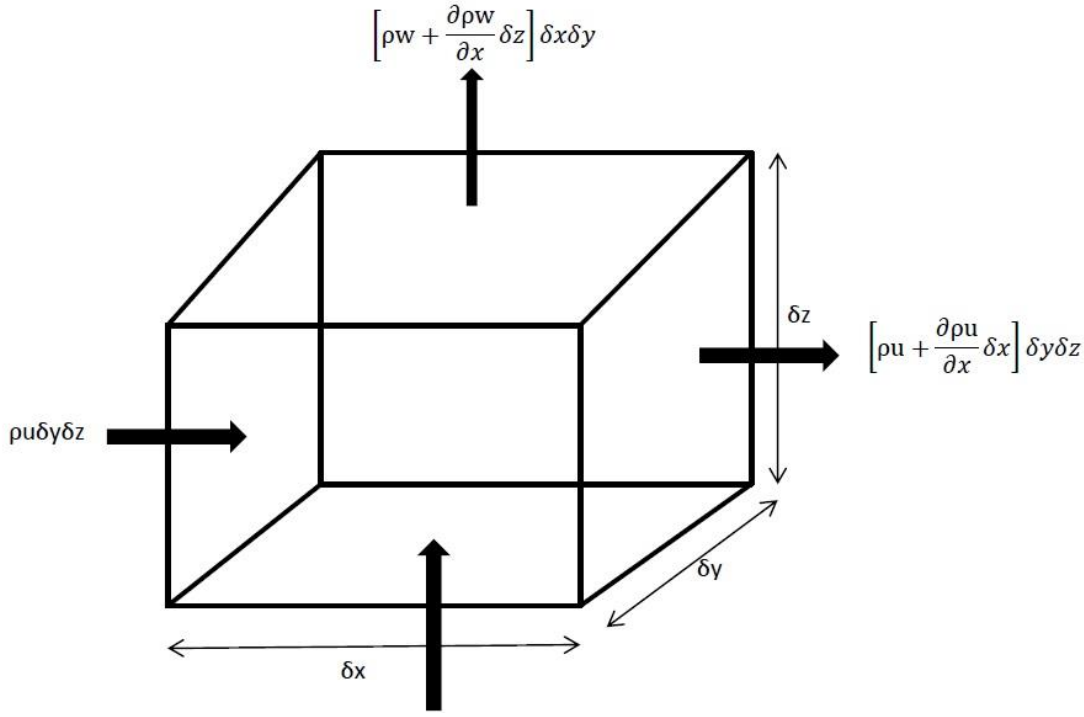

Figure 3-1: Infinitesimal fluid element inside a fluid [39]

3.1.2 Momentum Equation

The physical principle behind this fundamental equation is time rate of change of

momentum is equal to the force exerted on a body. This force comes from two sources:

1) Body forces: gravity, electromagnetic forces, or any other forces that "act at a distance" on the infinitesimal fluid element ν.
2) Surface forces: pressure and shear stress acting on the fluid element *S.*

This principle is applied to the infinitesimal fluid element ν as shown in Fig. 3-1. It indicates that the net force is equal to the sum of net flow of momentum out of fluid element across surface *S* and time rate of change of momentum due to unsteady fluctuations of flow properties inside infinitesimal fluid element ν. Momentum Equation in conservation form is written in Eq. (3.2) to Eq. (3.4) where *u*, *v* and *w* are the velocity components of *x*, *y* and *z*, respectively. τ_{xx}, τ_{yy} and τ_{zz} are normal stress components while τ_{xy}, τ_{xz}, τ_{yx}, τ_{yz}, τ_{zx} and τ_{zy} are shear stress components. f_x, f_y and f_z are the body force components in *x*, *y* and *z* directions respectively [38]. These equations are also known as Navier-Stokes equations.

$$x \text{ momentum: } \frac{\partial(\rho u)}{\partial t} + \nabla.(\rho u \vec{V}) = -\frac{\partial p}{\partial x} + \frac{\partial \tau_{xx}}{\partial x} + \frac{\partial \tau_{yx}}{\partial y} + \frac{\partial \tau_{zx}}{\partial z} + \rho f_x \tag{3.2}$$

$$y \text{ momentum: } \frac{\partial(\rho v)}{\partial t} + \nabla.(\rho v \vec{V}) = -\frac{\partial p}{\partial y} + \frac{\partial \tau_{xy}}{\partial x} + \frac{\partial \tau_{yy}}{\partial y} + \frac{\partial \tau_{zy}}{\partial z} + \rho f_y \tag{3.3}$$

$$z \text{ momentum: } \frac{\partial(\rho w)}{\partial t} + \nabla.(\rho w \vec{V}) = -\frac{\partial p}{\partial z} + \frac{\partial \tau_{xz}}{\partial x} + \frac{\partial \tau_{yz}}{\partial y} + \frac{\partial \tau_{zz}}{\partial z} + \rho f_z \tag{3.4}$$

where

$$\tau_{xx} = \lambda(\nabla.V) + 2\mu \frac{\partial u}{\partial x} \tag{3.5}$$

$$\tau_{yy} = \lambda(\nabla.V) + 2\mu \frac{\partial v}{\partial y} \tag{3.6}$$

$$\tau_{zz} = \lambda(\nabla.V) + 2\mu\frac{\partial w}{\partial z} \tag{3.7}$$

$$\tau_{xy} = \tau_{yx} = \mu\left[\frac{\partial v}{\partial x} + \frac{\partial u}{\partial y}\right] \tag{3.8}$$

$$\tau_{xz} = \tau_{zx} = \mu\left[\frac{\partial u}{\partial z} + \frac{\partial w}{\partial x}\right] \tag{3.9}$$

$$\tau_{yz} = \tau_{zy} = \mu\left[\frac{\partial w}{\partial y} + \frac{\partial v}{\partial z}\right] \tag{3.10}$$

3.1.3 Energy Equation

The physical principle behind this fundamental equation is energy can neither be created nor destroyed; it can only change in form. This principle is applied to the infinitesimal fluid element ν as shown in Fig. 3-1. It indicates that the sum of rate of heat added to fluid inside the infinitesimal fluid element from surroundings and the rate of work done on fluid inside the infinitesimal fluid element is equal to rate of change of energy of fluid as it flows through the infinitesimal fluid element. Energy equation in differential form is written in Eq. (3.11) [38].

$$\frac{\partial}{\partial t}\left[\rho\left(e + \frac{V^2}{2}\right)\right] + \nabla.\left[\rho\left(e + \frac{V^2}{2}\vec{V}\right)\right] = p\dot{q} + \frac{\partial}{\partial x}\left(\kappa\frac{\partial T}{\partial x}\right) + \frac{\partial}{\partial y}\left(\kappa\frac{\partial T}{\partial y}\right) + \frac{\partial}{\partial z}\left(\kappa\frac{\partial T}{\partial z}\right)$$

$$-\frac{\partial(up)}{\partial x} - \frac{\partial(vp)}{\partial y} - \frac{\partial(wp)}{\partial z} + \frac{\partial(u\tau_{xx})}{\partial x} + \frac{\partial(u\tau_{yx})}{\partial y} + \frac{\partial(u\tau_{zx})}{\partial z} + \frac{\partial(v\tau_{xy})}{\partial x} + \frac{\partial(v\tau_{yy})}{\partial y} + \frac{\partial(v\tau_{zy})}{\partial z}$$

$$+\frac{\partial(w\tau_{xz})}{\partial x} + \frac{\partial(w\tau_{yz})}{\partial y} + \frac{\partial(w\tau_{zz})}{\partial z} + \rho\vec{f}.\vec{V} \tag{3.11}$$

Where e is internal energy; $(e+V^2/2)$ is total energy; p is pressure; $\dot{q}$ is the volumetric heat addition per unit mass; κ is thermal conductivity and T is temperature.

3.1.4 Conservative Form of Governing Equations

Equations (3.1), (3.2), (3.3), (3.4) and (3.11) are the full system of governing equations in conservative form which consists of the five basic flow quantities ρ, ρu, ρv, ρw and $\rho(e+V^2)/2$. It can be written in a condensed form as [38]

$$\frac{\partial U}{\partial t}+\frac{\partial F}{\partial x}+\frac{\partial G}{\partial y}+\frac{\partial H}{\partial z}=J \tag{3.12}$$

Where U, F, G, H and J represents the column vectors given by

$$U=\begin{Bmatrix}\rho\\ \rho u\\ \rho v\\ \rho w\\ \rho(e+V^2/2)\end{Bmatrix} \tag{3.13}$$

$$F=\begin{Bmatrix}\rho u\\ \rho u^2+p-\tau_{xx}\\ \rho vu-\tau_{xy}\\ \rho wu-\tau_{xz}\\ \rho(e+V^2/2)u+pu-k\dfrac{\partial T}{\partial x}-u\tau_{xx}-v\tau_{xy}-w\tau_{xz}\end{Bmatrix} \tag{3.14}$$

$$G=\begin{Bmatrix}\rho v\\ \rho uv-\tau_{yx}\\ \rho v^2+p-\tau_{yy}\\ \rho wv-\tau_{yz}\\ \rho(e+V^2/2)v+pv-k\dfrac{\partial T}{\partial y}-u\tau_{yx}-v\tau_{yy}-w\tau_{yz}\end{Bmatrix} \tag{3.15}$$

$$H = \begin{Bmatrix} \rho w \\ \rho uw - \tau_{zx} \\ \rho vw - \tau_{zy} \\ \rho w^2 + p - \tau_{zz} \\ \rho(e + V^2/2)w + pw - k\dfrac{\partial T}{\partial z} - u\tau_{zx} - v\tau_{zy} - w\tau_{zz} \end{Bmatrix} \tag{3.16}$$

$$J = \begin{Bmatrix} 0 \\ \rho f_x \\ \rho f_y \\ \rho f_z \\ \rho(uf_x + vf_y + wf_z) + p\dot{q} \end{Bmatrix} \tag{3.17}$$

Here, *F*, *G* and *H* are called 'flux vectors' and *J* represents 'source vector'. *U* is called the 'solution vector' because the elements in *U* are the dependent variables that can be solved numerically.

3.1.5 Equation of State

In order to relate the flow variables (*p, ρ, T, e, H*) so that the system is closed, the equation of state for perfect gas is utilized

$$p = \rho R T \tag{3.18}$$

where *R* is the gas constant per unit mass. In most of the situations, compressible fluid is considered as perfect gas, even though viscous effects are included. For compressible flow perfect gas [calorically perfect gas (*i.e.*, c_p = c_v = constant)] is considered in computations.

3.2 Laminar Model

When the Reynolds number, *Re*, of the flow is lesser than 2300, it indicates that the flow is laminar. It is a layered flow without any or low level of disturbances or mixing and prone to separation under weak pressure gradients. It has low wall shear stress and low heat transfer. Unsteady, compressible flow is assumed for high speed cases which are typically a turbulent flow. Laminar model in FLUENT solves the basic governing equations mentioned in conservative form in Eq. (3.12). It is clearly evident that the edge-tone phenomenon exists in laminar shear flows [16, 26, 29, and 40]. Hence, the flow can be examined as 2-D and laminar that is persistent with the experimental conditions. The transition to turbulent flow, which is found occasionally in experimental case or existed mostly in high speed, does not affect the initial vortices created on the edge. Hence, turbulence has small importance on both the edge-tone frequency and feedback loop [16]. So, it is expected that the simulation of edge-tone using laminar flow model will match with the experimental data of edge-tone. For compressible flow, energy equation is included while for incompressible flow it is not included. Because ρ is constant in incompressible flow and primary flow-field variable are *p, u, v* and *w*. Equations (3.1) to (3.4) mentioned earlier are four equations in terms of four unknowns *p, u, v* and *w*. So for incompressible flow, continuity and momentum equations are sufficient.

3.3 Reynolds-Averaged Navier-Stokes Equations (RANS)

When turbulent flow is present, the velocity at one point can change as a function of time. So the details of fluctuations are not vital for industrial applications. Their major concern

is on the average flow and the impact of the turbulent fluctuations on the average flow. So, Reynolds-Averaged Navier-Stokes (RANS) equations, which are the time-averaged equations of motion for fluid flow, are introduced to calculate the mean flow. The momentary velocity component is considered as *u*, the time-averaged value is named $\bar{u}$ and the fluctuating velocity has the letter *u'*. From this definition, it can be written as

$u = \bar{u} + u'$; similarly $v = \bar{v} + v'$; $w = \bar{w} + w'$; $p = \bar{p} + p'$; $\rho = \bar{\rho} + \rho'$; $T = \bar{T} + T'$ (3.19)

The selected averaging method calculates the mean values at a fix place in space and averaged over a time span which is large enough for the mean values to be independent of it.

$$\bar{u} = \frac{1}{\Delta t}\int_{t_0}^{t_0+t_1} u dt \tag{3.20}$$

The time-averaged values of the fluctuating components are defined to be zero:

$$\bar{u'} = 0; \bar{v'} = 0; \bar{w'} = 0; \bar{p'} = 0;$$

If the expressions of velocities are substituted from Eq. (3.19) into continuity equation and take time-average as mentioned in Eq. (3.21)

$$\overline{\frac{\partial \bar{u}}{\partial x} + \frac{\partial u'}{\partial x} + \frac{\partial \bar{v}}{\partial y} + \frac{\partial v'}{\partial y} + \frac{\partial \bar{w}}{\partial z} + \frac{\partial w'}{\partial z}} = 0 \tag{3.21}$$

The resulting continuity equation would be

$$\frac{\partial \bar{u}}{\partial x} + \frac{\partial \bar{v}}{\partial y} + \frac{\partial \bar{w}}{\partial z} = 0 \tag{3.22}$$

Similarly if the expressions of velocities, pressure, and temperature are substituted from Eq. (3.19) into Navier-Stokes equations (*i.e.*, Eq. (3.2), (3.3) and (3.4)) and take time-average, the time-averaged Navier-Stokes equation would be

$$\rho\left(\frac{\partial \bar{u}}{\partial t} + \bar{u}\frac{\partial \bar{u}}{\partial x} + \bar{v}\frac{\partial \bar{u}}{\partial y} + \bar{w}\frac{\partial \bar{u}}{\partial z}\right) = F_x - \frac{\partial \bar{p}}{\partial x} + \mu\Delta\bar{u} - \rho\left(\frac{\partial \overline{u'u'}}{\partial x} + \frac{\partial \overline{u'v'}}{\partial y} + \frac{\partial \overline{u'w'}}{\partial z}\right) \tag{3.23}$$

$$\rho\left(\frac{\partial\bar{v}}{\partial t}+\bar{u}\frac{\partial\bar{v}}{\partial x}+\bar{v}\frac{\partial\bar{v}}{\partial y}+\bar{w}\frac{\partial\bar{v}}{\partial z}\right)=F_y-\frac{\partial\bar{p}}{\partial y}+\mu\Delta\bar{v}-\rho\left(\frac{\partial\overline{u'v'}}{\partial x}+\frac{\partial\overline{v'v'}}{\partial y}+\frac{\partial\overline{v'w'}}{\partial z}\right) \quad (3.24)$$

$$\rho\left(\frac{\partial\bar{w}}{\partial t}+\bar{u}\frac{\partial\bar{w}}{\partial x}+\bar{v}\frac{\partial\bar{w}}{\partial y}+\bar{w}\frac{\partial\bar{w}}{\partial z}\right)=F_z-\frac{\partial\bar{p}}{\partial z}+\mu\Delta\bar{w}-\rho\left(\frac{\partial\overline{u'w'}}{\partial x}+\frac{\partial\overline{w'v'}}{\partial y}+\frac{\partial\overline{w'w'}}{\partial z}\right) \quad (3.25)$$

Equations (3.23), (3.24) and (3.25) can be written in tensor form

$$\rho\frac{D\overline{u_i}}{Dt}=F_i-\frac{\partial\bar{p}}{\partial x_i}+\mu\Delta\overline{u_i}-\rho\left(\frac{\partial\overline{u_i'u_j'}}{\partial x_j}\right) \quad (3.26)$$

where Reynolds Stress = $\rho\left(\frac{\partial\overline{u_i'u_j'}}{\partial x_j}\right)$. Equations (3.22), (3.23), (3.24) and (3.25) are known as the Reynolds-Averaged Navier-Stokes (RANS) equations. Reynolds stress is a symmetric tensor and it contains six independent components; three shear stresses, $-\rho u'v'$, $-\rho v'w'$, $-\rho u'w'$ and three normal stresses, $-\rho(u'^2)$, $-\rho(v'^2)$, $-\rho(w'^2)$. Since the equations are not enough to find the unknowns, turbulence models are introduced to solve the Reynolds stress tensor.

3.4 Turbulence Model

When the Reynolds number, *Re*, of the flow is greater than 4000, it indicates the flow is turbulent. In a turbulent flow, the set of governing equations stated above are insufficient due to fluctuating products including Reynolds stresses and fluxes. Hence, the averaged conservation equations have more unknowns in such situations. This deficiency of governing equations is termed as closure problem. Consequently, there is a need for additional equations to solve the closure problem; turbulence modeling provides additional equations to solve the mean flow equations. These additional equations may be based on empirical observations or physical reasoning and therefore, an ideal turbulence model should present less quantity of complexity while observing the significance of physics behind the flow. Many turbulence models exist in literature today. The choice of

the turbulence model relies upon the physics associated with the flow, accuracy level needed and available time and computational resources.

The turbulence models are classified as

1. Algebraic models (Mixing Length, Cebeci-Smith, Baldwin-Lomax, etc.)
2. One-equation models (Wolfstein, Spalart-Allmaras, k-model, etc)
3. Two-equation models (k-ε, k-ω, k-τ, k-L, etc)
4. Stress-transport models (Reynolds Stress Transport Model)

3.4.1 Realizable k-ε turbulence model

In this present study, realizable *k-ε* turbulence model, which is a two-equation model, is used. *k-ε* turbulence model [41] usually differ in the procedure of calculating turbulent viscosity, turbulent Prandtl numbers that governs the turbulent diffusion of *k* and *ε*, and the production and destruction terms in *ε* equation. Traditional *k-ε* models poorly solve the dissipation equation, especially in spreading rate for axisymmetric jets whereas realizable *k-ε* model uses two new formulas in this aspect. A new eddy-viscosity formula and a new model equation for dissipation *ε* are established on dynamic equation of the average square vorticity fluctuation. Realizable *k-ε* model has been broadly investigated for many type of flows, including rotating homogenous shear flows, free flows including jet and mixing layers, channels and boundary layer flows and separated flows [42, 43]. Bousinesq approximation is used in this method to relate the Reynolds stress to the average velocity gradients in order to model the Reynolds stress, $-\rho\overline{u'_i u'_j}$, in the RANS equations .

$$-\rho\overline{u'_i u'_j} = \mu_t\left(\frac{\partial u_i}{\partial x_j} + \frac{\partial u_j}{\partial x_i}\right) - \frac{2}{3}\left(\rho k + \mu_t \frac{\partial u_k}{\partial x_k}\right)\delta_{ij} \qquad (3.27)$$

where, *u(x,t)* represents the velocity vector field. In addition to the Bousinesq approximation, the eddy viscosity can be described by the following equation,

$$\mu_t = \rho C_\mu \frac{k^2}{\epsilon} \tag{3.28}$$

The realizable portion of the k-ε model is based on the following relationship that can be achieved by defining the point where the mean normal stress becomes negative. The realizable k-ε model coefficient, C_μ, is defined at high Reynolds number using equilibrium analysis.

$$\frac{k}{\epsilon}\frac{\partial U}{\partial x} > \frac{1}{3C_\mu} \approx 3.7 \tag{3.29}$$

The realizable k-ε model is described by two equations as follow.

$$\frac{\partial}{\partial x_j}(\rho \epsilon u_j) = \frac{\partial}{\partial x_j}\left[\left(\mu + \frac{\mu_t}{\sigma_\epsilon}\right)\frac{\partial \epsilon}{\partial x_j}\right] - \rho C_2 \frac{\epsilon^2}{k+\sqrt{\vartheta \epsilon}} \tag{3.30}$$

and

$$\frac{\partial}{\partial x_j}(\rho k u_j) = \frac{\partial}{\partial x_j}\left[\left(\mu + \frac{\mu_t}{\sigma_k}\right)\frac{\partial k}{\partial x_j}\right] + G_k - \rho \epsilon \tag{3.31}$$

G_k refers the production of turbulent kinetic energy caused by the average velocity gradients and it depends upon the Boussinesq approximation.

$$G_k = \mu_t S^2 \tag{3.32}$$

where *S* is the modulus of average rate of strain tensor as defined as

$$S = \sqrt{2 S_{ij} S_{ij}} \tag{3.33}$$

and

$$S_{ij} = \frac{1}{2}\left(\frac{\partial u_j}{\partial x_i} + \frac{\partial u_i}{\partial x_j}\right) \tag{3.34}$$

The eddy viscosity variable is defined as

$$C_\mu = \frac{1}{A_0 + A_S \frac{kU^*}{\epsilon}} \tag{3.35}$$

where

$$U^* = \sqrt{S_{ij}S_{ij} + \overline{\Omega_{ij}\Omega_{ij}}} \tag{3.36}$$

and $$\Omega_{ij} = \overline{\Omega_{ij}} - \epsilon_{ijk}\omega_k \tag{3.37}$$

$\overline{\Omega_{ij}}$ is the mean rate-of-rotation tensor viewed in a rotating reference frame with the angular velocity ω_k. The constants in this model can be taken as

$$A_0 = 4.04,\ A_S = \sqrt{6}cos\phi$$

where

$$\phi = \frac{1}{3}cos^{-1}(\sqrt{6}W),\ W = \frac{S_{ij}S_{jk}S_{ki}}{S^3},\ S = \sqrt{S_{ij}S_{ij}}$$

The values of remaining constants are given by

$$C_2 = 1.9,\ \sigma_k = 1.0,\ \sigma_\varepsilon = 1.2.$$

3.5 Acoustic Model

Aerodynamically generated sound is calculated in FLUENT using Ffowcs Williams and Hawking's (FWH) method based on Lighthill's analogy. FWH equation is an inhomogeneous wave equation which is determined by manipulating the Navier-Stokes equations and continuity equation. FWH equation [44, 45] can be described as below:

$$\frac{1}{a_0^2}\frac{\partial^2 p'}{\partial t^2} - \nabla^2 p' = \frac{\partial^2}{\partial x_i \partial x_j}\left[T_{ij}H(f)\right] - \frac{\partial}{\partial x_i}\left[\left(P_{ij}n_j + \rho u_i(u_n - v_n)\right)\delta(f)\right] + \frac{\partial}{\partial t}\left[\left(\rho_0 v_n + \rho(u_n - v_n)\right)\delta(f)\right] \tag{3.38}$$

where,

u_i = component of velocity in the x_i direction

u_n = component of velocity perpendicular to the surface $f = 0$

v_i = component of surface velocity in the x_i direction

v_n = component of surface velocity perpendicular to the surface $f = 0$

$\delta(f)$ = Dirac delta function

$H(f)$ = Heaviside function

This equation is derived in Appendix A. Sound pressure at the farfield is denoted as p'. In an unbounded space, the exterior flow problem ($f > 0$) is embedded by proposing a mathematical surface described by $f = 0$. It aids the free-space Green's function and generalized function theory to achieve the result. The noise source (emission) is represented by the surface ($f = 0$) (i.e. wedge is the source in edge-tone computations), and it can be made simultaneous with a permeable surface off the body surface or body (impermeable) surface. n_i is the unit vector perpendicular to the exterior region ($f >0$), a_0 is sound speed at far field, and T_{ij} is the Lighthill stress tensor, described as in Eq. (2.3). The method for calculating sound utilizing the FWH acoustics model in FLUENT contains mainly two steps. In the initial step, time-accurate flow solution is produced from which time histories of the corresponding variables (e.g., density, velocity and pressure) on the picked source surface (*i.e.* wedge) is acquired. In the next step, the source data obtained from the previous step is used to calculate the sound pressure signals at the user-specified receiver locations. Then results are obtained by performing Fast Fourier Transformation (FFT) of the collected source data.

3.6 Boundary Conditions

A computational domain has to be selected, limited by a boundary and the boundary conditions for the potential flow computations have to be defined. Boundary conditions play a vital role in defining the domain. Directing the flow motion and specifying the

fluxes into the numerical domain (e.g. energy, momentum and mass) are done by the boundary conditions. Cell zones refer to the solid and fluid regions in the computational domain. Source terms and fluid material are designated to cell zones. Face zones mean the internal surfaces and boundary regions. Different types of boundary conditions are attached to the face zones as listed in Table 3-1. They represent the flow variables of boundary regions in the computational model.

Table 3-1: Domain Boundary Specifications

Label	Boundary type
OO’	Mass flow inlet/Velocity inlet
CEC’	Wall (Wedge)
AO and A’O’	Wall (Nozzle pipe)
OL and O’L’	Wall (Nozzle lip thickness)
LB, L’B’, BC and B’C’	Pressure Outlet (Ambient)

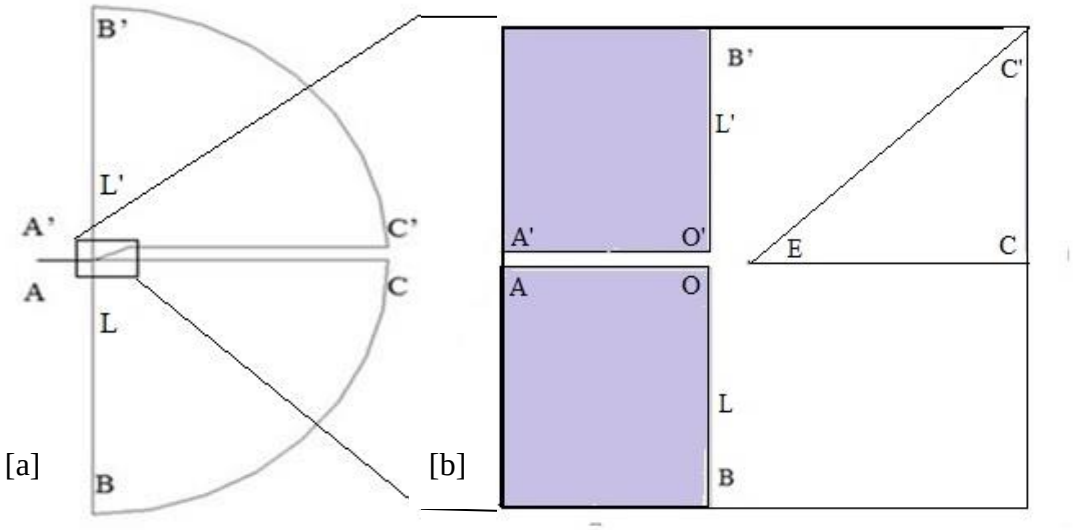

Figure 3-2: Computational domain: [a] Whole domain and [b] Close-up view of wedge impingement region

The boundary conditions involved in the present domain are shown in Fig. 3-2 in which a wedge is placed ahead of the jet slit. The domain boundary specifications are listed in Table 3-1 shown above. The wedge (wall) is represented by CEC’. Similarly, the jet slit is represented by edges OO´, nozzle lip thickness is represented by OL and O’L’, all

other edges are considered as pressure outlet represented by LB, L'B', BC and B'C'.

3.6.1 Mass Flow Inlet

The mass flow inlet boundary condition is utilized to model the flow inlet boundary for compressible flow. When it is applied for an inlet boundary condition, a velocity is calculated for every face in that region and the computed velocity is utilized to calculate the fluxes of all related solution variables into the numerical model as mentioned in Eq. (3.12). Accurate mass flow is retained by adapting the calculated total pressure in response to the interior solution for all iterations. Inputs of static pressure, flow direction, mass flow rate, and total temperature are utilized to calculate this velocity. Air acting as ideal gas is considered to flow out from a jet with high subsonic speeds (M > 0.3).

When a total mass flow rate is defined in FLUENT, it turns into a uniform mass flux (mass flow rate per unit area) internally, from Eq. (3.39) which shows the ratio of mass flow rate to the total inlet area:

$$\rho V_n = \frac{\dot{m}}{A} \tag{3.39}$$

To compute the fluxes of all variables as mentioned in Eq. (3.12) at the inlet, the normal velocity, V_n, is utilized along with the inlet value of the unknown variable ρ in Eq. (3.39). Then, the computed fluxes are utilized as boundary conditions for the respective conservation equations as mentioned in Eq. (3.12) during the course of solution. Mass flow rate boundary condition can be used for incompressible flow but it is not necessary. Because, velocity inlet boundary condition will solve the mass flow if the fluid density is a constant.

3.6.2 Pressure Outlet

Pressure outlet boundary condition is utilized to describe the static pressure at fluid outlets. An added advantage of this type of outlet boundary condition is that it defines scalar variables in case of back flow. At pressure outlet boundary condition, FLUENT considers the pressure at the input boundary condition as the static pressure of the flow at outlet. Then it is used to extrapolate all other conditions from domain interior. For subsonic compressible flows, the face pressure values at the outlet boundary is calculated using Eq. (3.40)

$$P_f = 0.5(P_c + P_e) + dp \tag{3.40}$$

Where,

P_c = interior cell pressure,

P_e = static pressure defined,

dp = pressure difference between the specified pressure P_e and the latest average pressure for the boundary defined in Eq. (3.41)

$$dp = \left[P_e - \frac{\sum_{i=1}^{i=n\_face} 0.5(P_c + P_e)(A)}{\sum_{i=1}^{i=n\_face} (A)} \right] \tag{3.41}$$

where,

A = Area of the pressure outlet boundary.

For incompressible flows, the face pressure is computed as an average between the specified pressure and interior pressure of adjacent cell.

$$P_f = 0.5(P_c + P_e) \tag{3.42}$$

With this boundary implementation, the exit pressure is not constant along the pressure outlet boundary. However, upon flow convergence the average boundary pressure becomes nearly equal to the specified static exit pressure. Because during flow convergence the interior cell pressures near the exit boundary would be different. So FLUENT takes average of all the interior cell pressures near the exit boundary to make it close to the specified exit pressure.

3.6.3 Wall

Wall boundary condition is utilized to constrain the solid and fluid regions. No slip boundary is applied at walls for viscous flow model. No slip boundary condition which requires that the fluid in contact with a wall.

$$u \times \hat{n} = U \times \hat{n} \tag{3.43}$$

Where, *u* is the velocity of fluid *in m/s*

U is the velocity of wall (In present study the wall is at rest)

$\hat{n}$ is the unit normal.

In no slip boundary condition, tangential velocity of fluid is equivalent to the velocity of wall while perpendicular component of velocity is set to be zero. Because of that normal component of the flux vector reduces to the following expression in 2-D flow in which only the pressure contribution remains at the wall.

$$\vec{F}.\hat{n} = \begin{vmatrix} 0 \\ p\hat{n}_x \\ p\hat{n}_y \\ 0 \end{vmatrix} \tag{3.44}$$

Details of flow in the flow-field near the wall are used to calculate the heat transfer and shear stress between the wall and fluid. Wedge and nozzle lip of the model is considered

as wall.

3.6.4 Numerical Scheme

Governing integral equations for the conservation of mass, momentum and energy (in case of compressible flow) are resolved in FLUENT using *segregated* or *coupled* solver based on Finite Volume Method (FVM). 2-D, unsteady, segregated, second order upwind solver is used as it solves the governing equations sequentially performing solution loop before convergence is reached for each time step. Second order upwind scheme is selected for spatial discretization while second order implicit scheme is picked for transient formulation. In second order upwind scheme the spatial accuracy is improved than the first order upwind scheme by introducing 3 data points instead of 2 which provide more accuracy of spatial derivative. For this scheme, 3 point backward difference (u_x^-) is defined as

$$u_x^- = \frac{3u_i^n - 4u_{i-1}^n + u_{i-2}^n}{2\Delta x} \tag{3.45}$$

While 3 point forward difference (u_x^+) is defined as

$$u_x^+ = \frac{-u_{i+2}^n + 4u_{i+1}^n - 3u_i^n}{2\Delta x} \tag{3.46}$$

Least squares cell-based gradient evaluation method is used in the second order upwind scheme.

Time step size is required to resolve the high frequency end of the sound spectrum and it can be calculated as

$$\Delta t = 1/f_{max} \tag{3.47}$$

For high speed edge-tones time step size is considered as 0.00001 *sec* to resolve the high

frequencies up to 50000 Hz. It is because Shannon's sampling theorem states to resolve frequencies up to 50000 Hz; the sampling rate should be at least 100000 Hz or anything higher. Total number of 8200 time steps (in which 1 time step consists of 25 inner iterations) is calculated in each case that corresponds to a total simulation time of 30 hours. First, the fluid properties are obtained and momentum equation is solved. Then the pressure corrections are made by continuity equation considering the current pressure and mass flow rate values. All the other equations including energy, FWH and scalar equations are then solved and checked for the convergence criteria.

All the cases are modeled in GAMBIT using personal computer equipped with Intel® Core™ i3, 2.53 GHz CPU and 4.00 GB of RAM with 64 bit operating system. The convergence criteria set for all the cases is 10^{-6}. Fluent Simulations is performed in High Performance Computing (HPC) provided by King Fahd University of Petroleum and Minerals, Saudi Arabia, equipped with Intel® Xenon® 2 GHz CPU and 40 GB of RAM with 64 bit operating system. Each case took on average about 30 hours to obtain the 8200 time steps (in which 1 time step consists of 25 iterations) in HPC with 21 cores. Each case ran on an average of about 205000 iterations.

CHAPTER 4

COMPUTATIONAL MODEL

4.1 Grid Generation

Grid generation is often considered as the most important part of CFD simulation. It is a process of dividing the region into a set of small control volumes. The quality of grid plays a direct role on the quality of the solution. The solution is more consistent and efficient when using a well-constructed grid. As the governing equations are solved for each grid point numerically during simulation, it is important to construct the proper grids in order to get the most accurate results in the proper amount of time. High speed test cases considered in this study are validated against the experimental model and data of Krothapalli et.al [13] which is described in section 4.2. High speed test cases are performed with very small time step size of 0.00001 *sec* for 8200 time steps, corresponding to the total time of 0.082 *sec* (in which 1 time step consists of 25 inner iterations). So high speed test cases geometry constructed with fine grid required around 75 hours to complete numerical calculations in HPC with 21 cores for the laminar flow model.

In order to reduce the required computation time to a reasonable amount to get acceptable results, a detailed grid study has been carried out for high speed test cases. In the present study, both structured and unstructured grids (*i.e.* hybrid grids) are used in meshing. Initially, the grid size is changed outside the jet impingement region (*i.e.,* the region

attached with wedge from the nozzle exit as shown in Fig. 4-3 (b)) where coarse grid has been used. Coarse region is constructed using unstructured grid with tri-pave elements. Because pave mesh is used for non-uniform or complex structures. When the same number of mesh nodes on both edges cannot properly matched, pave mesh is used. Since the pressure outlet boundary is semi-circular, mesh nodes are not properly matching on the wall boundary (*i.e.* wedge). So tri-pave mesh is the most suitable. Jet impingement region is constructed of fine structured grid with quad map elements having interval size of 0.02 *mm*. Six different growth rates of 1.05, 1.1, 1.15, 1.2, 1.3 and 1.5 are used on the coarse grid region to reduce the grid size. The growth rate indicates the increase in mesh-element edge length with each succeeding layer of elements. For example, a growth rate of 1.2 results in a 20% increase in mesh-element edge length with each succeeding layer of elements. The growth rate of 1.2 is selected because the computational time is reduced considerably due to the reduction in grid size and the computed results using laminar flow model has 7.4% error compared with the experimental data. The effect of the growth rate changes on grid is presented in Table 4-1 and Fig. 4-1 for the test case having stand-off distance of $d/h = 0.1666$.

Table 4-1: Grid Study - Growth Rate Effect for High Speed Case

Growth Rate	**Grid Size**	**The Computed Edge-tone Frequency (Hz)**	**Experimentally observed edge-tone frequency (Hz) [13]**	**% Error** $\left[\frac{Exp.Freq - Comp.Freq}{Exp.Freq}\right]\times 100$
1.05	312476	3421	3600	5.0
1.1	249504	3395	3600	5.7
1.15	233710	3361	3600	6.6
1.2	227012	3334	3600	7.4
1.3	203616	3297	3600	8.4
1.5	201024	3190	3600	11.1

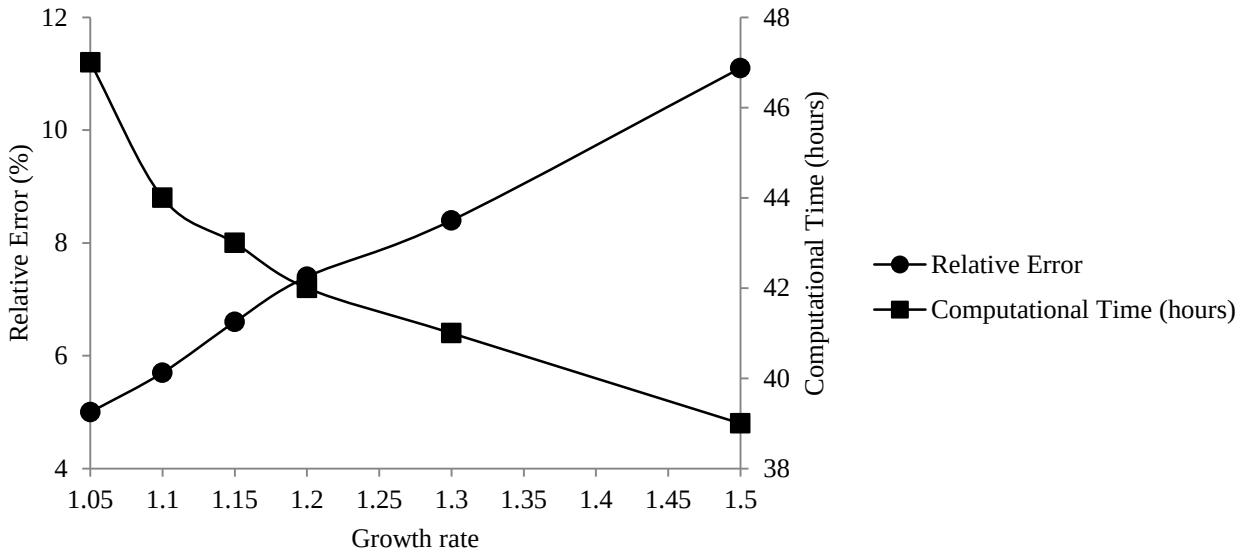

Figure 4-1: Grid study – effect of growth rate on the computed fundamental edge-tone frequency

After the growth rate is selected, the interval size of the fine grid near the jet impingement region is changed to observe the effect of grid size on computed edge-tone frequency. Five different cases of interval sizes are used on the fine grid region to reduce the grid size. The acceptable interval size is found out to be 0.05 *mm* because of the reduction in computation time along with the acceptable error of 7.41 % compared with the experimental data. The effect of the interval size changes on grid is presented in Table 4-2 and Fig. 4-2.

Table 4-2: Grid Study - Interval Size Effect for High Speed Case

Interval Size	**Grid Size**	**The Computed Edge-tone Frequency (Hz)**	**Experimentally observed edge-tone frequency (Hz) [13]**	**% Error** $\left[\frac{Exp.Freq - Comp.Freq}{Exp.Freq}\right]\times 100$
0.01	864842	3335	3600	7.36
0.02	227012	3334	3600	7.38
0.03	158734	3334	3600	7.38
0.04	107474	3334	3600	7.38
0.05	80898	3333	3600	7.41

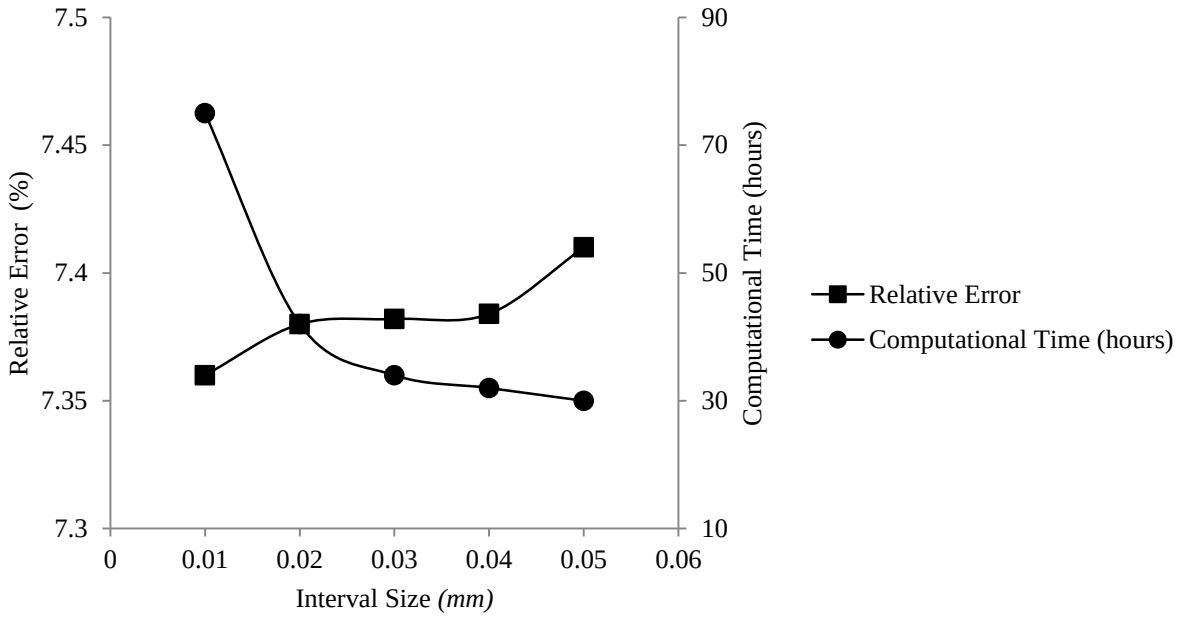

Figure 4-2: Grid study – effect of interval size on the computed edge-tone frequency

The grid for the case of, stand-off distance, d/h = 0.1666, nozzle lip thickness, d/t_{nl} = 0.0652 and wedge angle 20°, is shown in Fig. 4-3. It consists of 80898 cells with interval size of 0.05 *mm* near the jet impingement region and growth rate of 1.2 outside the jet impingement region.

Table 4-3: Size Function Parameter Values

Parameter	Value
Start Size	0.05 *mm*
Growth Rate	1.2
Maximum Size	60 *mm*

Slit and jet impingement regions are constructed with fine quad map elements with interval size of 0.05 *mm* and outside regions are constructed of coarse grid consists of tri-pave elements. A size function has been attached near the jet impingement region to control the size of mesh elements for faces with the parameters listed in Table 4-3. Mass flow inlet, wall and pressure outlet boundary conditions assigned for inlet, nozzle lip thickness and wedge, and outlet, respectively. Outer domain boundaries are constructed

far away from the area of interest. It is normally constructed at 30 to 35 times the length of area of interest [46]. In our case, stand-off distance and wedge extension are the area of interests. So from the experimental set up of Krothapalli *et.al* [13], the outer domain boundaries are estimated and retained at 167*d*, where *d* is the slit width as shown in Fig. 4-3.

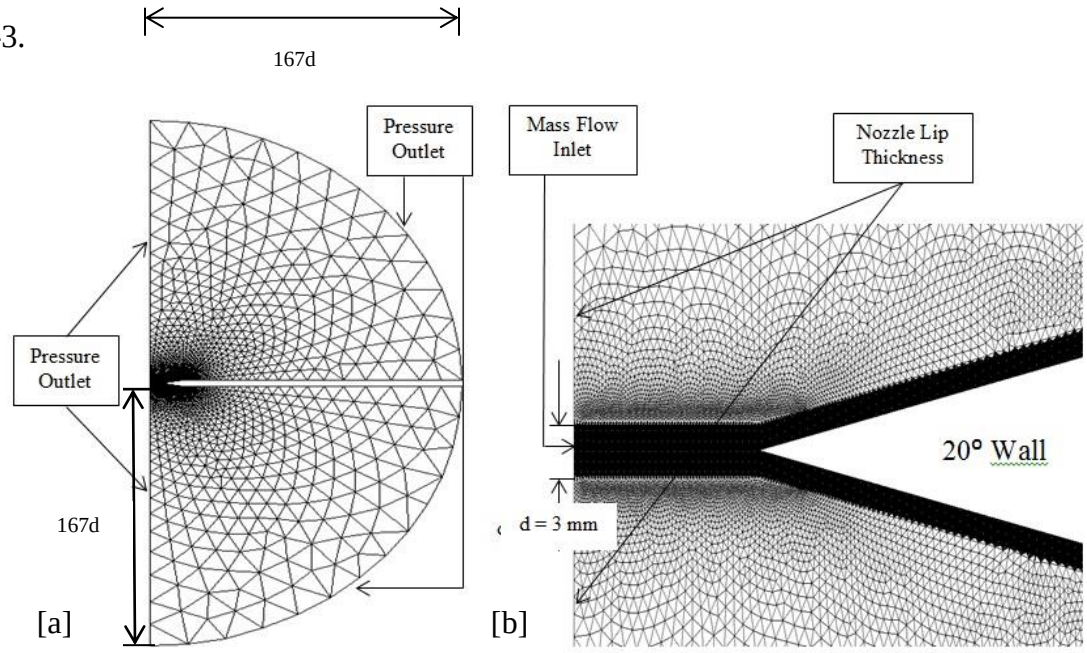

Figure 4-3: Computational domain: [a] Grids on entire domain (grid size of 80898 cells) and [b] Close-up of grid near the wedge where *d/h* = 0.1666

4.1.1 Structured Grid

Structured grid allows high degree of control as the user is free to place control points and edges at the desired locations to enhance the quality of the grid. Structured mesh flow solver typically require low memory to execute the solution faster as they are optimized for structured layout of the grid. Because cells in the structured grid is organized in rows and columns (for 2-D) and each node is encircled with equivalent number of neighboring elements. So FLUENT program working on entire mesh can directly address the neighboring cells to evaluate the difference in physical variables of any cell. While in unstructured mesh, grid points have unknown number of neighbors, domain can have any

shape and storing of data requires complex special structures. In the present study, for the validation and parametric study, mesh is constructed using a well-structured grid within the stand-off region and on the wedge as shown in the Fig. 4-4. The grid is uniform to properly resolve the various flow gradients near the walls and in the shear layer.

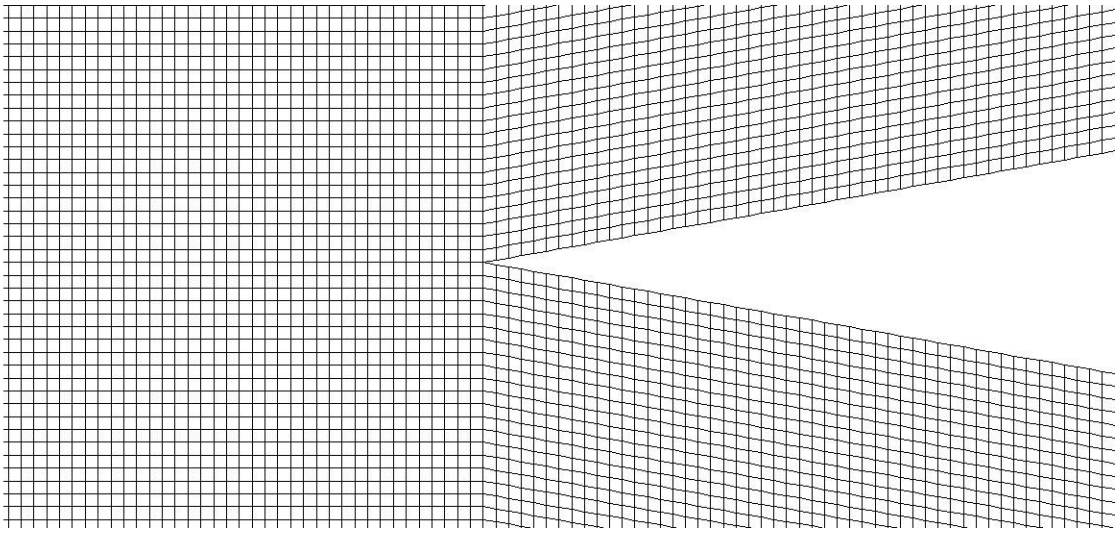

Figure 4-4: Domain discretized using a structured grid near the wedge using quad map elements with interval size of 0.02 mm

In the present case, the velocity gradient near the walls has to be resolved; therefore, the grid is fine and uniform near the walls. Since edge-tone is generated when jet impinges on a wedge, fine and uniform grid of quad map elements are constructed along the stand-off distance and wedge extension region. Fine grid is constructed on both of the wedge extension surfaces and extended normally up to a length which is equal to half of the slit width. Hence, fine grid is constructed where it is needed while coarse grid is applied in all other parts of the geometry in order to save computational time.

4.1.2 Hybrid Grid

A structured grid is the more economical way of meshing and computationally solving a problem. However, there are many cases in which the geometry becomes complex and

intricate where a structured grid becomes very difficult to construct. In such cases, the user is forced to use unstructured mesh to resolve all the regions of the domain. Unstructured grid uses an arbitrary collection of elements to fill the domain. Because the grid shown in Fig. 4.4, the wedge-jet arrangement is not a repeated pattern as in structured grid, the mesh is called unstructured. An advantage of such a grid is that it requires a very little input from the user and is numerically generated using different unstructured grid generation schemes. Thus, the user has very little control over the elements and their arrangement. Hence, this type of grid generation is used when users encounter complex geometry which cannot be meshed using a structural pattern.

A geometry may require unstructured grid generation but not in the entire domain. In such cases, a combination of structured and unstructured mesh is used where only few faces are subjected to the required type of grid. Such a combination of grids is called a hybrid grid. In the present study, structured grid is constructed from nozzle exit to wedge and unstructured grid is constructed at other regions as shown in Fig. 4-3 (b). For the case of stand-off distance, d/h = 0.1666 and Mach number of 0.87, the mesh nodes inside the shear layer in laminar flow model at d/h = 0.0833 are presented as horizontal lines in Fig. 4-5. Along the nozzle exit, the mesh nodes are placed at an interval size of 0.05 *mm* that makes the total number of 30 nodes. Growth rate of 1.2 is attached at the end of nozzle exit. So along the shear layer 13 nodes are placed near the nozzle lip region. This indicates that the shear layer region is constructed with fine mesh. Hence, high speed test geometries are constructed according to the present grid study.

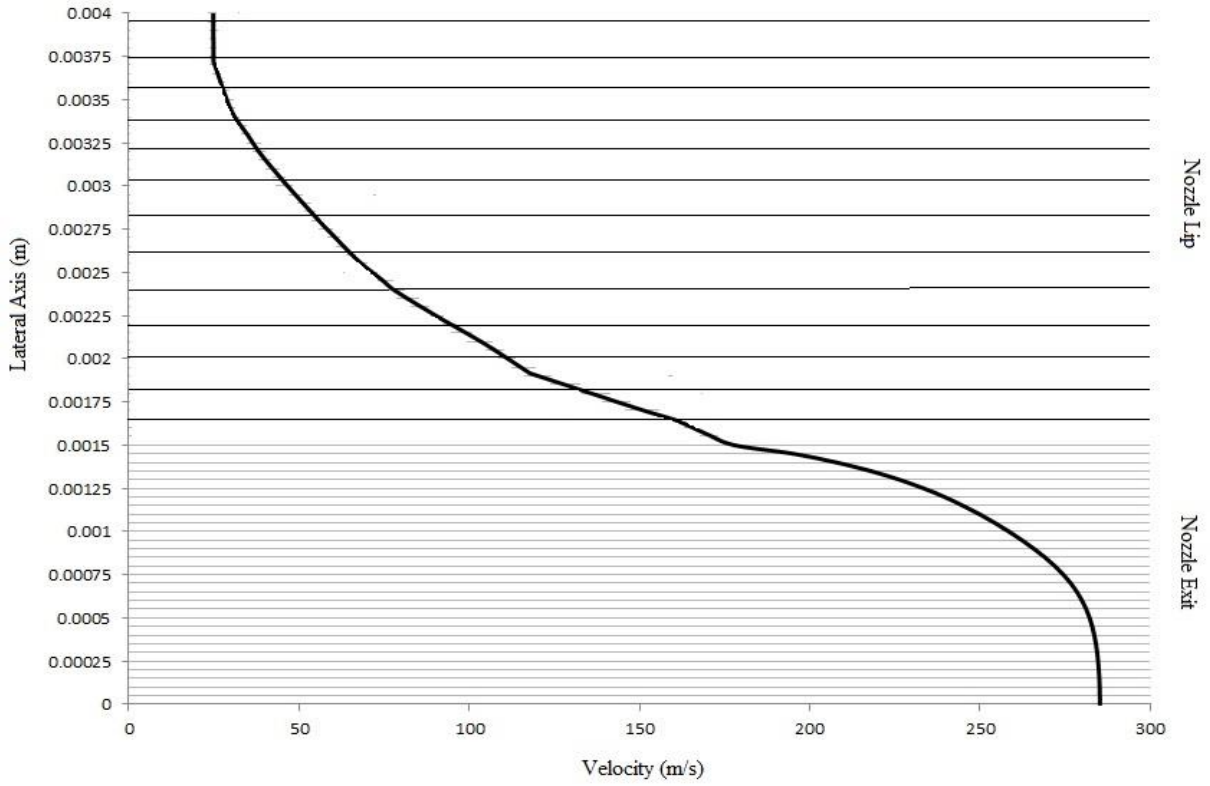

Figure 4-5: Mesh nodes along the shear layer in laminar flow model at *d/h* = 0.0833, for the case of *d/h* = 0.1666 and *M* = 0.87

4.2 Validation Case

Krothapalli *et al.* [13] performed experiments using the experimental set-up shown in Fig. 4-6, to generate high speed edge-tone frequencies. They formed the jet by blowing air through a two-dimensional channel of width 0.158 cm to the wedge of angle 20°.

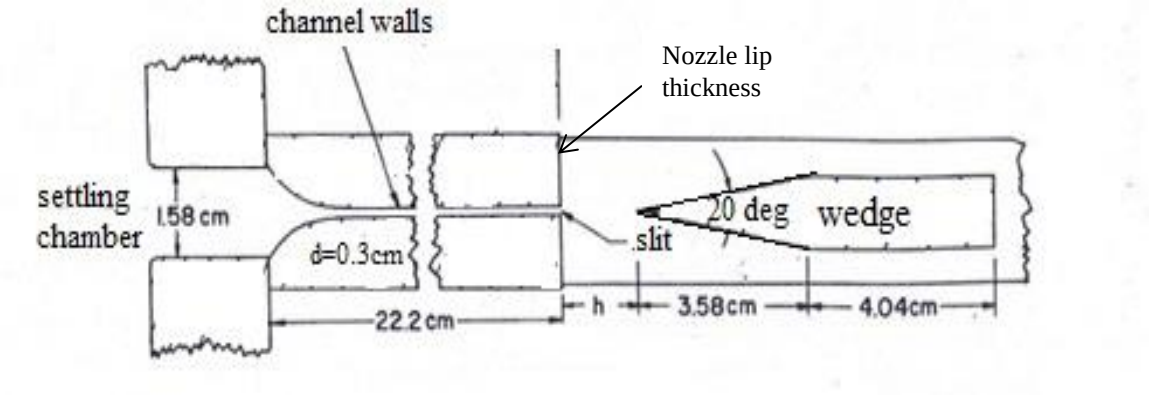

Figure 4-6: The experimental set-up of high speed jet impingement on a wedge [11]

The entrance section of the channel is rounded and begins in a settling chamber that contains damping screens. The speed of the nozzle flow for top hat velocity profile is calculated from the static pressure drop computed between two points along the channel and the jet is discharged through a sharp-edged slit, the mean speed is determined from the pressure drop across the slit (orifice) [11]. The velocity profile distributions are obtained from hot wire measurements. From the Fig. 4-6, the domain boundaries are estimated and the dimensions of wedge angle, slit width, stand-off distance and nozzle lip thickness are constructed as shown in Fig. 4-3 after grid study. Edge-tone frequency is obtained as 3333 Hz from FWH acoustic results in FLUENT for d/h = 0.1666 and M = 0.87 for observer located at *10d* distance from the nozzle exit. It is calculated by taking Fast Fourier Transform (FFT) of the FWH acoustic data in FLUENT. To verify the FWH acoustic module, static pressure data history at the wedge tip is obtained from flow-field. Edge-tone frequency is calculated from FFT of the static pressure data. Both methods provided same edge-tone frequencies. Validated for minimum breadth cases also which is described in chapter 5.3. After the successful validation, the model is used for simulation of different cases.

4.3 Grids for Parametric Study Cases

4.3.1 Grids for Wedge Angle Study

The effect of wedge angle on edge-tone is studied by considering three different wedge angles of 20°, 60° and 180°. Grids are constructed with the same criteria that consist of fine grid on the jet impingement region and coarse grid outside the jet impingement region. The schematics of the grid for two wedge angles 60° and 180° are shown in Fig. 4-7 and Fig 4-8.

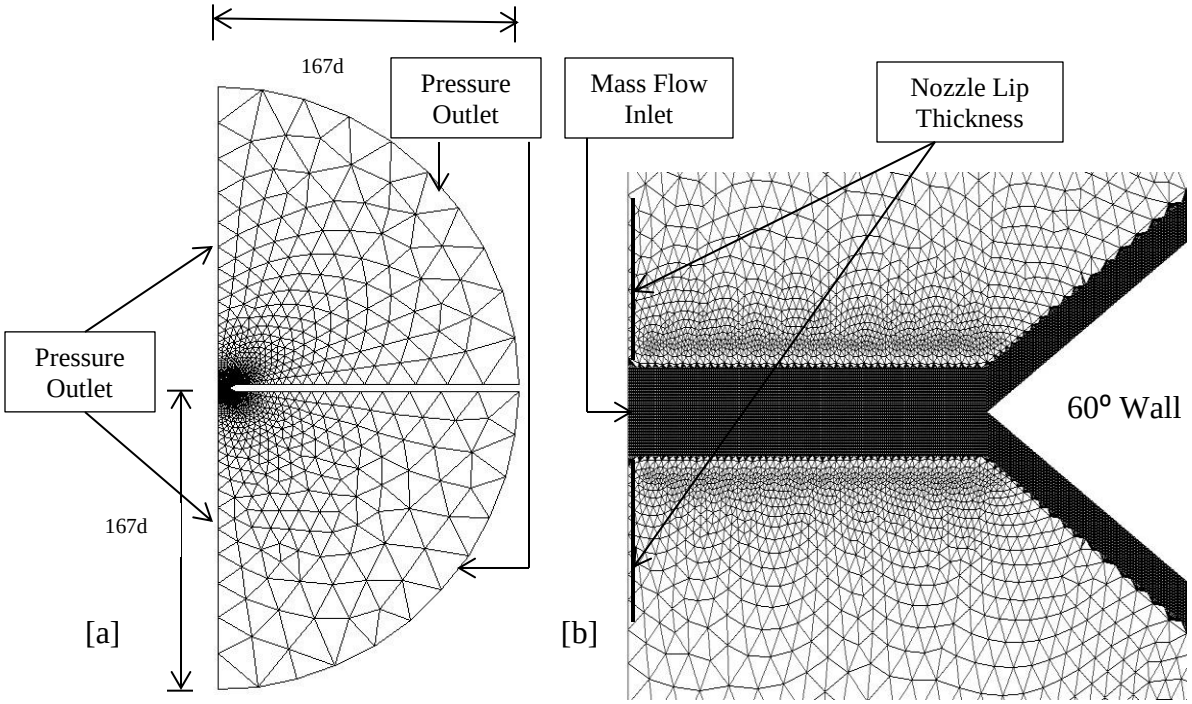

Figure 4-7: Computational domain: [a] Grids on entire domain (grid size of 85700 cells) and [b] Close-up of grid near the wedge where *d/h* = 0.1666 (wedge angle 60^{o})

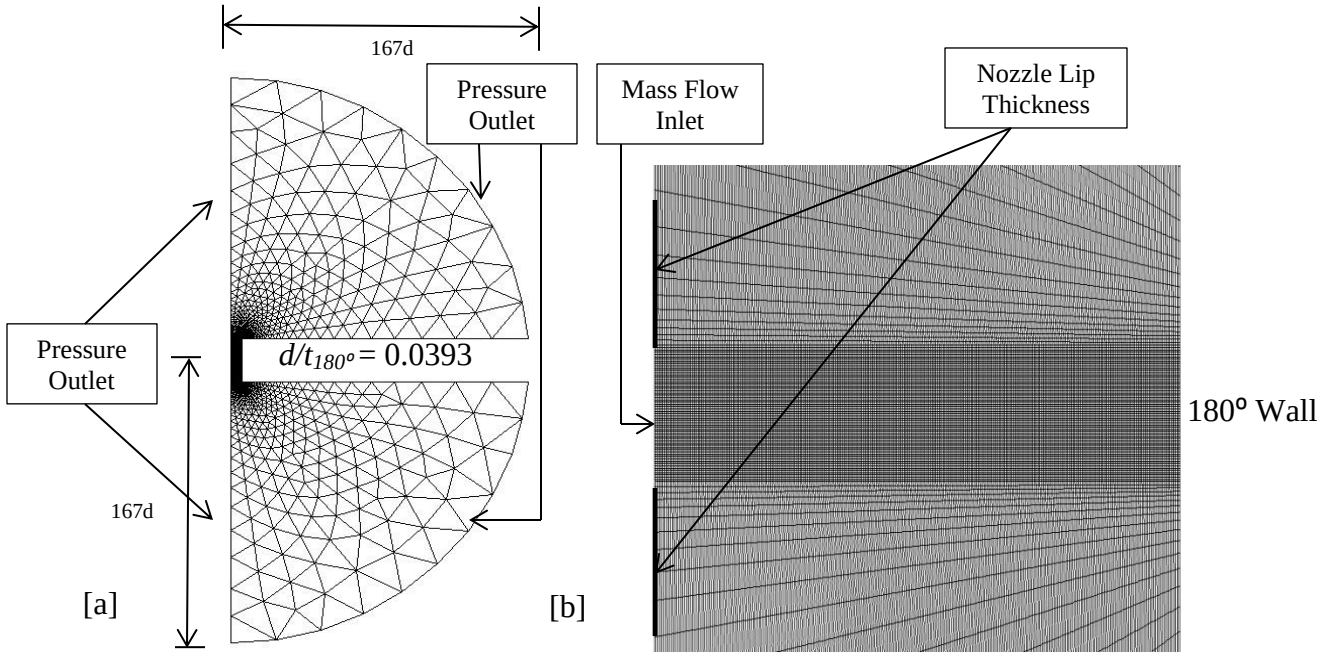

Figure 4-8: Computational domain: [a] Grids on entire domain (grid size of 94817 cells) and [b] Close-up of grid near the wedge where *d/h* = 0.1666, d/t_{180} = 0.0393 (wedge angle 180^{o})

The above grids are constructed for the case of *d/h* = 0.1666. Size function used for construction of the different wedge angle cases is the same as in Table 4-3. The grid sizes

for the three different angles are listed in Table 4-4. Similarly, the grid for different wedge angles are constructed for five different wedge locations *(d/h)*, specifically; 0.1818, 0.1428, 0.0952, 0.0869, and 0.0800. The wedge angle effect on edge-tone is discussed in Chapter 5.

Table 4-4: Grid size for different wedge angles

Wedge Angle	Grid Size
20°	80898
60°	85700
180°	94817

4.3.2 Grids for Nozzle Lip Thickness Study

The effect of nozzle lip thickness on edge-tone is examined for five different nozzle lip thicknesses at wedge location, d/h = 0.1666 and wedge angle 20°. Krothapalli *et al.* [13] performed experiments using the experimental set-up as shown in Fig. 4-6 which has nozzle lip thickness, d/t_{nl} = 0.0652. The grid for nozzle lip thickness, d/t_{nl} = 0.0621 is shown in Fig. 4-9. The grid sizes of different nozzle lip thicknesses are listed in Table 4-5. The effect of nozzle lip thickness on edge-tone is discussed in chapter 5.

Table 4-5: Grid size for different nozzle lip thicknesses

Slit width/Nozzle lip thickness (d/t_{nl})	Grid Size
0.0686	80886
0.0668	80910
0.0660	80906
0.0652	80898
0.0636	80860
0.0621	80894

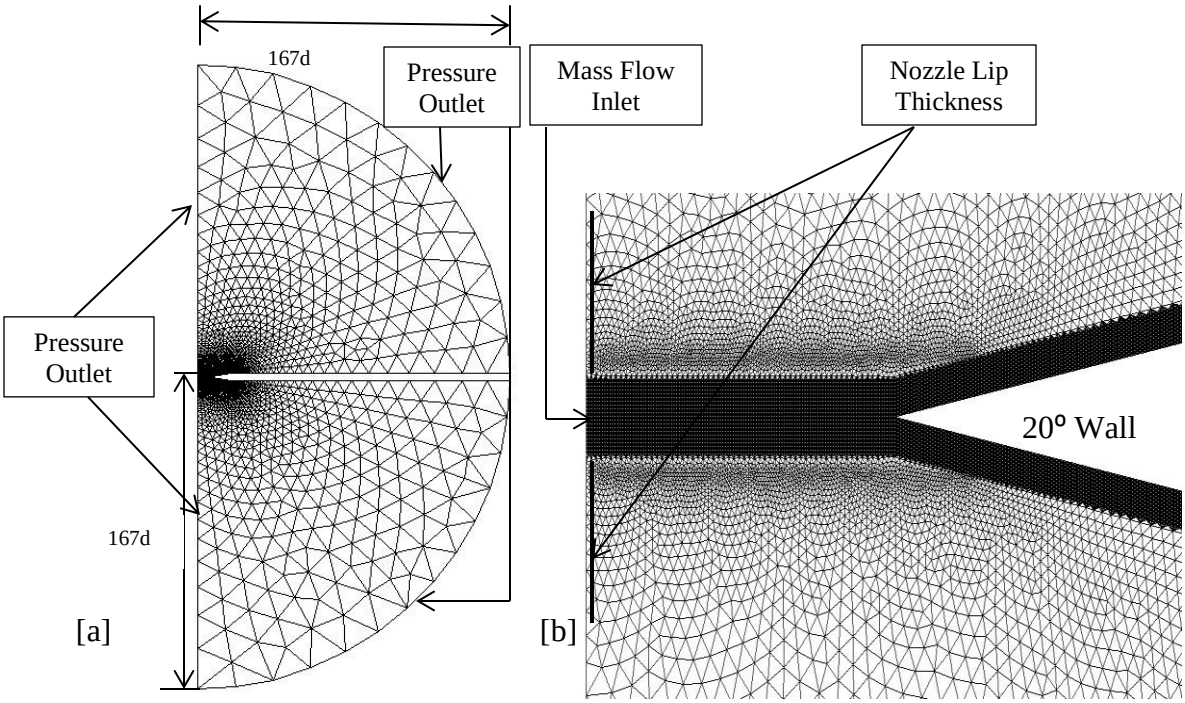

Figure 4-9: Computational domain: [a] Grids on entire domain (grid size of 80894 cells) and [b] Close-up of grid near the wedge where d/h = 0.1666 and d/t_{nl} = 0.0621

4.3.3 Grids for Edge-tone Suppression

The edge-tone suppression is achieved by injecting microjet laterally inside jet plume which alters the shear layer. Edge-tone suppression is examined for three different stand-off distances at different locations of microjet injection and wedge angle 20°. The grid for stand-off distance, d/h = 0.1666 and tube length, d/l_t = 0.0621 is shown in Fig. 4-10. The grid sizes of three different stand-off distances for d/l_t = 0.375 are listed in Table 4-6. Edge-tone suppression results are discussed in chapter 5.

Table 4-6: Grid size for different stand-off distances for edge-tone suppression test cases

Slit width/Stand-off distance (d/h)	Slit Width/Tube Length (d/l_t)	Grid Size
0.1666	0.375	167464
0.1428	0.375	172726
0.0869	0.375	212218

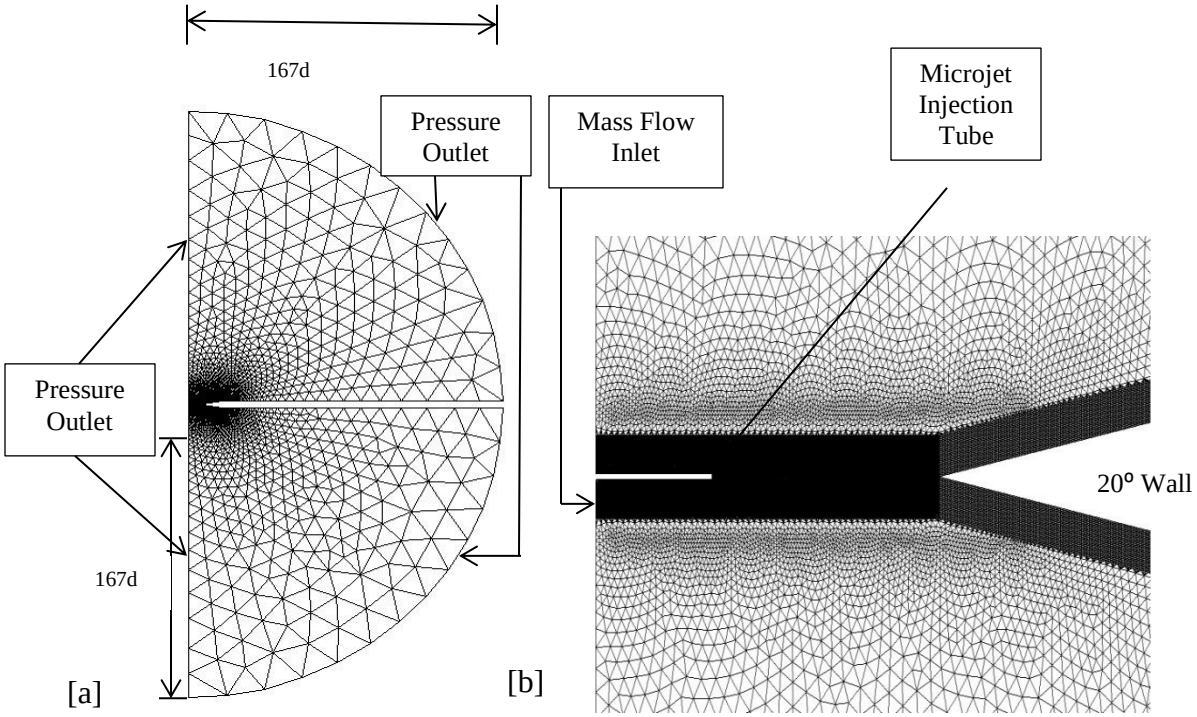

Figure 4-10: Computational domain:[a] Grids on entire domain (grid size of 167464 cells) and [b] Close-up of grid near the wedge where d/h=0.1666 and d/l_t=0.375

CHAPTER 5

RESULTS AND DISCUSSION

5.1 Validation of High Speed Edge-tone Test Case

For high speed edge-tones, the validations are conducted using both laminar and realizable k-ε turbulence flow models in FLUENT at Mach number of 0.87 at different stand-off distance *(d/h)* to capture the associated edge-tone generated flow-field. Six cases have been considered to simulate the two stages of edge-tone frequencies as shown in Table 5-1.

Table 5-1: Validated cases for high speed jet

d/h	Computed edge-tone frequency using laminar model (Hz)	Computed edge-tone frequency using realizable k-ε model (Hz)	Experimentally observed edge-tone frequency (Hz) [13]	% Error (Laminar model)	% Error (realizable k-ε model)
0.1818	3888	3950	4200	7.4	5.9
0.1666	3333	3570	3600	7.4	1.0
0.1428	3055	3080	3300	7.4	6.6
0.0952	4351	4510	4800	9.3	6.0
0.0869	4074	4240	4250	4.1	0.5
0.0800	3888	3870	3600	8.0	7.5

Fig. 5-1 shows the effect of stand-off distance on edge-tone frequencies using laminar and realizable k-ε turbulence flow models along with the experimental data. Two stages of edge-tone frequencies are captured and coexistence of edge-tones occurred when second stage appeared. It is clearly evident that both models predicate the edge-tone

frequency fairly well. The maximum error is almost the same in the computed edge-tone frequency which is about 8%. From laminar flow model data, phase lag p is calculated using Powell's feedback loop given by Eq. (2.4) by considering average jet disturbance velocity, U_c, in Eq. (2.5) as half of the main jet velocity, U_j. Then average phase lag value of -0.35 is resulted. This value is considered as constant to compute theoretical edge-tone frequency for all the cases using Powell's feedback loop given by Eq. (2.4). This value is in agreement with Kwon *et al.* [8] who proposed phase lag value varies between -0.5 to 0 *(i.e.* $-0.5<p<0$*).* Results from Powell's theoretical formula are also shown in Fig. 5-1 with $p = -0.35$.

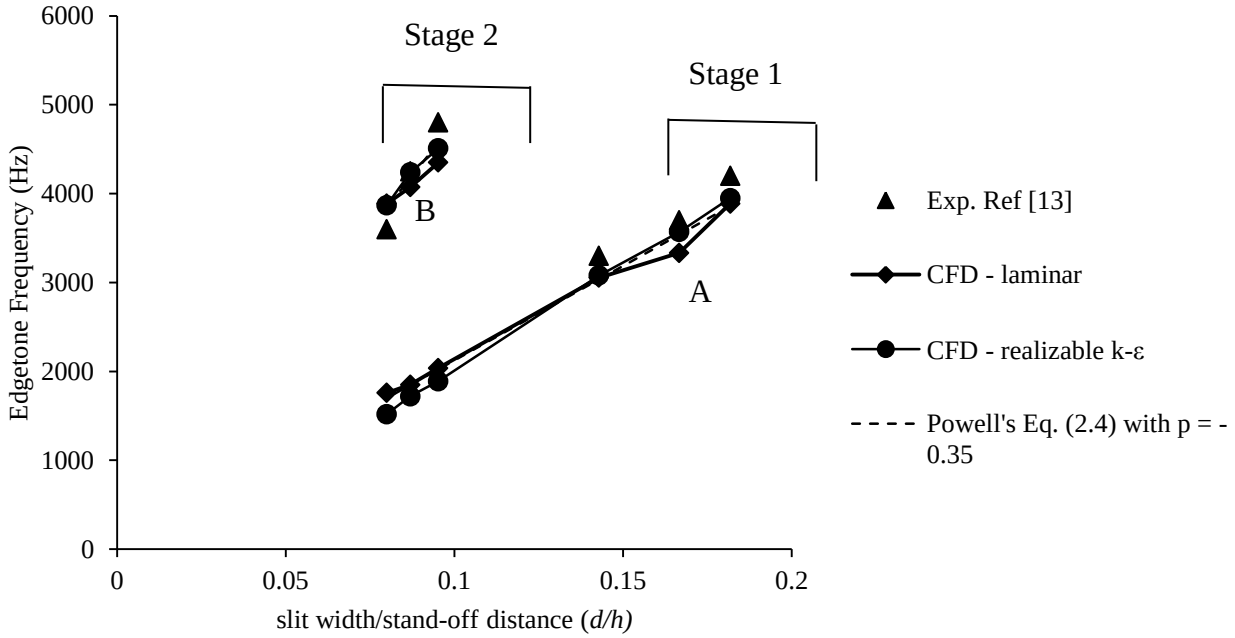

Figure 5-1: High speed jet edge-tone staging phenomenon computations at acoustic field point

The static pressure contours of flow-field associated with laminar and realizable k-ε turbulence flow models for the case of $d/h = 0.1666$ and Mach number of 0.87 are shown in Fig. 5-2 and Fig. 5-3. In those figures, t_o refers to any time during the stable oscillation of the flow.

p in *Pa*

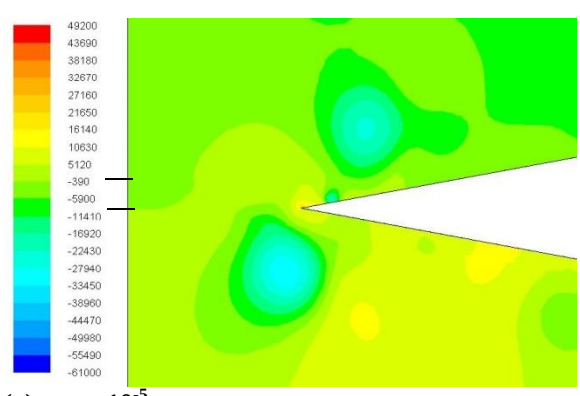

(a) at $t_0 \times 10^{-5}$s

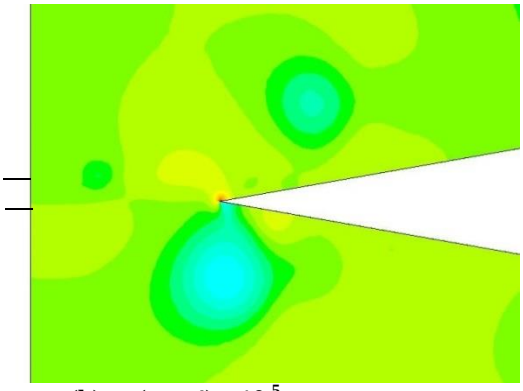

(b) at $(t_0 + 4) \times 10^{-5}$s

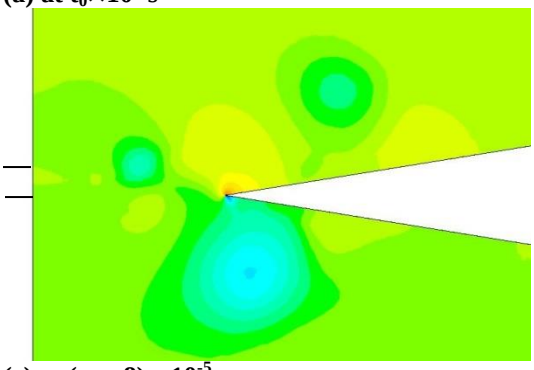

(c) at $(t_0 + 8) \times 10^{-5}$s

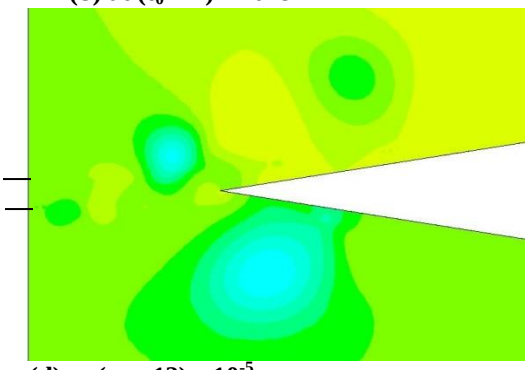

(d) at $(t_0 + 12) \times 10^{-5}$s

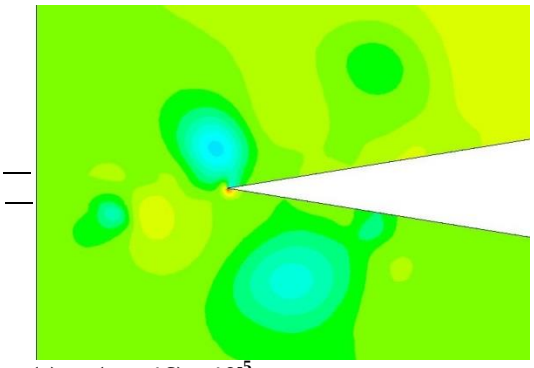

(e) at $(t_0 + 16) \times 10^{-5}$s

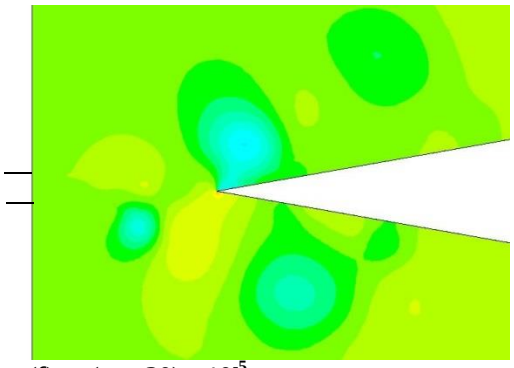

(f) at $(t_0 + 20) \times 10^{-5}$s

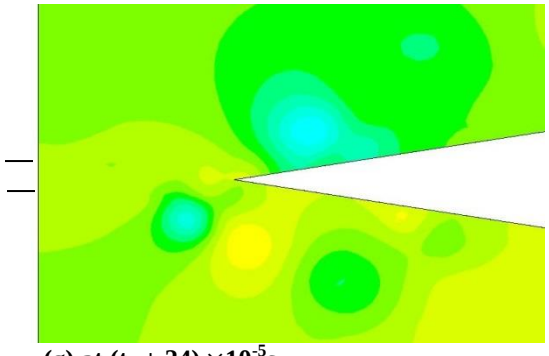

(g) at $(t_0 + 24) \times 10^{-5}$s

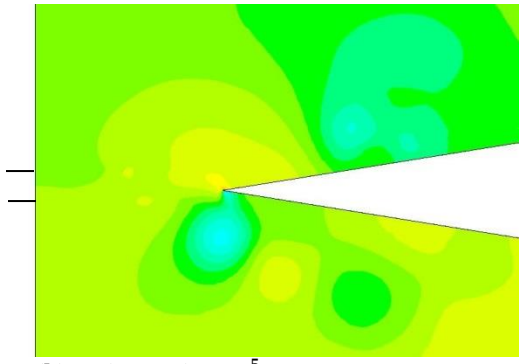

(h) at $(t_0 + 29) \times 10^{-5}$s

Figure 5-2: Static pressure contours for laminar flow model at *d/h*=0.1666 and *M*=0.87

p in *Pa*

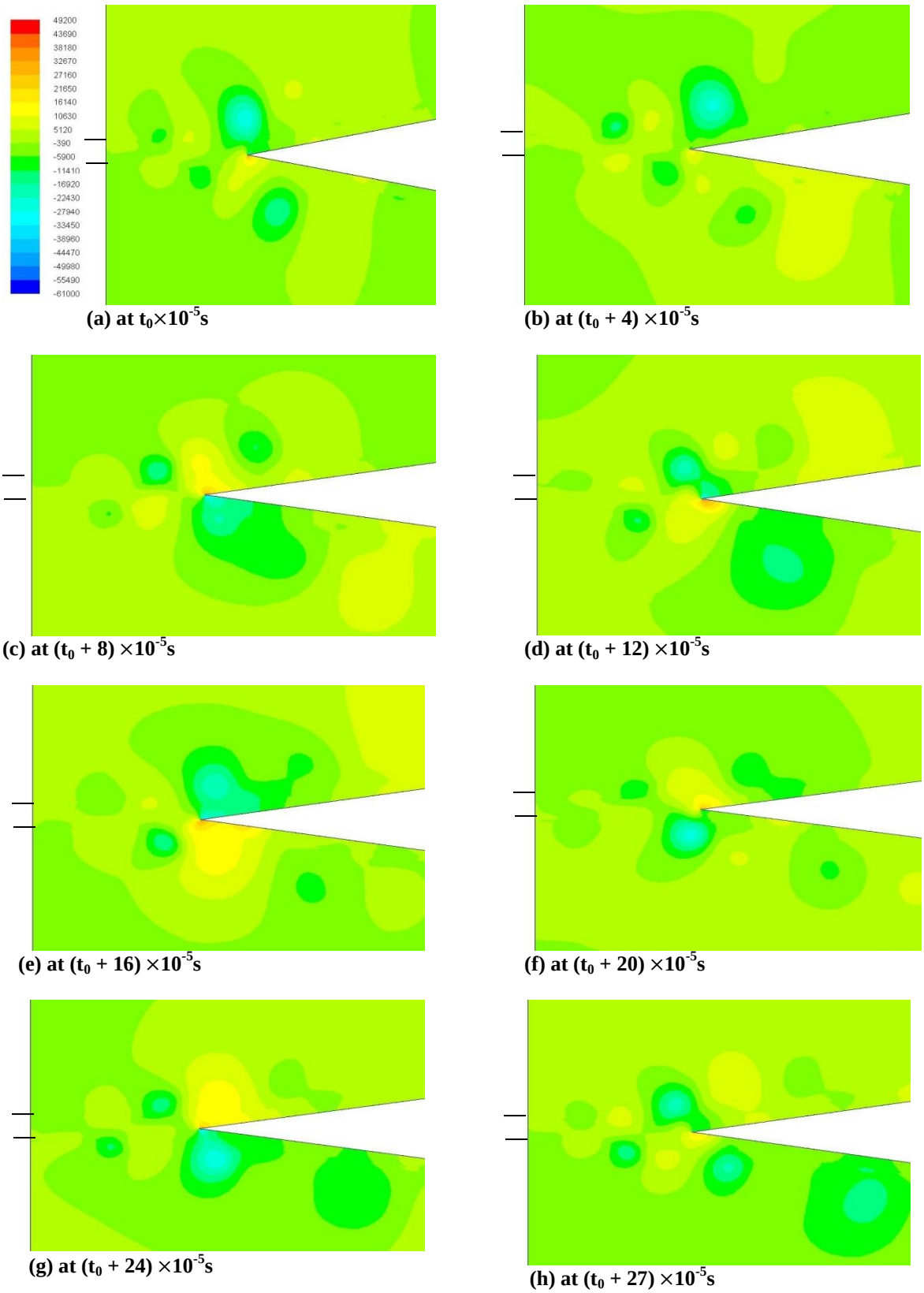

(a) at $t_0 \times 10^{-5}$s **(b) at $(t_0 + 4) \times 10^{-5}$s**

(c) at $(t_0 + 8) \times 10^{-5}$s **(d) at $(t_0 + 12) \times 10^{-5}$s**

(e) at $(t_0 + 16) \times 10^{-5}$s **(f) at $(t_0 + 20) \times 10^{-5}$s**

(g) at $(t_0 + 24) \times 10^{-5}$s **(h) at $(t_0 + 27) \times 10^{-5}$s**

Figure 5-3: Static pressure contours for turbulent flow with realizable k-ε turbulence flow model at *d/h* = 0.1666 and *M*=0.87

Pressure zones of blue color in these figures indicate the pressure drop due to vortices. Sizes of the pressure zone increases along the stand-off distances. This represents the amplification of vortices in the edge-tone system which is clearly evident from Fig. 5-2 and Fig. 5-3. In comparison, pressure zones in the realizable k-ε turbulence flow model are less in size than the laminar flow model. It indicates that the sound intensity is less in realizable k-ε turbulence flow model which is explained in Fig. 5-9 and Fig. 5-10.

Convective speed of jet disturbance is calculated for the laminar flow model and realizable k-ε turbulence flow model for the case of d/h = 0.1666 using the most reliable method of Karamcheti *et al.*[11]. In this method, jet disturbance convective speed, U_c, is not considered as half of the main jet velocity, U_j. Instead, it is computed using the phase variation along the centerline of the fluctuating lateral velocity components obtained from the simulation data. Phase computations are made with respect to the fluctuation of the lateral velocity components along the centerline of the jet at x/h, specifically; 0, 0.1666, 0.3333, 0.5, 0.6666, 0.8333 and 1. The phases at different locations are reported relative to the phase at the slit and presented in Fig. 5-4. The angle in degrees by which the phase at a given location lags behind that at the slit is denoted by θ. The values of vertical axis in Fig. 5-4 denote the local phase angle divided by 2π. Autocorrelation method is used to calculate the phase lag and the MATLAB code used for this computation is described in Appendix B. The relation between the convection velocity U_c and phase $\theta(x)$ is reported by Karamcheti *et al.* [11] and given by the following relation

$$U_c(x) = \frac{f}{\frac{d}{dx}\left(\frac{\theta(x)}{2\pi}\right)} \tag{5.1}$$

where f is the edge-tone frequency in *Hz*. The above relation can be deduced as follow.

$$U_c(x) = \frac{\omega}{K} = \frac{\frac{d\theta}{dt}}{\frac{d\theta}{dx}} = \frac{2\pi f}{\frac{d\theta}{dx}} = \frac{f}{\frac{d}{dx}\left(\frac{\theta(x)}{2\pi}\right)} \tag{5.2}$$

where ω is the angular frequency and K is the wave number. Using Eq. (5.1) the variation of convective speed of jet disturbance along the centerline of the jet is calculated and it is shown in Fig. 5-5.

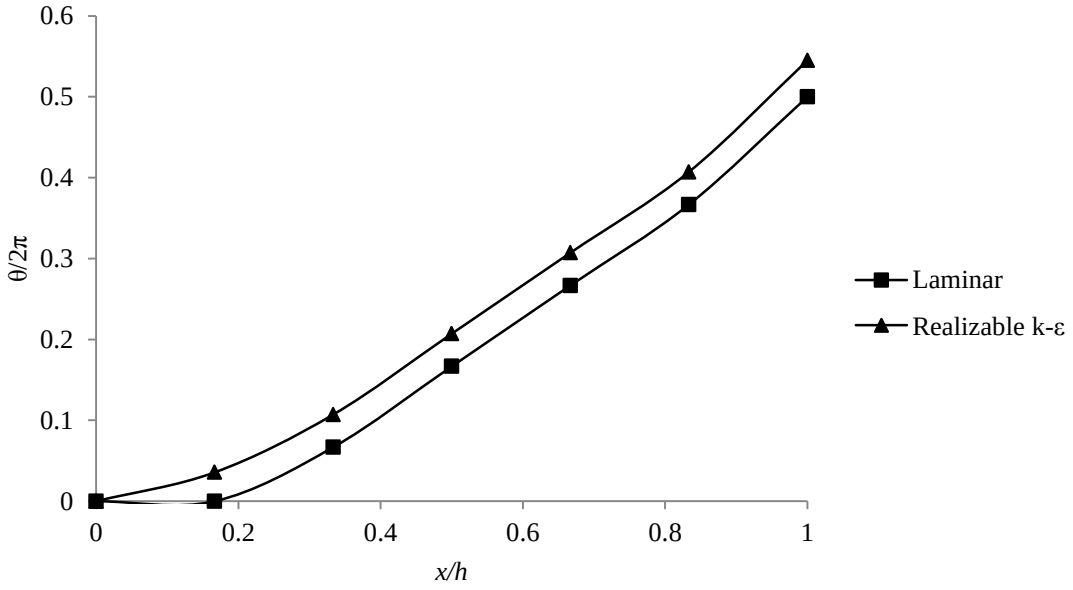

Figure 5-4: Phase variation for laminar and realizable k-ε turbulence flow models at *d/h* = 0.1666, *M* = 0.87 and $\dot{m}$ = 1.145

From Fig. 5-5, it is clear that the jet disturbance convective speed of laminar flow model is lesser than the realizable k-ε turbulence flow model. It means that downstream propagation time, T_1, increases in laminar flow model as indicated by Eq. (2.5). So T_1 is 0.000167*s* for turbulent flow model while it is 0.00017*s* for laminar flow model. This causes the edge-tone frequency to decrease in laminar flow model as indicated by Eq. (2.4). Hence, the edge-tone frequency computed using the laminar flow model is slightly lesser than that computed by the realizable k-ε turbulence model as shown in Fig. 5-1 and Table 5-1.

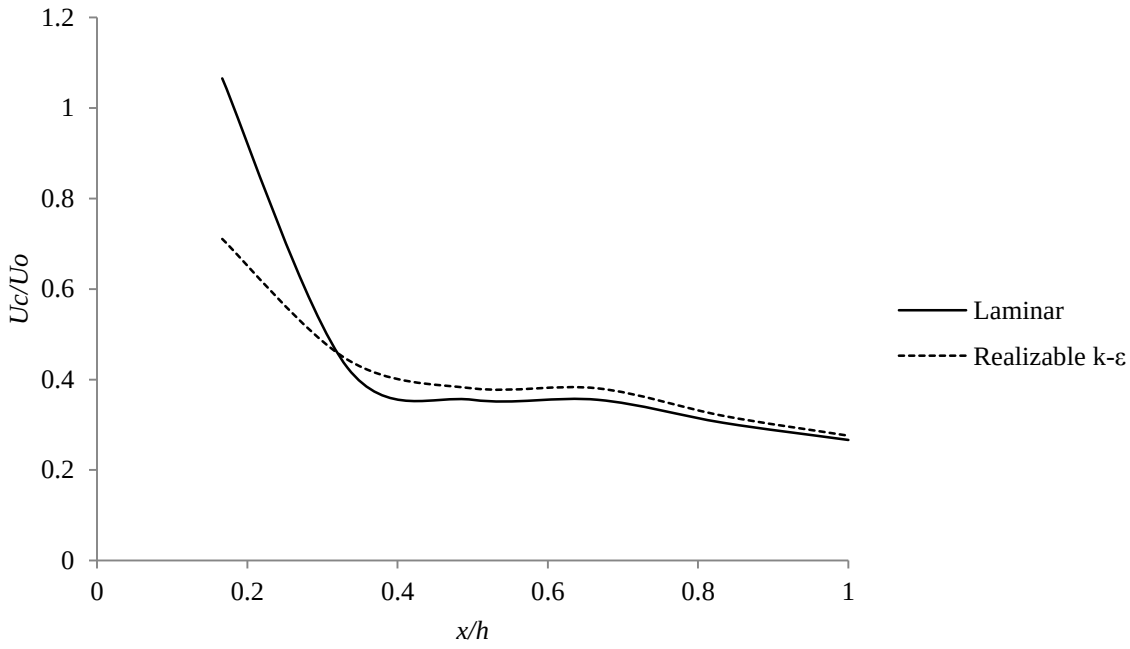

Figure 5-5: Variation of jet disturbance convective speed along the stand-off distance for laminar and realizable k-ε turbulence flow models (*d/h* = 0.1666, *M* = 0.87 and $\dot{m}$ = 1.145)

Sound Pressure Level (SPL) of cases A and B (shown in Fig. 5-1) are acquired by an acoustic receiver located at a certain distance in the acoustic field. It is placed at 10*d* distance and 45° angle from nozzle exit as shown in Fig. 5-6. This location of receiver is considered for all high speed simulations in this study to acquire acoustic data. SPL values of cases A and B for laminar flow model and realizable k-ε turbulence flow model are shown in Fig. 5-7 and Fig. 5-8. The frequency associated with the first peak amplitude represents the edge-tone frequency. Harmonics of edge-tone frequency are also clearly shown in these figures. Harmonics is a signal or wave whose frequency is a multiple number of the fundamental frequency of edge-tone. From Fig. 5-7 and Fig. 5-8, it is evident that the relative amplitude of Sound Pressure Level (SPL) of realizable k-ε turbulence flow model is less than the laminar flow model.

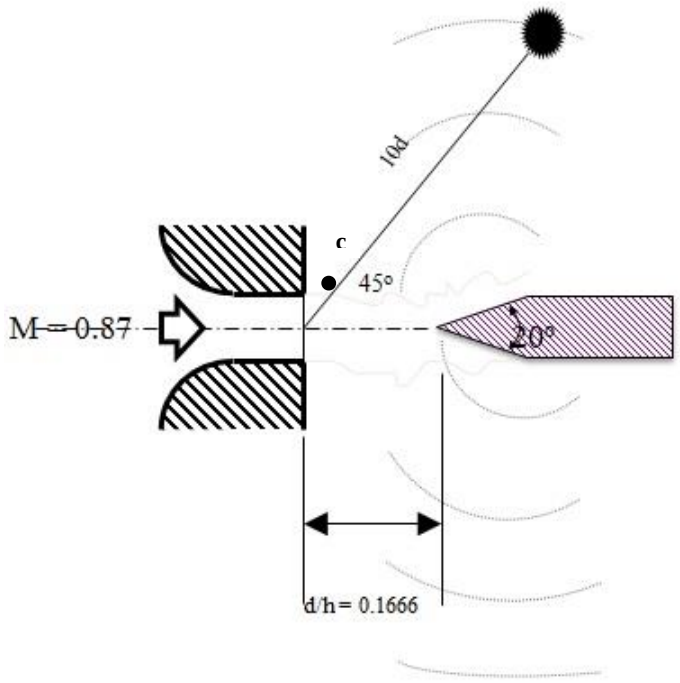

Figure 5-6: Schematic of acoustic receiver location for high speed edge-tone models

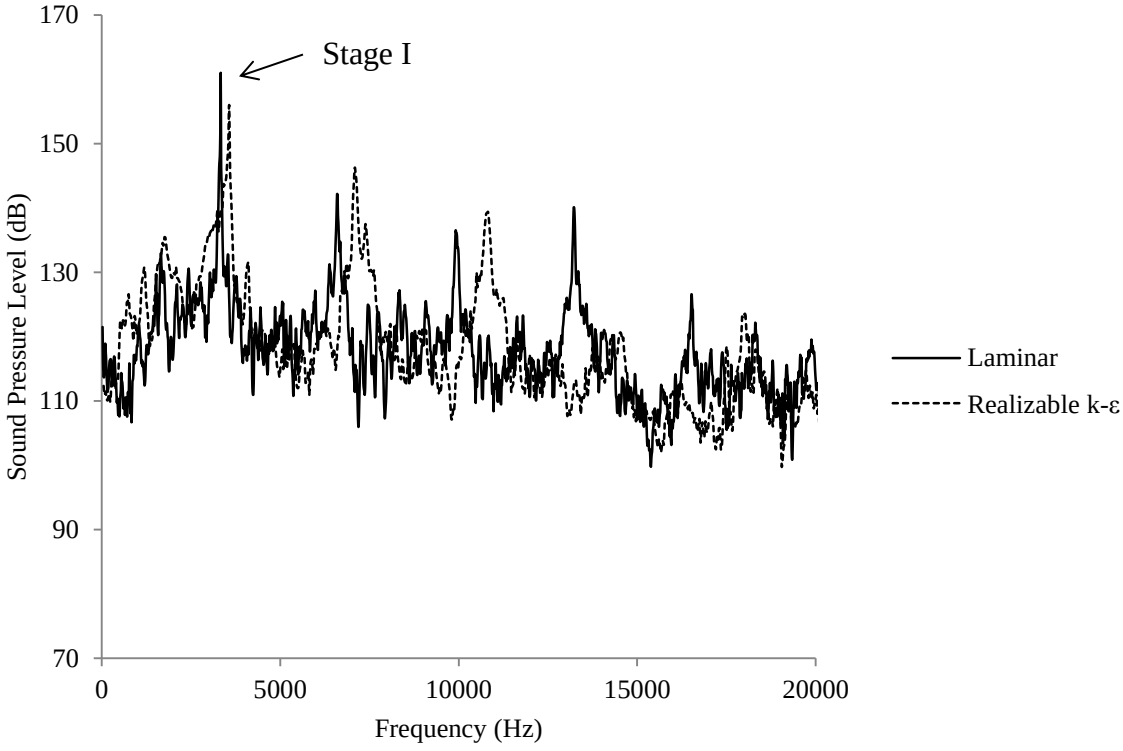

Figure 5-7: SPL spectra for the case with *d/h* = 0.1666 and *M* = 0.87 (Stage I-Point A is shown in Fig. 5-1)

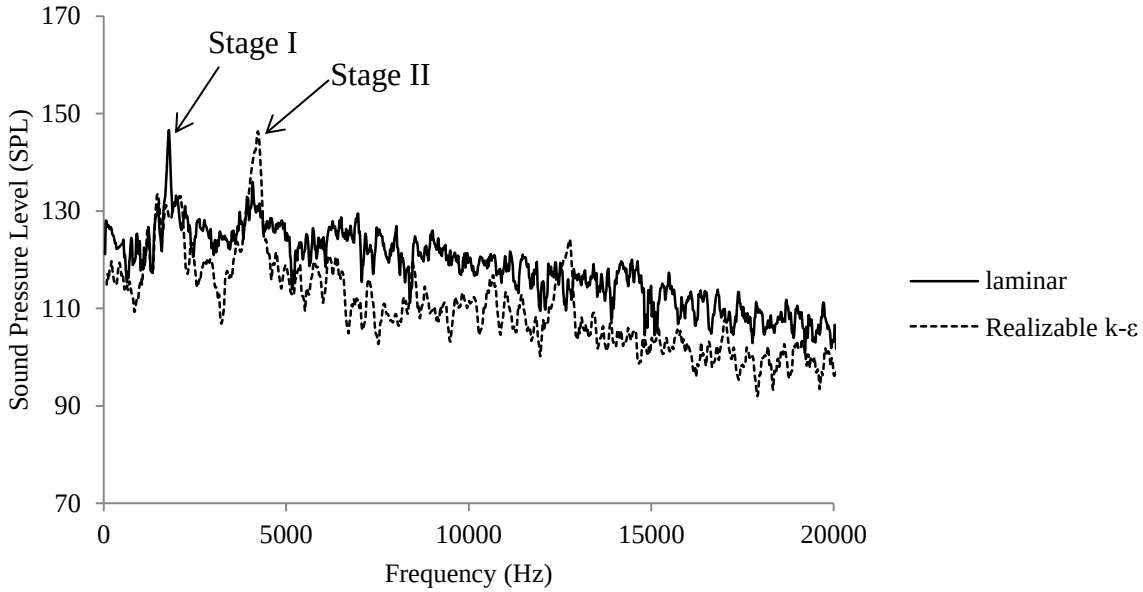

Figure 5-8: SPL spectra for the case with *d/h*= 0.0869 and *M* = 0.87 (Stage II-Point B is shown in Fig. 5-1)

SPLs are higher in laminar flow case compared to the turbulent case, which is in agreement with the numerical investigation conducted by Buhler *et.al* [47]. This is because for laminar flow, shear layer is developed by the laminar turbulent transition associated with the Kelvin-Helmholtz instabilities, which ultimately causes the turbulent breakdown of the jet. While in turbulent flow, the jet flow advancement is identified by rapid changeover of the turbulent wall boundary layer to the turbulent free shear layer at downstream of the nozzle exit. So difference in SPL between laminar and turbulent flow might be related to the different structure of the generated sound [47]. In laminar flow, the sound captured by acoustic receiver is governed by the upstream propagating acoustic waves emitted around the closing of the potential core. While in case of turbulent flow, fine scale turbulent structures are present in the jet shear layer such that the sound radiation in the acoustic receiver location is present immediately downstream of the nozzle exit [47]. The large scale coherent structures developing in the jet shear layer in

laminar flow (Kelvin-Helmholtz instabilities) can be considered as more efficient sound radiators than the turbulent fluctuations within the shear layer in case of turbulent flow model [47]. The velocity divergence contours are used to show the sound wave source and propagation. It can be interpreted from the continuity equation of compressible flow as written in Eq. (5.3). The RHS of Eq. (5.3) indicates the change in density ratio of fluid flow. Hence, minor change in density caused by wave emission can be easily seen in the velocity divergence contours [48]. The velocity divergence is computed in FLUENT from the numerically obtained velocity field.

$$\nabla.\vec{V} = -\frac{1}{\rho}\frac{D\rho}{Dt} \tag{5.3}$$

Fig. 5-9 and Fig. 5-10 shows the velocity divergence contours for laminar flow model and realizable k-ε turbulence flow model, respectively for the case of d/h = 0.1666. Near the wedge tip, the velocity divergence takes a large value, where jet impingement takes place. From these figures, the downstream and upstream propagating waves are depicted. Large scale structures and vortex size in using laminar flow model is greater than the realizable k-ε turbulence flow model. The wedge tip of laminar flow model has more region of high velocity divergence than the realizable k-ε turbulence flow model. It indicates that the laminar flow model has more intense sound emission than the turbulent case which is in agreement with the numerical investigation of Buhler *et.al* [47]. Hence, the sound pressure level of realizable k-ε turbulence flow model is slightly lesser than the laminar flow model. Based on the above results, the flow is examined as 2-D and laminar compressible flow that is persistent with the experimental observations. The transition to turbulence which is found occasionally in experiments does not affect the initial vortices created on the edge [16].

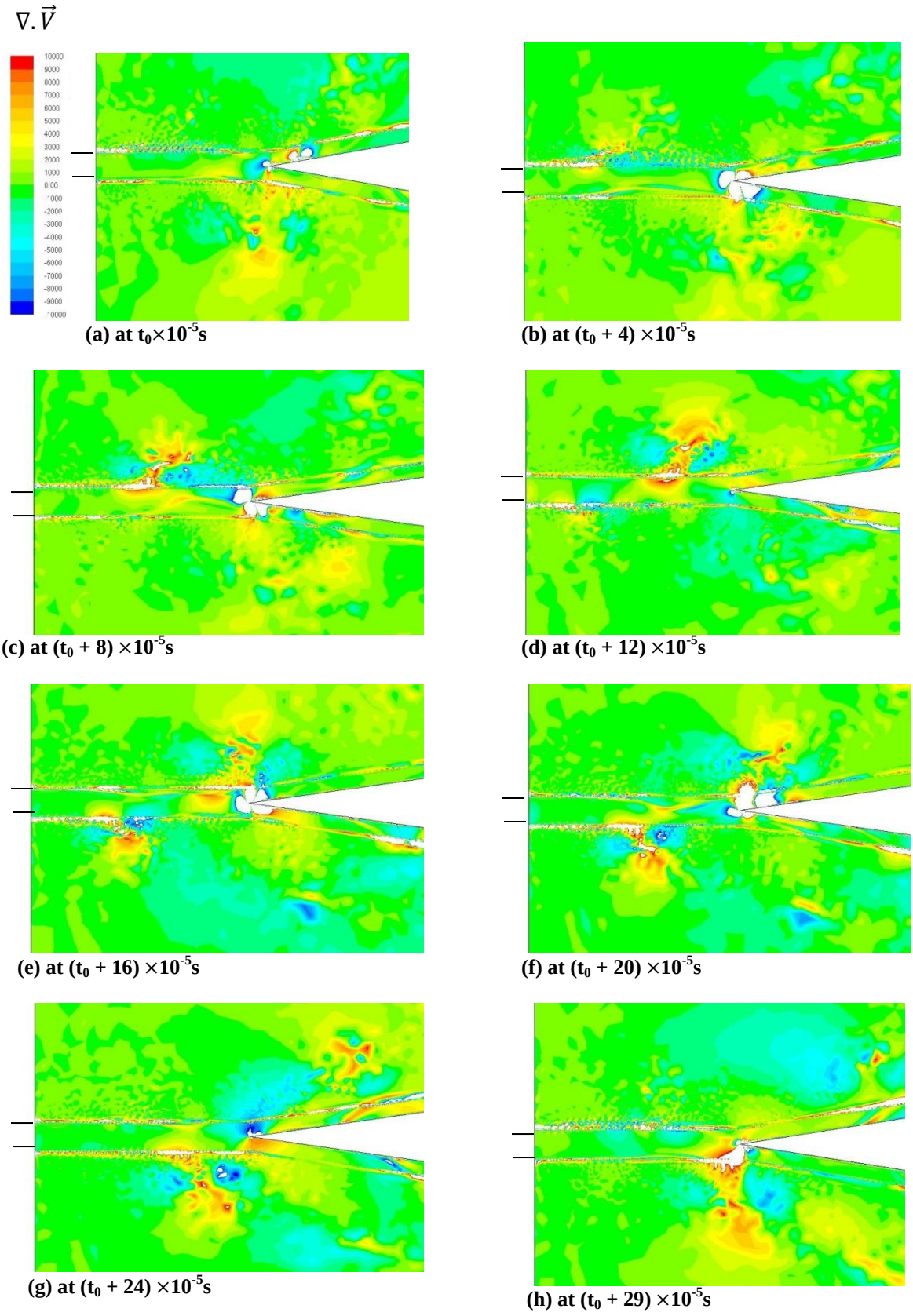

Figure 5-9: Contours of the velocity divergence for laminar flow model computations at *d/h*=0.166 and *M*=0.87

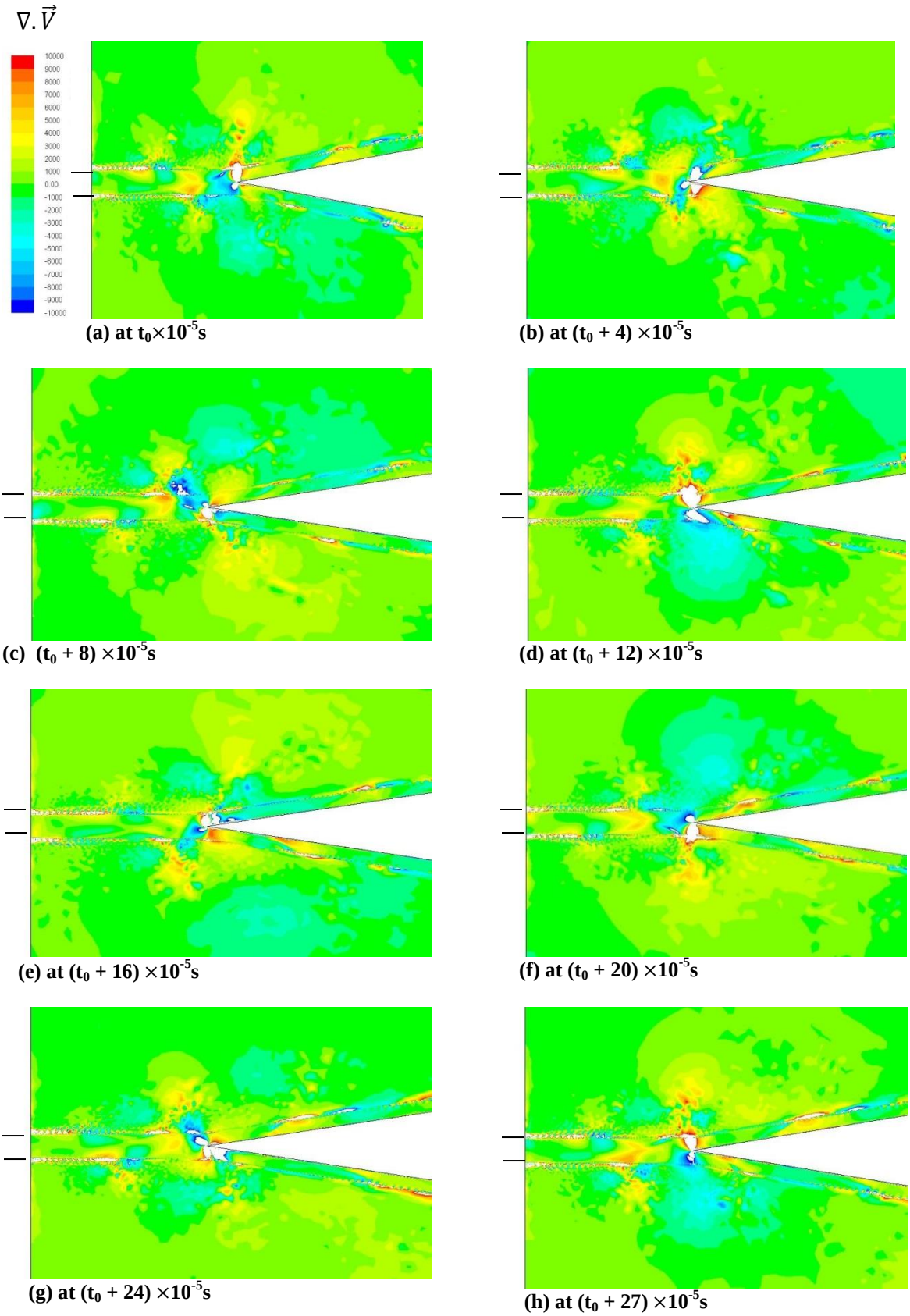

(a) at $t_0 \times 10^{-5}$s **(b) at $(t_0 + 4) \times 10^{-5}$s**

(c) $(t_0 + 8) \times 10^{-5}$s **(d) at $(t_0 + 12) \times 10^{-5}$s**

(e) at $(t_0 + 16) \times 10^{-5}$s **(f) at $(t_0 + 20) \times 10^{-5}$s**

(g) at $(t_0 + 24) \times 10^{-5}$s **(h) at $(t_0 + 27) \times 10^{-5}$s**

Figure 5-10: Contours of the velocity divergence for realizable k-ε turbulence flow model computations at *d/h*=0.166 and *M*=0.87

Hence, turbulence has small importance on both the edge-tone frequency and feedback loop [16]. From Fig. 5-1, it is clearly evident that the realizable k-ε turbulence flow model has almost the same values of edge-tone frequencies as the laminar flow model. Moreover, from the experiment observations of Krothapalli *et.al* [40] it can be concluded that the edge-tone, which is a discrete frequency, attributed to the laminar portion of the jet shear layers. Hence, the numerical data of edge-tone simulations using laminar flow model agrees very well with the experimental data of edge-tone. So, laminar flow model is used to simulate all high speed cases in this present study to examine edge-tones.

5.2 Parametric Study

5.2.1 Compressibility Effect

The effect of compressibility or jet exit Mach number, on the edge-tone and the associated flow-field are considered in this section. It is expected that the effect of Mach number will affect the downstream propagation disturbances velocity as can be deduced from Powell's Eq. (2.4). Four cases of different Mach numbers are computed for high speed jet numerical model. All the cases is for $d/h = 0.1666$ and angle of wedge is 20^{o}, same as the experimental cases of Krothapalli. *et.al* [13] for comparison and it is shown in Table 5-2. The effect of Mach number on edge-tone frequency is shown in Fig. 5-11. Powell [12] proposed a feedback loop equation to predict the edge-tone frequency as explained in Eq. (2.4). From these data, phase lag p is calculated using Eq. (2.4) by considering average jet disturbance velocity, U_c, in Eq. (2.5) as constant and equal to half of the main jet velocity, U_j. Then average phase lag value is found out to be -0.35.

Table 5-2: Cases studied at different Mach numbers

d/h	Mach Number	The computed edge-tone frequency (Hz)	Experimentally observed edge-tone frequency (Hz) [13]	% Error $\left[\frac{Exp.Freq - Comp.Freq}{Exp.Freq}\right]\times 100$
0.1666	0.3	1667	-	
0.1666	0.53	2498	2800	10.7
0.1666	0.87	3333	3600	7.4
0.1666	0.93	3592	3900	7.9

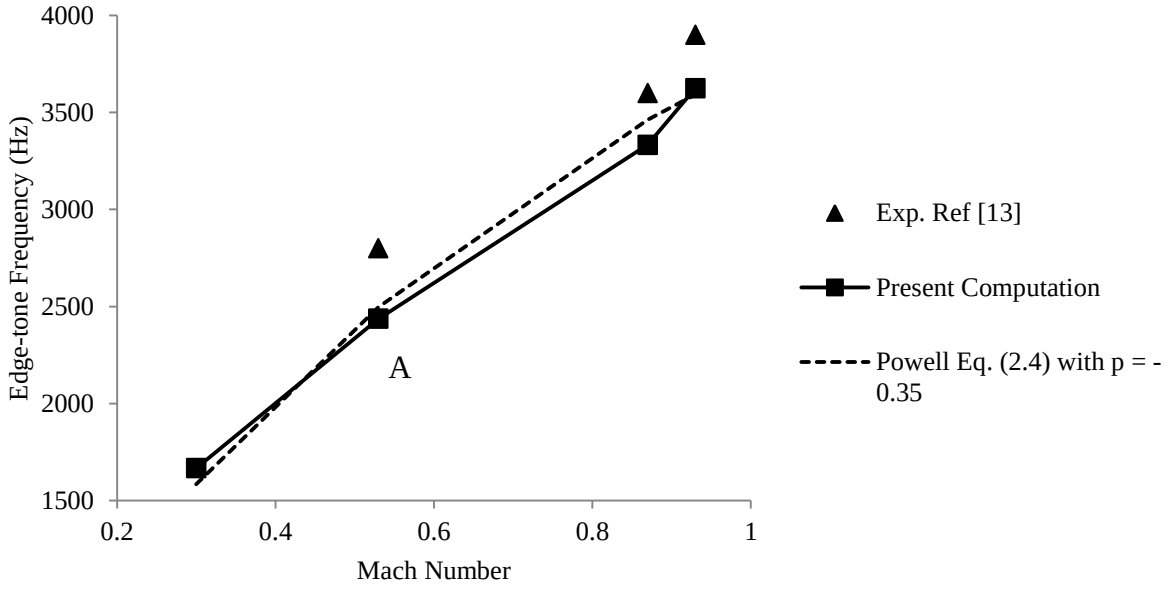

Figure 5-11: Compressibility effect study – edge-tone computations at acoustic field point

Edge-tone frequencies computed at acoustic field using FLUENT simulation, Powell's theoretical formula and experimental edge-tone data [13] are shown in Fig. 5-11 which indicates that edge-tone frequency increases as Mach number increases. It can be explained by analyzing the downstream and upstream acoustic wave propagations. As Mach number increases, the time required for downstream propagation (T_1) decreases and the total value of T_1+T_2 in Eq. (2.4) decreases that causes the increase in edge-tone frequency as shown in Fig. 5-12. Sound Pressure Level (SPL) for all the cases are

captured by receiver located at the place depicted in Fig. 5-6 and the SPL values of case where Mach number is 0.53 (presented in Fig. 5-11) is shown in Fig. 5-13.

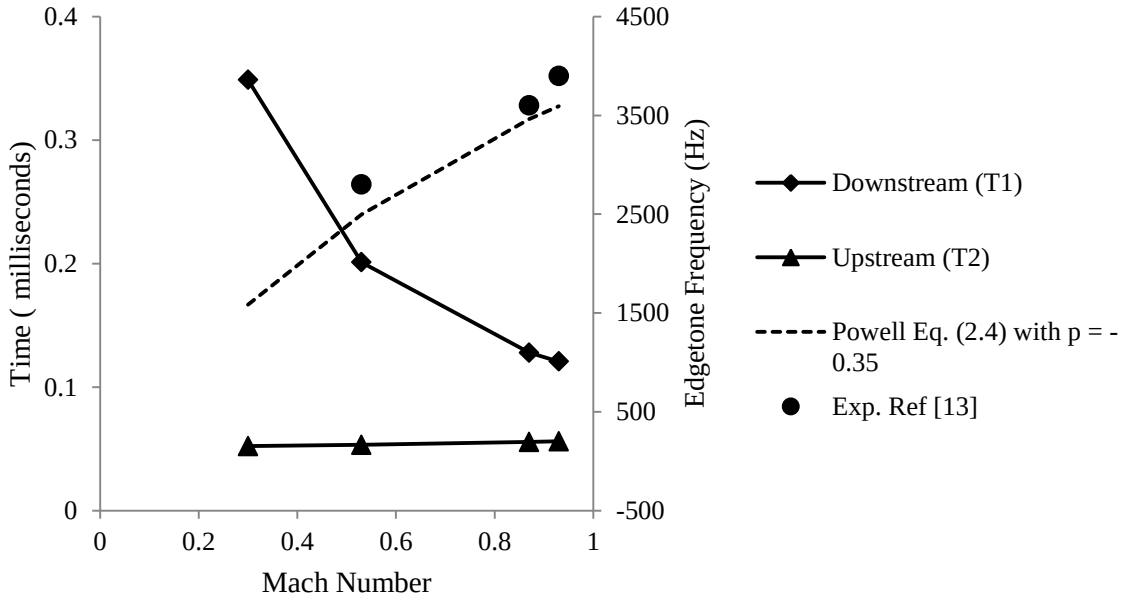

Figure 5-12: Downstream and upstream propagation times of edge-tone frequency computations at acoustic field point

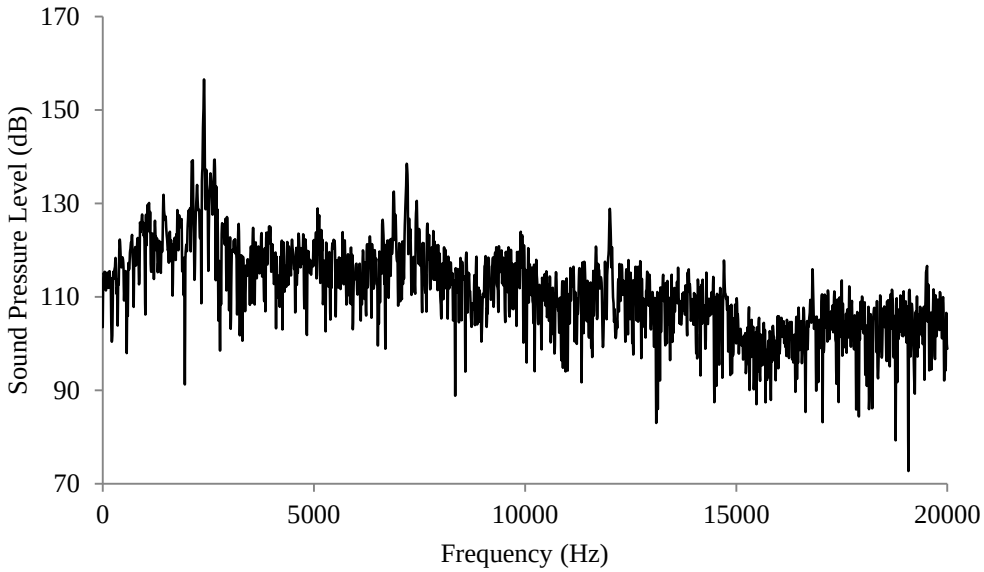

Figure 5-13: SPL spectra for the case with *d/h* = 0.1666 and *M* = 0.53 (Stage I-Point A is shown in Fig. 5-11)

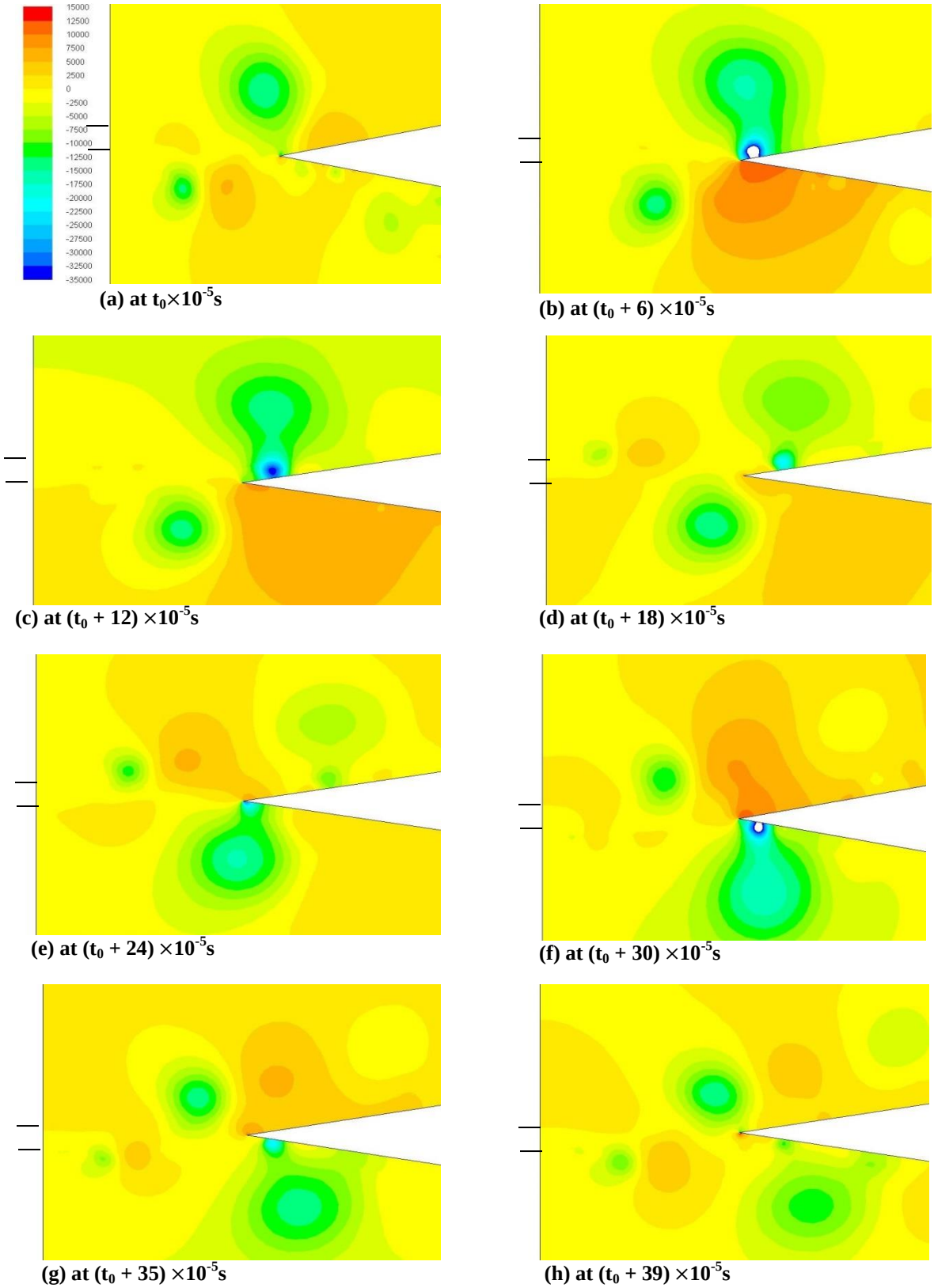

Figure 5-14: Static pressure contours for laminar flow model at *d/h*=0.166 and *M*=0.53

Static pressure contours for the case of Mach number 0.53 are shown in Fig. 5-14. Dipole sound source is clearly visible near the wedge tip and it is clearly evident from the static pressure contours where the low and high pressure regions are located.

5.2.2 Wedge Angle Effect

The effect of wedge angle on edge-tone has been analyzed for high speed jets at different stand-off distances for three different wedge angles of 20°, 60° and 180°. The flow conditions used to analyze the effect of wedge angle at different stand-off distances are listed in Table 5-3.

Table 5-3: Cases studied at different stand-off distances to investigate the wedge angle effect

d/h	**Mach Number**	**The computed edge-tone frequency (Hz)**		
		20°	**60°**	**180°**
0.1818	0.87	3888	3935	4352
0.1666	0.87	3333	3611	4444
0.1428	0.87	3055	3150	3796
0.0952	0.87	4351	4739	2315
0.0869	0.87	4074	4351	1945
0.0800	0.87	3888	3981	1480

All cases are performed at Mach number of 0.87 and at slit width 3 mm, which is same as the experimental data of Krothapalli *et.al* [13]. The results are shown in Fig. 5-15. For a jet with constant Mach number, the edge-tone frequency decreased steadily as the stand-off distance increased above the minimum breadth. This frequency persist to decrease up to certain stand-off distance is achieved where the edge-tone will abruptly changes to a new higher frequency. As the stand-off distance increased further, this action is repeated again and again which is known as the "Staging" phenomenon. From Eq. (2.4) the stage number abruptly changes when certain Mach number or stand-off distance is achieved which leads to staging phenomenon.

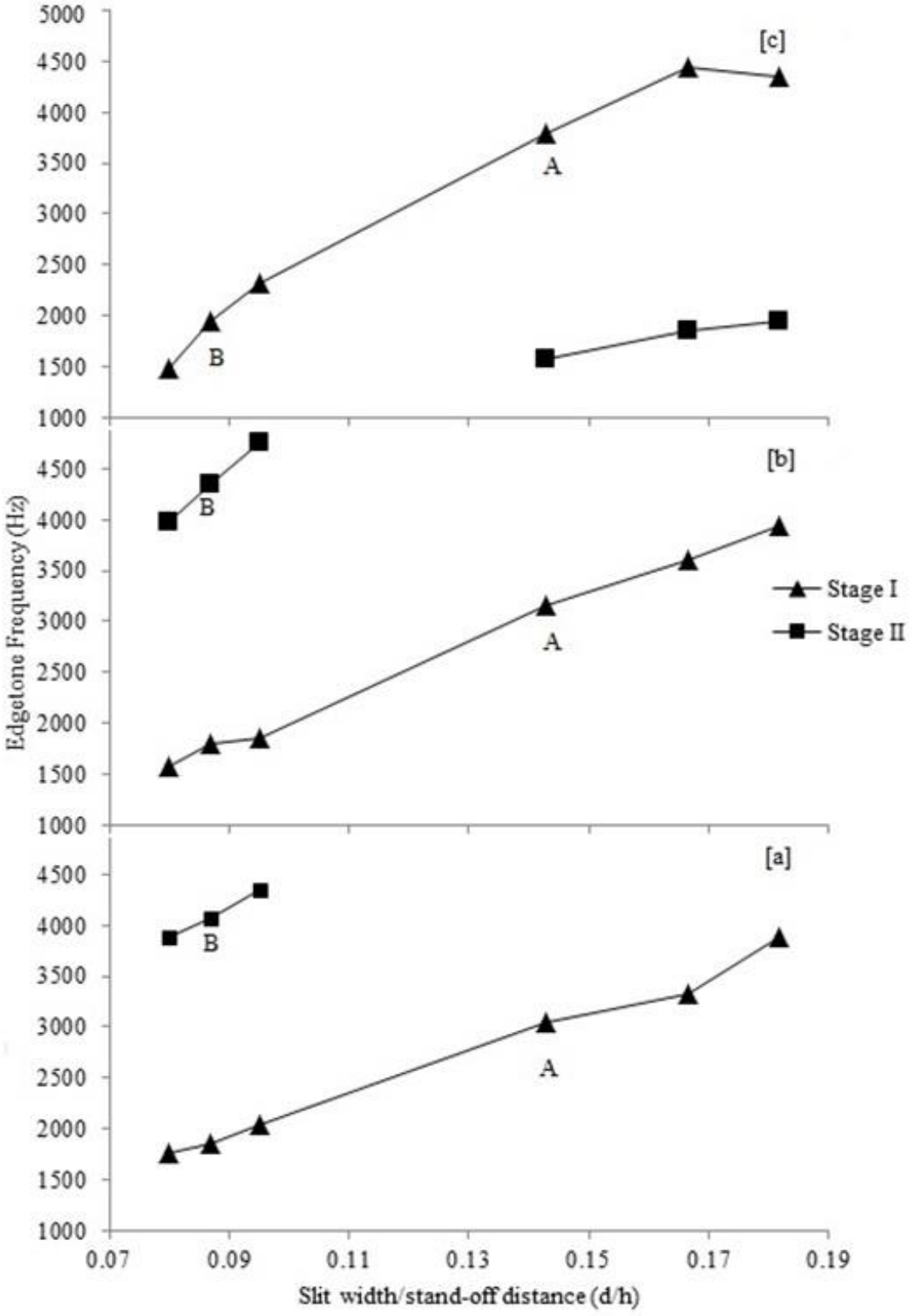

Figure 5-15: Staging phenomena for wedge angles; [a] 20° [b] 60° and [c] 180°

Edge-tone frequencies showed similar trend (i.e. as the stand-off distance increased edge-tone frequency decreased steadily) of staging phenomenon for wedge angles 20° and 60°. Stage II appeared for both wedge angles of 20° and 60° where *d/h* is 0.0952. In the case of wedge angle 180° (impingement on a plate) impingement frequency decreased as stand-off distance increased and lower stage of frequency occurred at earlier stage but it is diminish. The reason behind this tendency for the case of wedge angle having 180° is not clear and needs further investigations. Flow oscillations matched with the dominant frequency of higher stage. Sound Pressure Level (SPL) of cases A and B (shown in Fig. 5-15) are captured with a receiver depicted in Fig. 5-6. It is presented in Fig. 5-16 and Fig. 5-17 for different wedge angles of 20°, 60° and 180°. For a given exit Mach number and stand-off distance, the edge-tone frequency increases and amplitude decreases as wedge angle increases as shown in Fig. 5-16 and 5-17.

The static pressure contours for two wedge angles of 60° and 180° are shown in Fig. 5-18 and Fig. 5-19. In edge-tone systems, the period of flow-field oscillations should be equal to the reciprocal of edge-tone frequency. From Fig. 5-18, it is evident that period of flow-field oscillations is 0.000027 *s*, which is reciprocal of 3611 Hz. From Fig. 5-19, it is evident that period of flow-field oscillations is 0.000022 *s*, which is reciprocal of 4444 Hz. For wedge angle 60°, the flow oscillations are similar to the case of wedge angle 20°. For the special case of wedge angle 180° (i.e. impingement on a plate), the flow oscillations are matched with its impingement tone frequency. Impinging tone is a discrete sound generated when a jet impinges on a flat plate placed at a short distance from the nozzle exit. Similarly, edge-tone is a special type of impinging tone and it is produced when jet impinges on a sharp edge corner of a wedge instead of a flat plate.

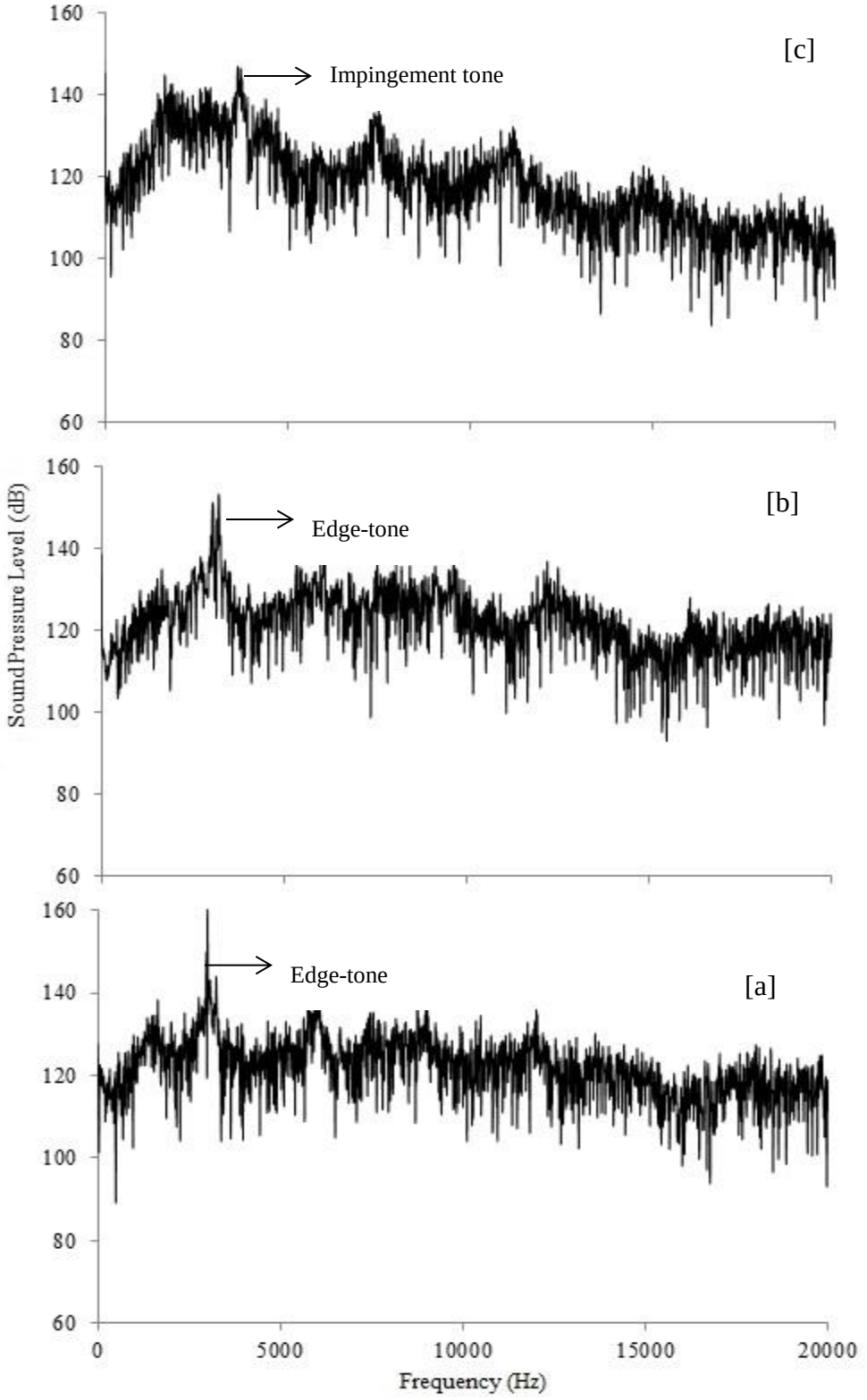

Figure 5-16: SPL spectra for the cases with *d/h* = 0.1428 and *M* = 0.87 and wedge angles; [a] 20°, [b] 60° and [c] 180° (Stage I-point A presented in Fig. 5-15)

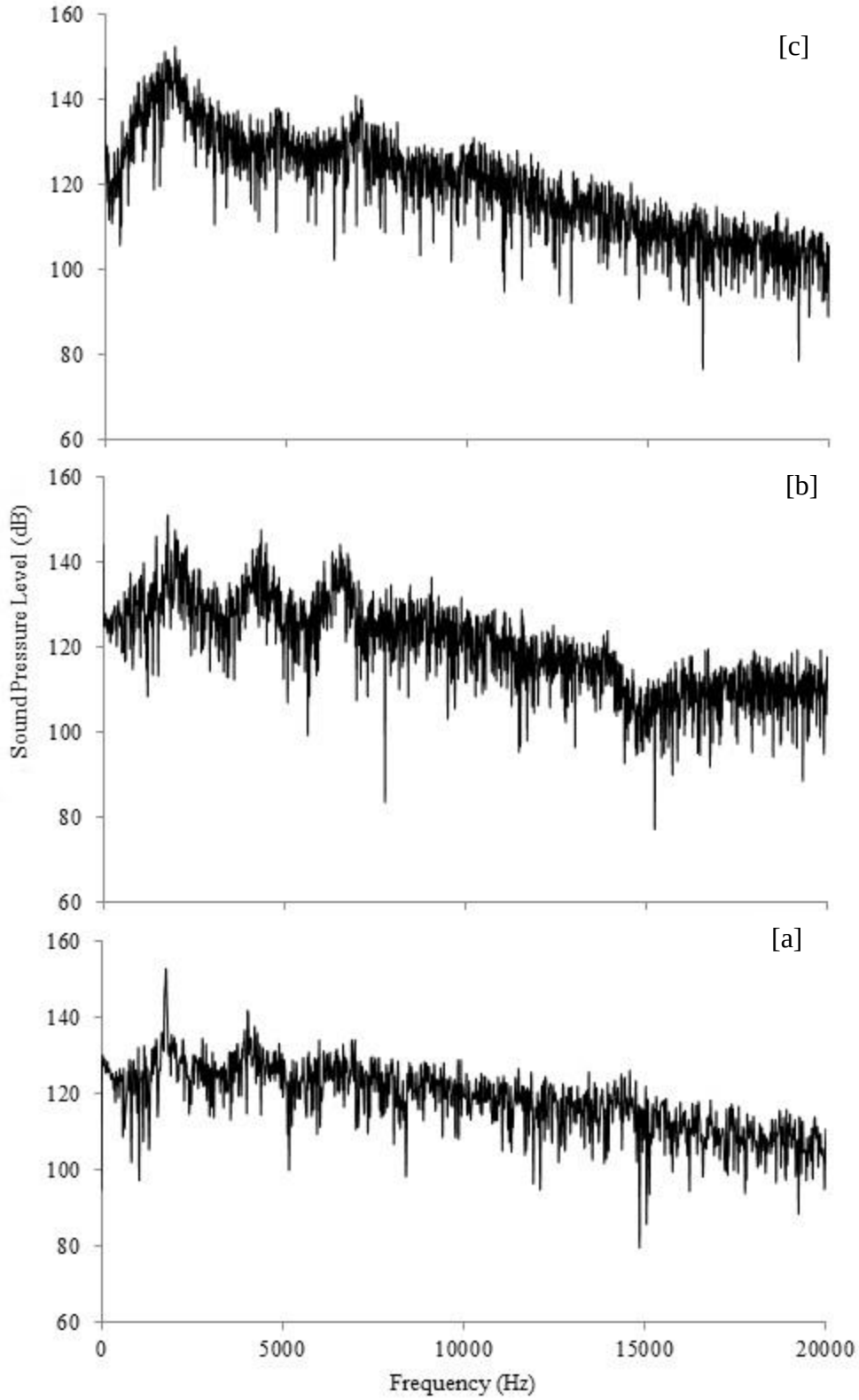

Figure 5-17: SPL spectra for the cases with *d/h* = 0.0869 and *M* = 0.87 and wedge angles; [a] 20°, [b] 60° and [c] 180° (Stage II-point B presented in Fig. 5-15)

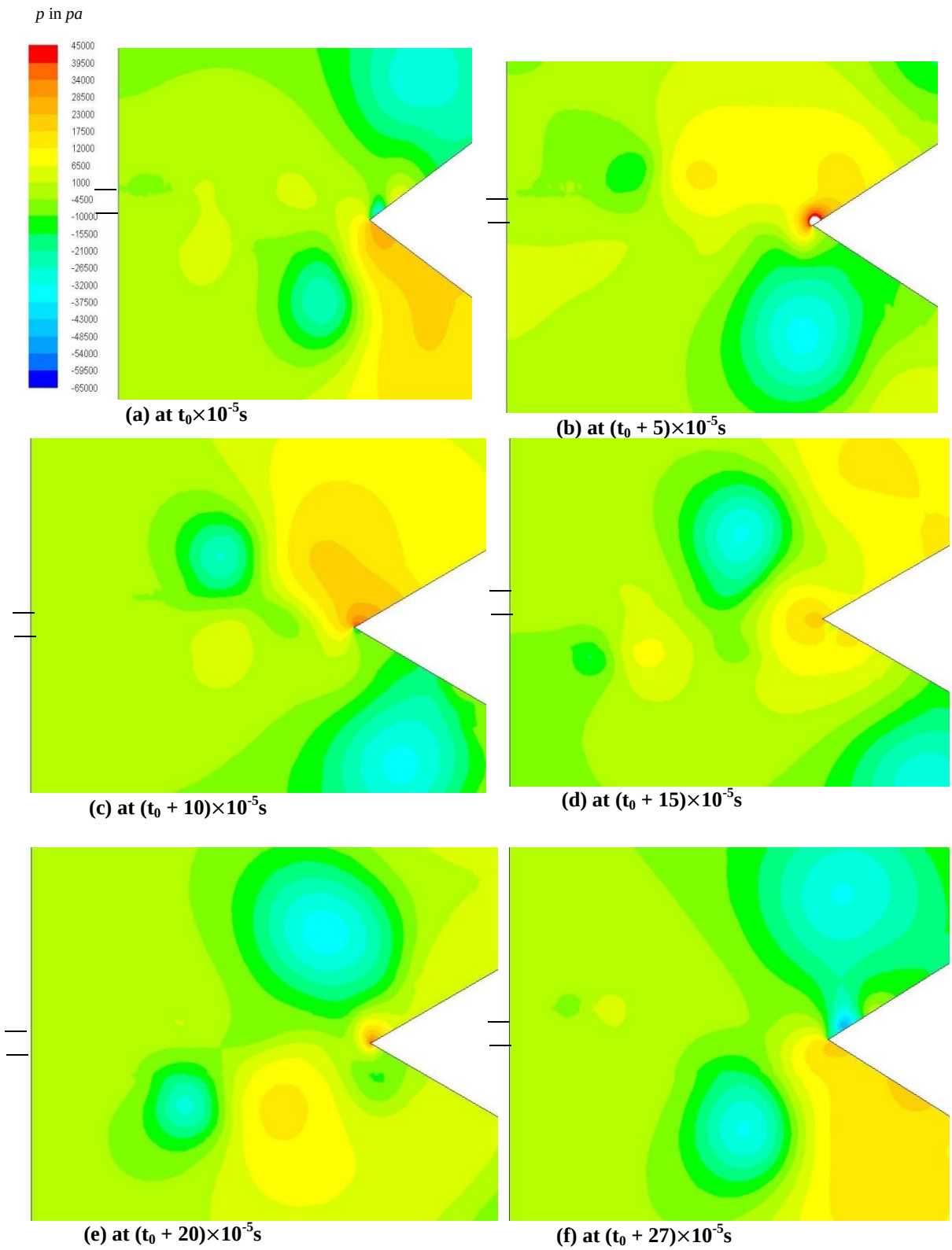

Figure 5-18: Static pressure contours for wedge angle 60^0, M = 0.87 at d/h = 0.1666

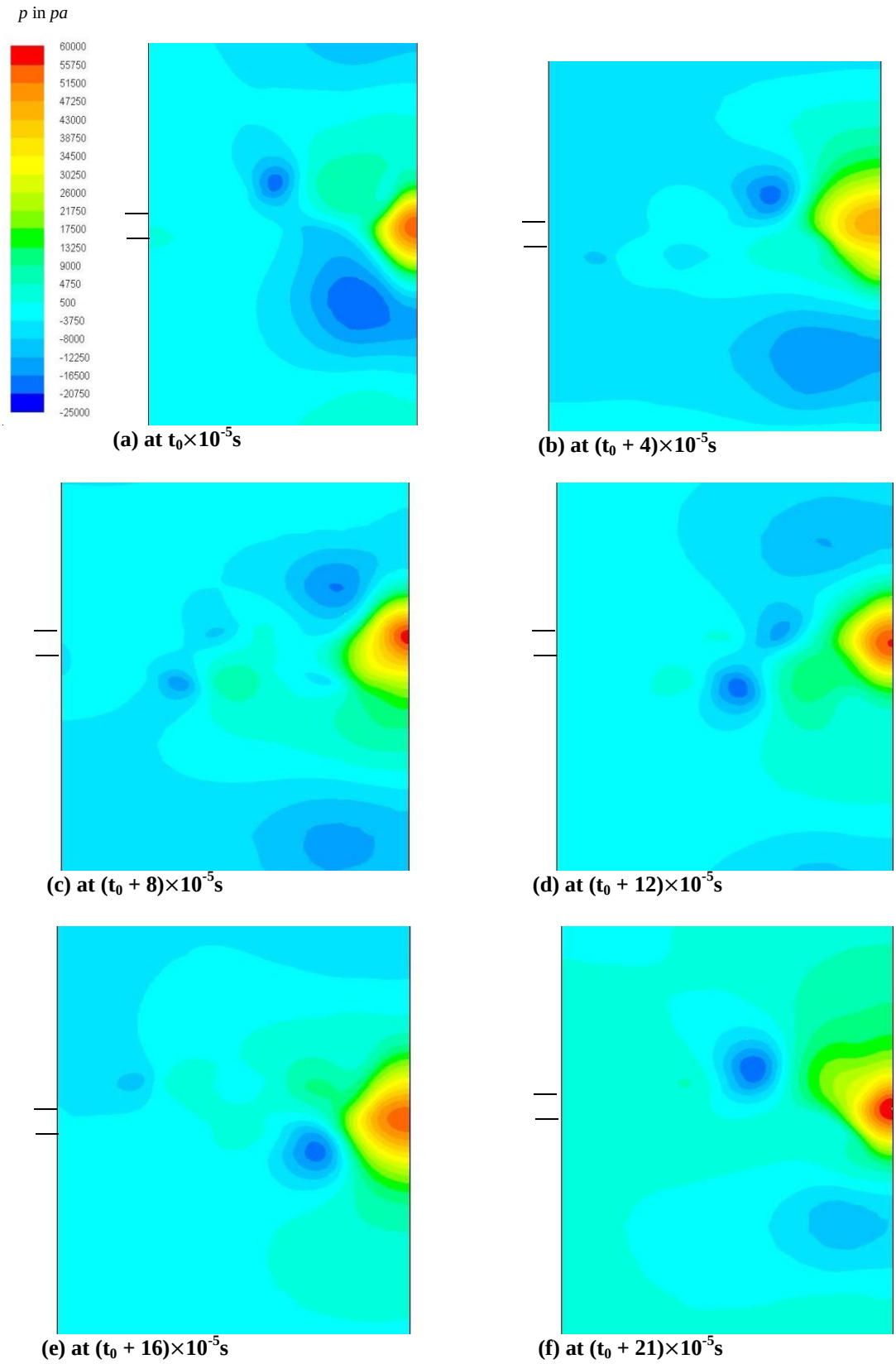

(a) at $t_0 \times 10^{-5}$s **(b) at $(t_0 + 4) \times 10^{-5}$s**

(c) at $(t_0 + 8) \times 10^{-5}$s **(d) at $(t_0 + 12) \times 10^{-5}$s**

(e) at $(t_0 + 16) \times 10^{-5}$s **(f) at $(t_0 + 21) \times 10^{-5}$s**

Figure 5-19: Static pressure contours for wedge angle 180^0, M = 0.87 at d/h = 0.1666

5.2.3 Shear Layer Thickness Effect

In this shear layer thickness effect study, the main objective is to find the phase lag value, *p*, for high speed edge-tone test cases using the most reliable method of Karamcheti *et al.*[11]. Using this method, Nonomura *et al.* [30] proved that the phase lag value, *p*, is -0.2 for low speed edge-tones. So in this parametric study top hat velocity profiles are used to calculate the phase lag value, *p*, for high speed edge-tone test cases. Top hat velocity profiles can be represented using the following equation

$$U(r) = 0.5\left\{1 + \tanh\left[0.25\frac{R}{\theta}\left(\frac{R}{r} - \frac{r}{R}\right)\right]\right\} \tag{5.4}$$

where

θ is the momentum thickness which is defined as

$$\theta = \int_0^\infty \left(\frac{\rho(r)}{\rho_0}\right)\left(\frac{U(r)}{U_0}\right)\left(1 - \frac{U(r)}{U_0}\right) \tag{5.5}$$

R is the jet radius

r is the local point radius, *x(R)*

At the inlet, the momentum thickness (θ) is changed in order to vary the shear layer thickness. High speed jet at Mach number of 0.87 is considered for computations. All the cases are performed at *d/h* = 0.1666 and wedge angle of 20^0 similar to the experiments of Krothapalli *etl.al* [13]. Five different cases of momentum thickness (θ) are considered, specifically; 0.004 R, 0.04 R, 0.1 R, 0.2 R, 0.4 R. The top hat velocity profiles for these four cases are shown in Fig. 5-20.

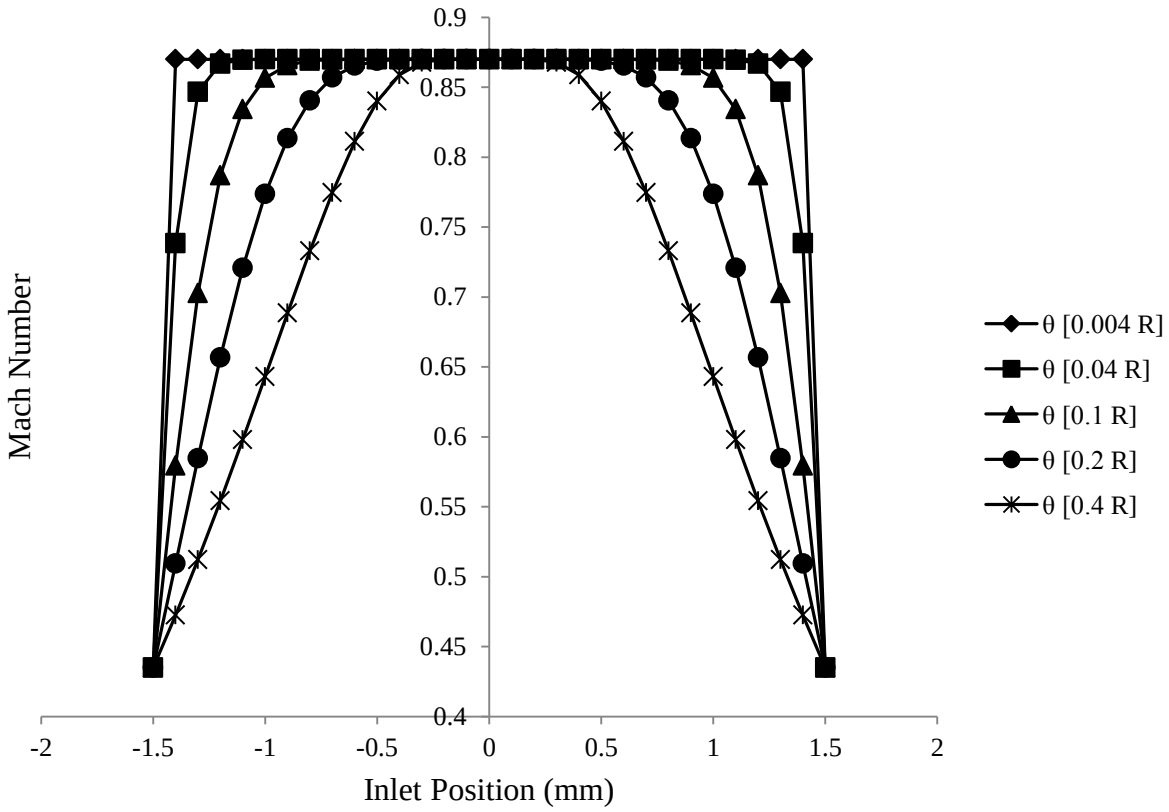

Figure 5-20: High speed top hat velocity profiles for different momentum thicknesses (M = 0.87 and $\dot{m}$ = 1.145)

Phase computations are made by using the fluctuation of lateral velocity components along the centerline of jet at *x/h*, specifically; 0, 0.16, 0.33, 0.50, 0.66, 0.83 and 1. The phases at different locations are computed relative to the phase at the slit and presented in Fig. 5-21. As the *x/h* value reaches 1, the phase variation along the centerline of the lateral velocity components also increases. To confirm the Powell's feedback loop mechanism quantitatively, phase lag *p* is computed and examined. The data obtained from Fig. 5-21 is used to calculate the jet disturbance convection speed (U_c) using Eq. (5.1) and it is shown in Fig. 5-22. It shows that the convection of jet-disturbance is nonlinear and the convective jet disturbance speed near the nozzle is higher than that in the downstream.

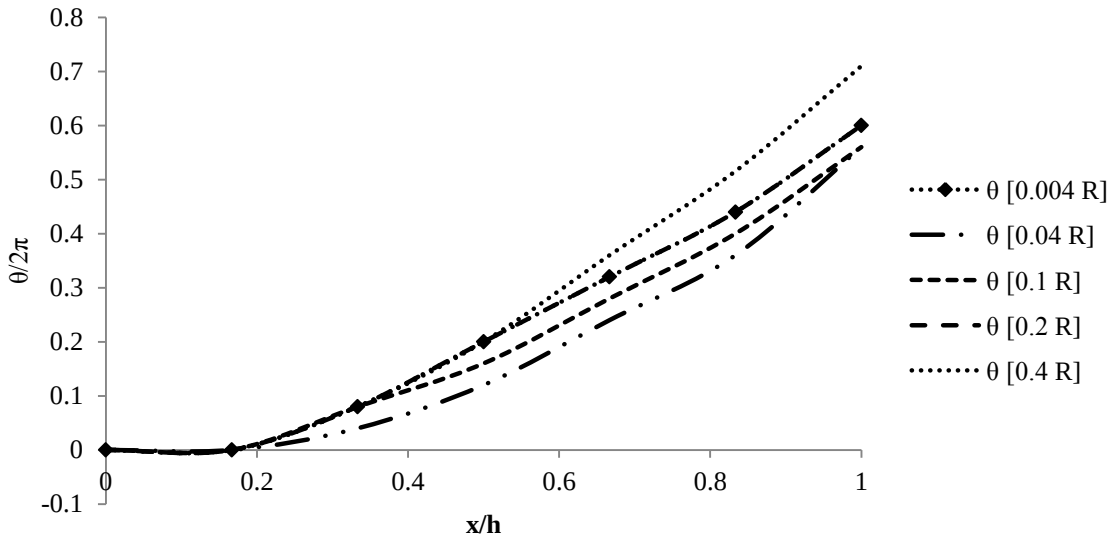

Figure 5-21: Phase variation for different momentum thicknesses of top-hat velocity profiles (M = 0.87 and $\dot{m}$ = 1.145)

Using Eq. (2.5) the downstream propagation time, T_1 and upstream propagation time, T_2 is calculated. As the momentum thickness increases, convective speed of jet disturbance decreases along the stand-off distance. It indicates that downstream propagation time increases as momentum thickness increases. For the momentum thickness cases of 0.004 R, 0.04 R, 0.1 R, 0.2 R and 0.4 R, the downstream propagation times are 0.0002*s*, 0.00016*s*, 0.00016*s*, 0.00017*s*, and 0.00018*s*, respectively. Then, phase lag p is computed from Eq. (2.4), where stage number n, edge-tone frequency f from present study (shown in Fig. 5-24) and whole edge-tone period of feedback loop (T_{LOOP}) are obtained from computational study. Fig. 5-23 shows the relation between Strouhal number St and $1/T_{LOOP}$ calculated from the present results where the solid line shows the result of $p = -0.1$. Edge-tone frequency calculated from Powell's Eq. (2.4) with assumption of $U_c = 0.5U_j$ and $p = -0.35$ is shown as well. The present results prove that the phase lag $p = -0.1$ and it is constant for high speed edge-tone test cases. The case that phase lag is almost constant indicates that the Powell's feedback loop Eq. (2.4) is physically correct.

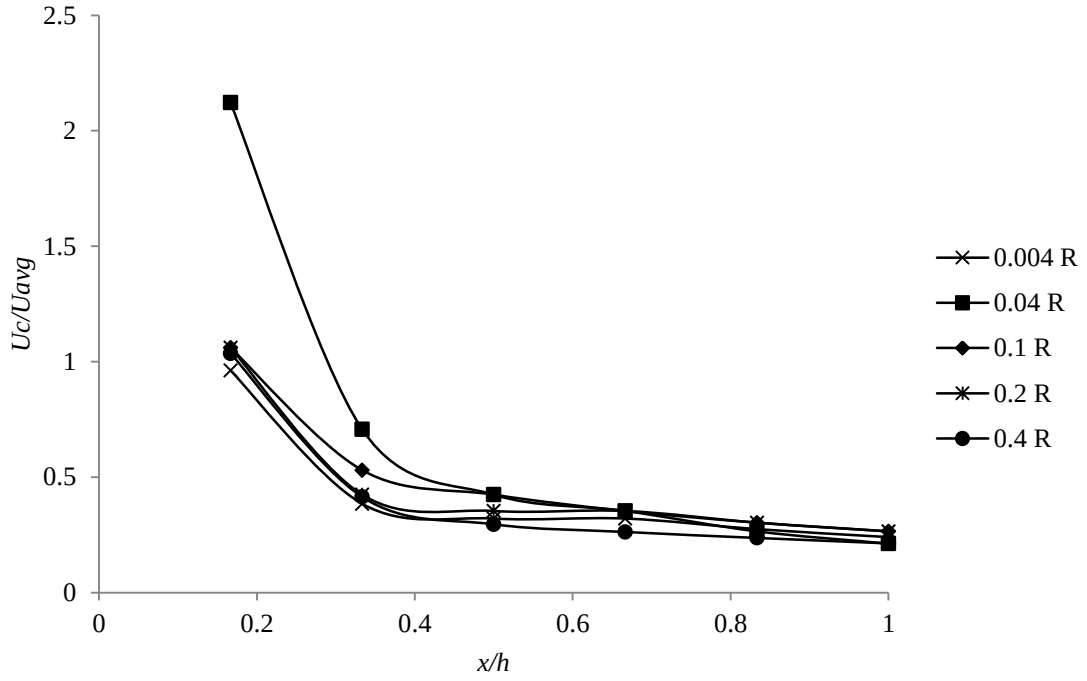

Figure 5-22: Variation of jet disturbance convective speed along the stand-off distance for different momentum thicknesses (M = 0.87 and $\dot{m}$ = 1.145)

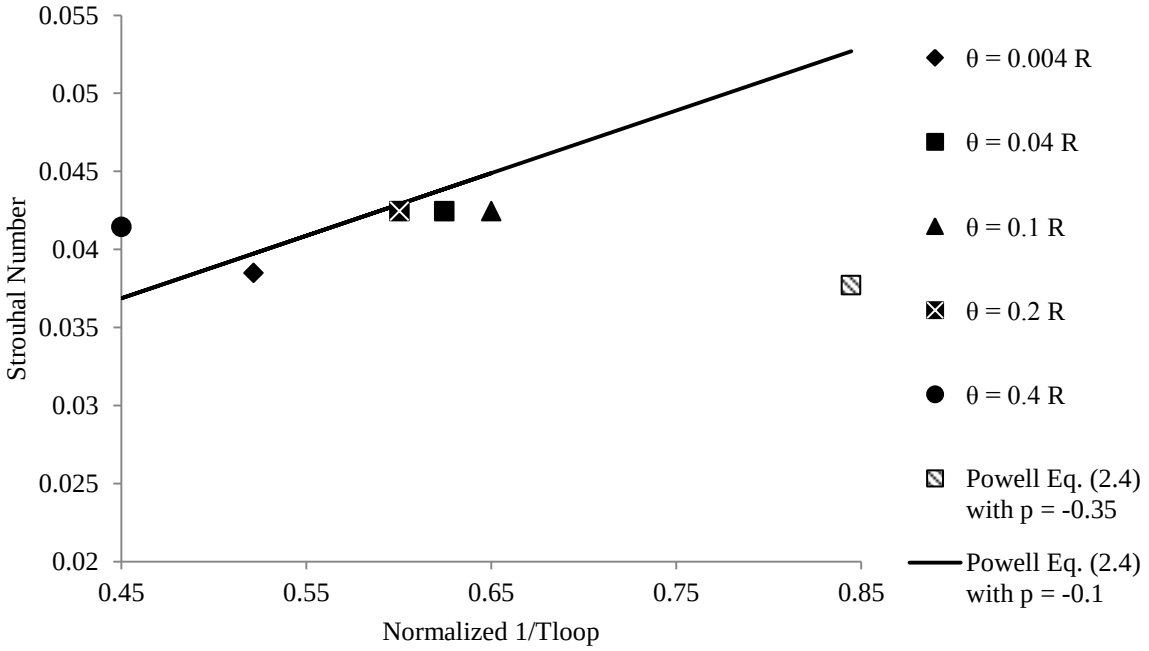

Figure 5-23: Relation between Strouhal number and whole edge-tone period of feedback loop along with Powell's feedback loop equation assuming $p = -0.1$ ($U_c \neq 0.5U_j$) and $p = -0.35$ ($U_c = 0.5U_j$)

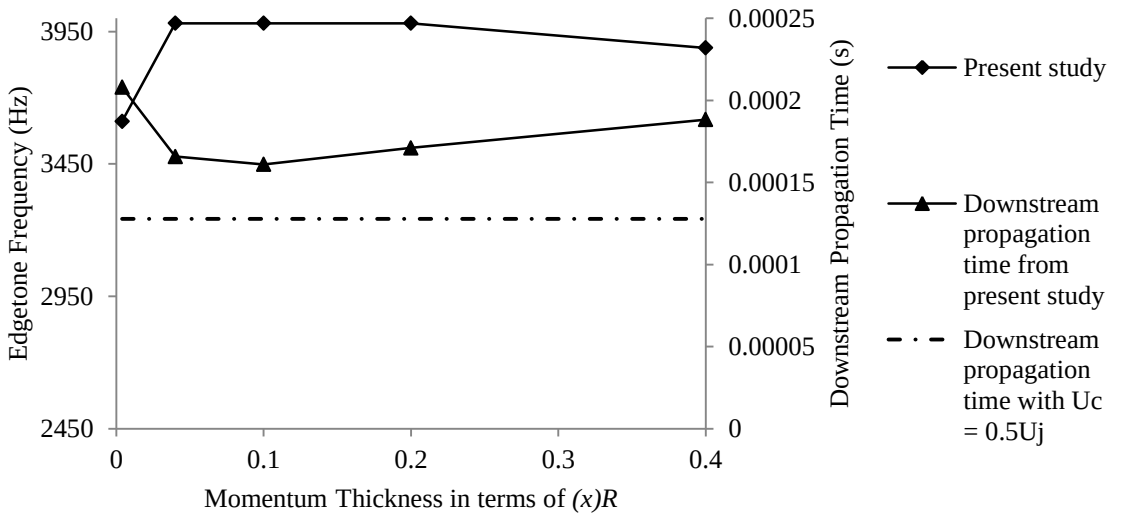

Figure 5-24: Shear layer thickness effect on edge-tone frequency from present study and downstream propagation times with $U_c \neq 0.5U_j$ and $U_c = 0.5U_j$ at $M = 0.87$

Fig. 5-24 shows the effect of shear layer thickness on edge-tone frequency from present study and downstream propagation time (T_1) in high speed jets. T_1 calculated by assuming $U_c = 0.5U_j$ is shown as well. By comparing this with T_1 calculated from present study, it is evident that $U_c \neq 0.5U_j$ in real cases. As the shear layer thickness increased, the edge-tone frequency decreased gradually. The maximum edge-tone frequency is produced by the momentum thickness (θ) of 0.04 R. Greater momentum thickness indicates more mixing occurring in the flow-field. As the momentum thickness increases, convective speed of jet disturbance decreases monotonically along the stand-off distance as shown in Fig. 5-22. It indicates that downstream propagation time, T_1, increases from Eq. (2.5) which causes the edge-tone frequency to decrease from Eq. (2.4). Minimum edge-tone frequency is observed for the momentum thickness of 0.004 R, because the downstream propagation time is high.

5.2.4 Nozzle Lip Thickness Sensitivity Study

Five different types of nozzle lip thickness are considered as shown in Table 5-4 in order to examine its effect on edge-tone phenomenon. Nozzle lip thickness refers to the

thickness of the nozzle wall at the jet exit as shown in Fig. 4-6. It has considerable effect on edge-tone frequency and the phenomenon is studied in detail in this section. The grid is constructed similar to the models of high speed jet cases considered for validation described in chapter 4. All the cases are performed at wedge location where *d/h* is 0.1666, angle of wedge 20° and Mach number of 0.87. As the nozzle lip thickness increases, the edge-tone frequency decreased and the SPL of edge-tone frequency increased. At a certain nozzle lip thickness frequency decreased rapidly compared to the other nozzle lip thickness cases. Edge-tone sound pressure level (SPL) of all the cases are also shown in Fig. 5-25.

Table 5-4: Cases studied at different nozzle lip thickness

Slit width/Nozzle lip thickness (d/t_{nl})	**Mach number**	**The computed edge-tone frequency (Hz)**
0.0686	0.87	3657
0.0668	0.87	3611
0.0660	0.87	3564
0.0652	0.87	3333
0.0636	0.87	3320
0.0621	0.87	3300

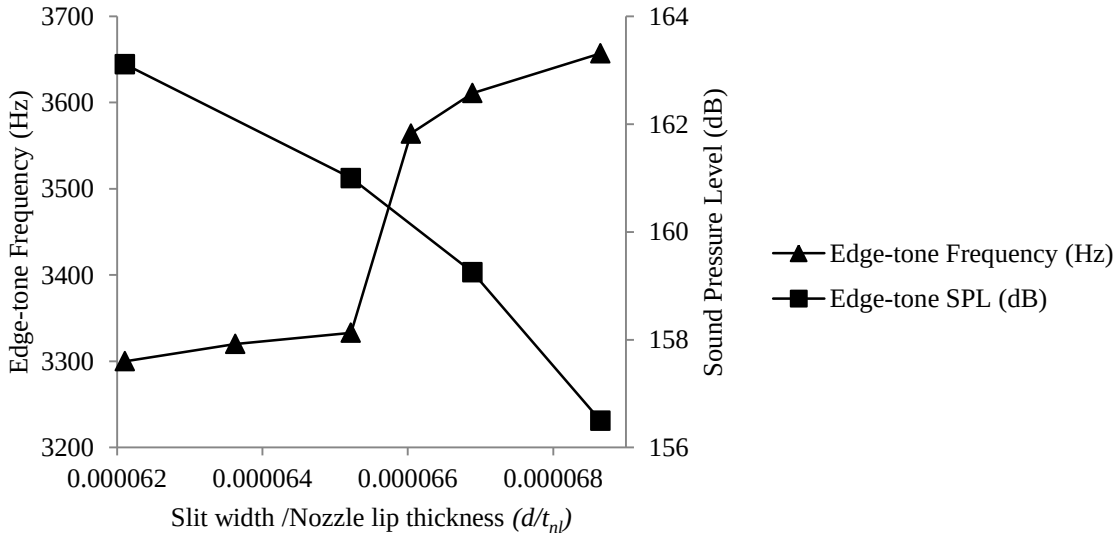

Figure 5-25: Nozzle lip thickness sensitivity study: computed edge-tone frequency and amplitude computations at acoustic field point

Fig. 5-26 shows the normalized axial velocity distribution in radial direction at four different locations for d/t_{nl} of 0.0686. Along with the numerical data obtained in this study, the top hat velocity profile of Eq. (5.4) is shown in this figure. In order to calculate the momentum thickness defined in the top hat velocity profile equation, least-square fitting method is used to determine the axial variation of θ/R and the results of which is shown in Fig. 5-27. The same procedure is conducted for other values of d/t_{nl}, specifically; 0.0652 and 0.0621.

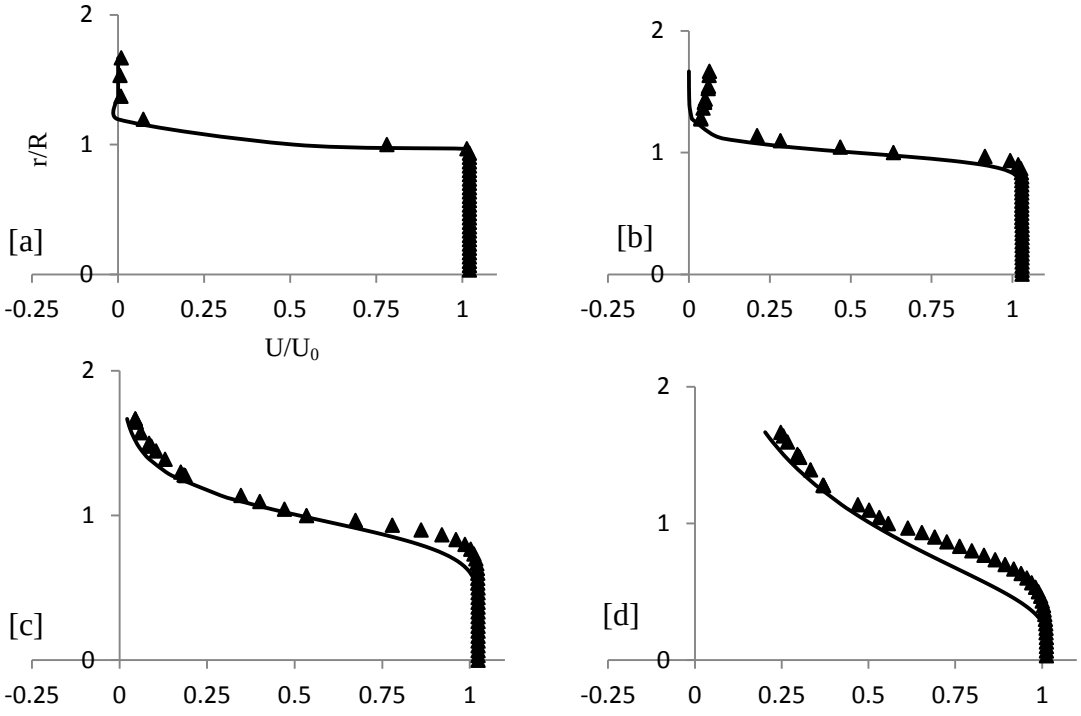

Figure 5-26: Radial velocity distribution at different axial locations for nozzle lip thickness, d/t_{nl} = 0.0686, d/h = 0.1666, and M = 0.87: ♦, numerical data; "----", hyperbolic tangent velocity profile. a) x/d = 0, b) 1, c) 2, and d) 3

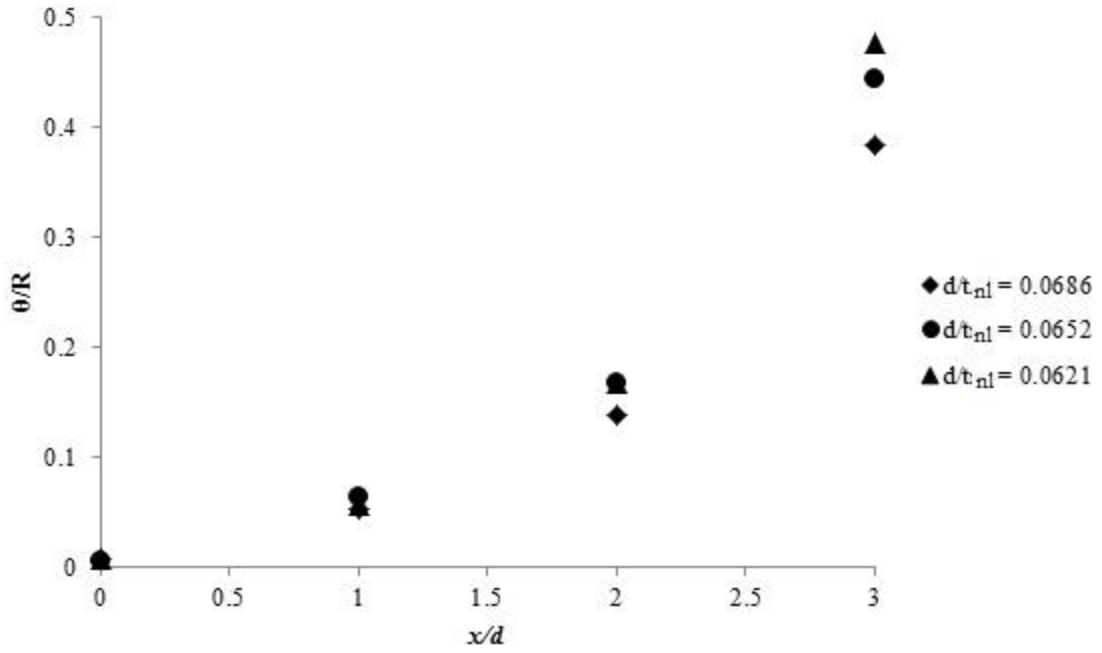

Figure 5-27: Comparison of momentum thickness at several axial locations for different nozzle lip thickness cases at *d/h = 0.1666,* and *M = 0.87.*

It is clearly evident from Fig. 5-27 that the momentum thickness increase as nozzle lip thickness increased. The static pressure data is acquired for three cases of d/t_{nl}, 0.0686, 0.0652, and 0.0621, near the nozzle lip at point *'c'* which is located at 1 *mm* downstream and 0.1 *mm* upward from the jet exit as shown in Fig. 5-6. Pressure spectra are calculated from the static pressure data and it is presented in Fig. 5-28. As shown from this figure, as nozzle lip thickness increase, the amplitude value increased. It proves that thicker nozzle lip generates more intense reflected waves which result from the interaction between incident upstream propagating waves and nozzle lip wall. This interaction results in increase in momentum thickness as the nozzle lip thickness increases. This tendency indicates greater mixing of jet is occurring in the flow-field with large nozzle lip thickness.

When nozzle lip thickness increased, convective speed of jet disturbance decreases along the stand-off distance as shown in Fig. 5-29. It is clearly evident from the figure that the smaller nozzle lip thickness case of d/t_{nl} = 0.0686 has more convective speed of jet disturbance along the stand-off distance than the thicker nozzle lip thickness case of d/t_{nl} = 0.0621. For the cases of $d/t_{nl,}$ specifically; 0.0686 and 0.0621, the downstream propagation times are 0.000152*s* and 0.000185*s*, respectively. It indicates that the downstream propagation time, T_1, increases for thicker nozzle lip thickness case which causes the edge-tone frequency to decrease. The relationships between edge-tone frequency and downstream propagation are described in equations (2.4) and (2.5). Hence, when the nozzle lip thickness increased for a constant stand-off distance and jet exit with constant Mach number, the edge-tone frequency decreased as shown in Fig. 5-25.

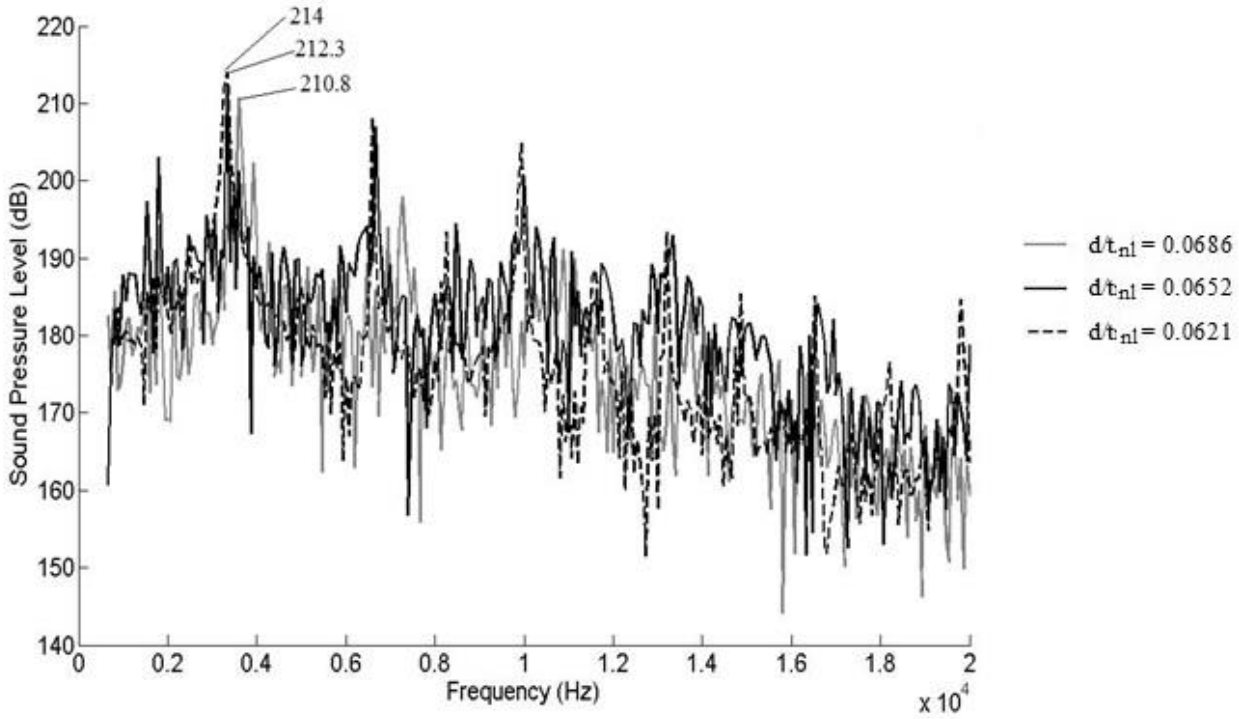

Figure 5-28: SPL spectra for different nozzle lip thickness cases (*d/h*=0.166, *M*=0.87)

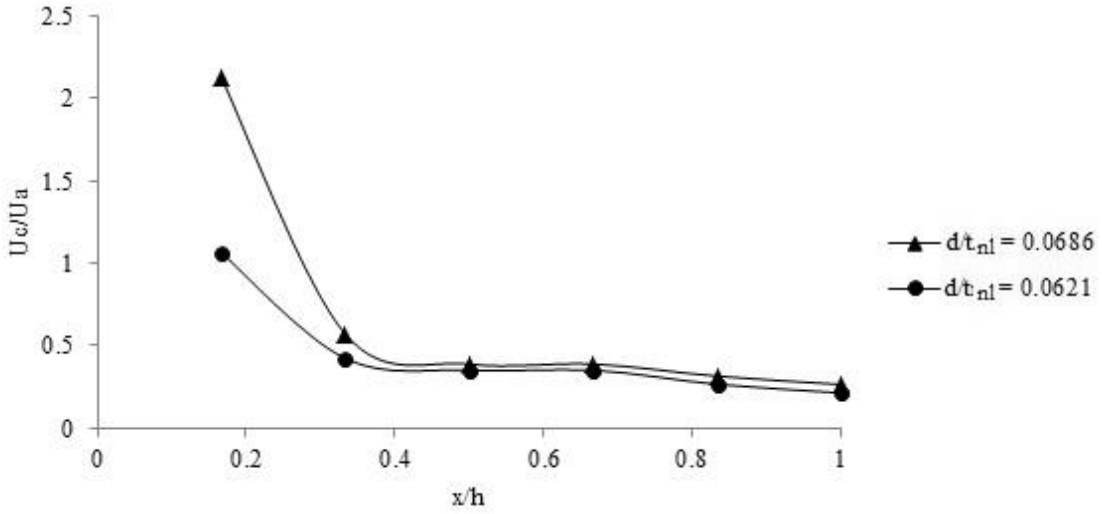

Figure 5-29: Variation of jet disturbance convective speed along the stand-off distance for different nozzle lip thickness cases (*M* = 0.87 and $\dot{m}$ = 1.145)

5.3 Minimum Breadth Study

One of the main features of the edge-tone is the 'minimum breadth,' which is a minimum stand-off distance h_0 required for a first edge-tone to be created. The effect of minimum breadth on edge-tone frequency is studied for two different jets having Mach number of 0.53 and 0.87 at four different stand-off distances as shown in Table 5-5. All the cases have slit width 3 *mm* and wedge angle 20°. The cases studied at both Mach numbers have different minimum breadth regions as shown in Table 5-5 and Fig. 5-30. Since this study focuses on the reason behind the occurrence of minimum breadth, the cases studied at Mach number, 0.87 is explained in detail.

Table 5-5: Cases studied at different stand-off distances for minimum breadth study

d/h	**The computed edge-tone frequency (Hz) (at *M* = 0.53)**	**The computed edge-tone frequency (Hz) (at *M* = 0.87)**
0.500	Nil	Nil
0.333	4519	Nil
0.250	3510	4814
0.166	2441	3333

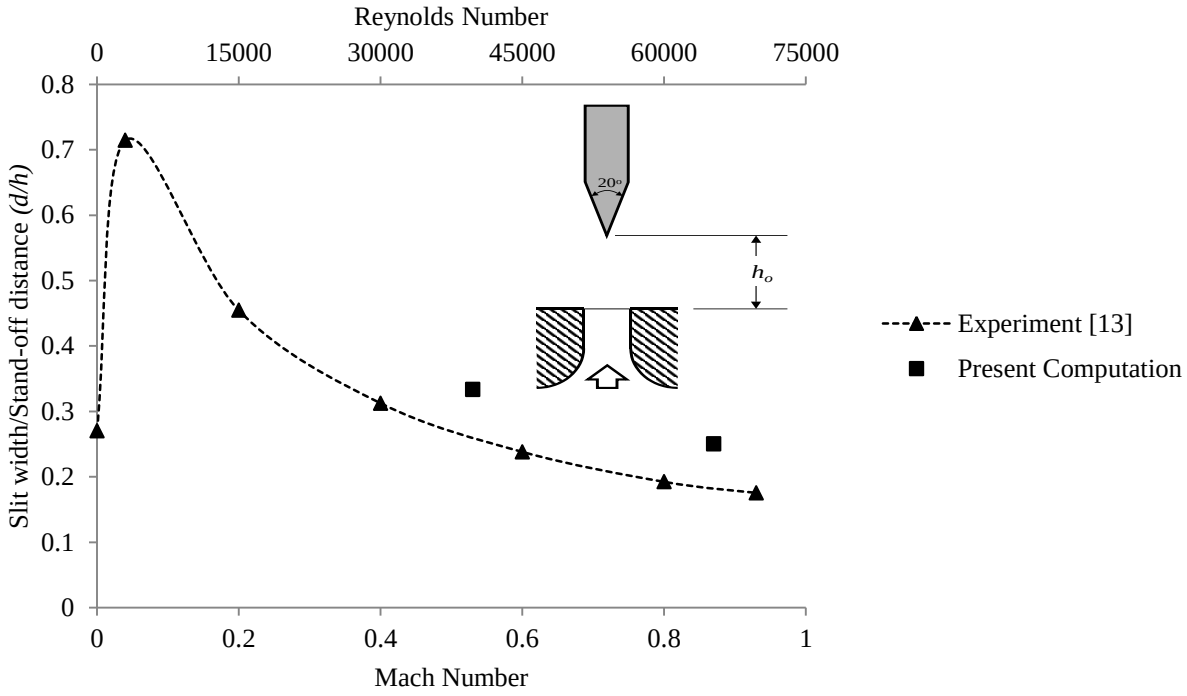

Figure 5-30: Variation of 'minimum breadth' (h_0 – shown in figure) with Mach number and Reynolds number

Minimum stand-off distance *(h_0)* to create minimum breadth is lower in present computation than the experimental data. This might be attributed to the finite aspect ratio of jet employed in the experiments. However, the present computations are 2D, which means infinite aspect ratio and consequently the mass flow rate issuing from the slit is different. Sound Pressure Level (SPL) for the jet with Mach number of 0.87 at three different values of *d/h*, specifically; 0.500, 0.333, and 0.250 is shown in Fig. 5-31. In SPL spectra graph, the peak amplitude at specific frequency denotes the edge-tone frequency. At *d/h* = 0.333, the peak amplitude represents a weak tone because the jet oscillation is not occurred in the flow-field as it is a common phenomenon in edge-tone system. As the stand-off distance decreased, the edge-tone amplitude decreased then disappeared which denotes that there is no edge-tone and SPL value also decreased. Disappearance of edge-

tone amplitude also determines the minimum breadth region. In the present study, the minimum breadth is found out to be $d/h_0 = 0.333$.

In FLUENT, FWH acoustic module provides the static pressure time derivative (*dp/dt* at the wedge surface) of acoustic source surface. For all the four cases of stand-off distances, the time derivative of static pressure of the wedge surface are captured and shown in Fig. 5-32. As the stand-off distance decreases, the time derivative of static pressure of the wedge surface decreases. This value denoted by *dp/dt* which could represent the flow-field oscillations of the jet. For the cases of *d/h*, specifically; 0.500 and 0.333, the surface *dp/dt* shows significant decrease which means that the flow oscillations are reduced. Time average of *dp/dt* is high in case of edge-tone production. This is qualitatively confirmed by observing the vorticity of all four cases as shown in Fig. 5-33. It is evident from Fig. 5-33, that at low value of surface *dp/dt* at edge tip there are no jet oscillations for values of *d/h*, specifically; 0.500 and 0.333. But from Fig. 5-33 (a) and (b), it is proved that there is no vortices interact with the edge tip which leads to the diminishing of upstream wave propagation and of the flow oscillations, and consequently reduced the amplitude of edge-tone frequency. The onset of this condition marks the minimum breadth. For other values of *d/h*, 0.250 and 0.1666, shown in Fig. 5-33 (c) and (d), respectively, it is evident that vortices are interacted with the edge tip and consequently the amplitude of edge-tone frequency increases and it becomes very clear in the spectra.

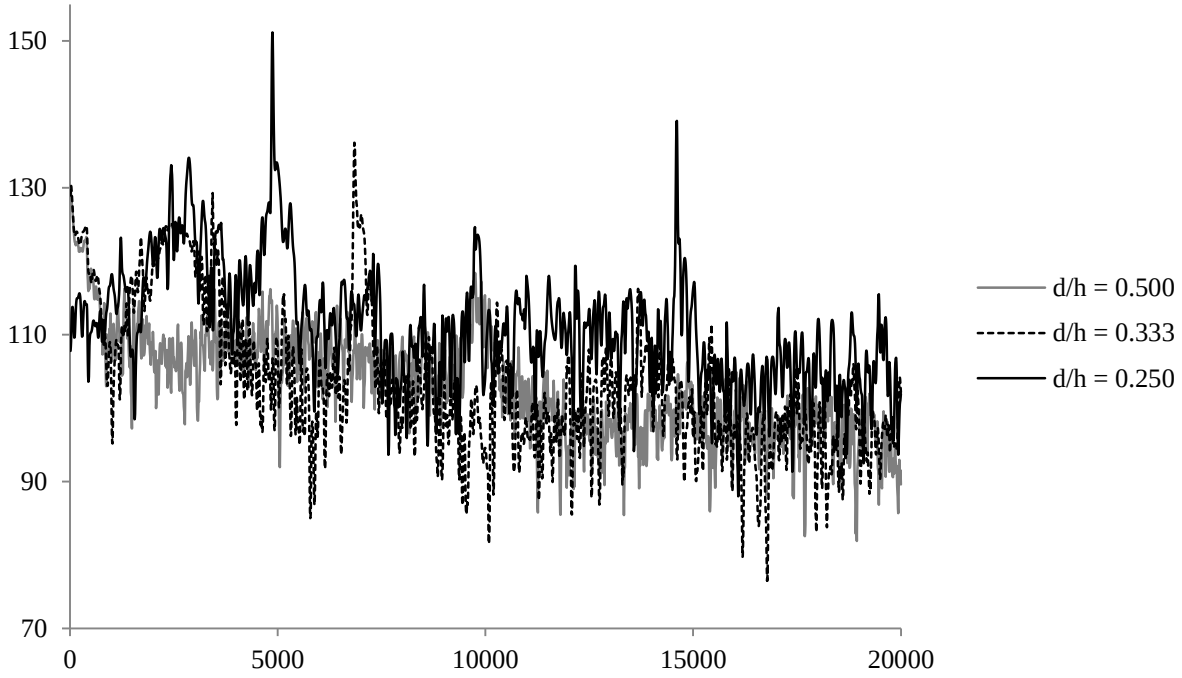

Figure 5-31: Sound Pressure Level for *M* = 0.87 at different *d/h* (0.500, 0.333, 0.250) (3 point average)

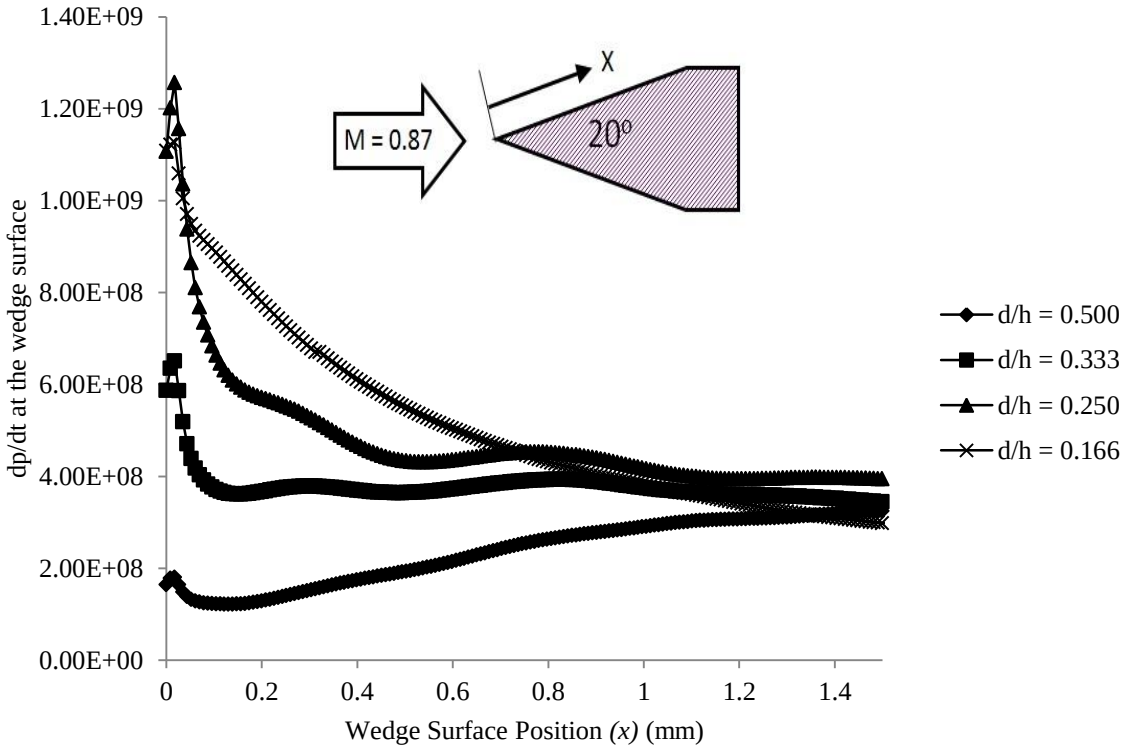

Figure 5-32: The time derivative of the static pressure of flow-field on wedge surface position, *x* (shown in figure) for *M* = 0.87

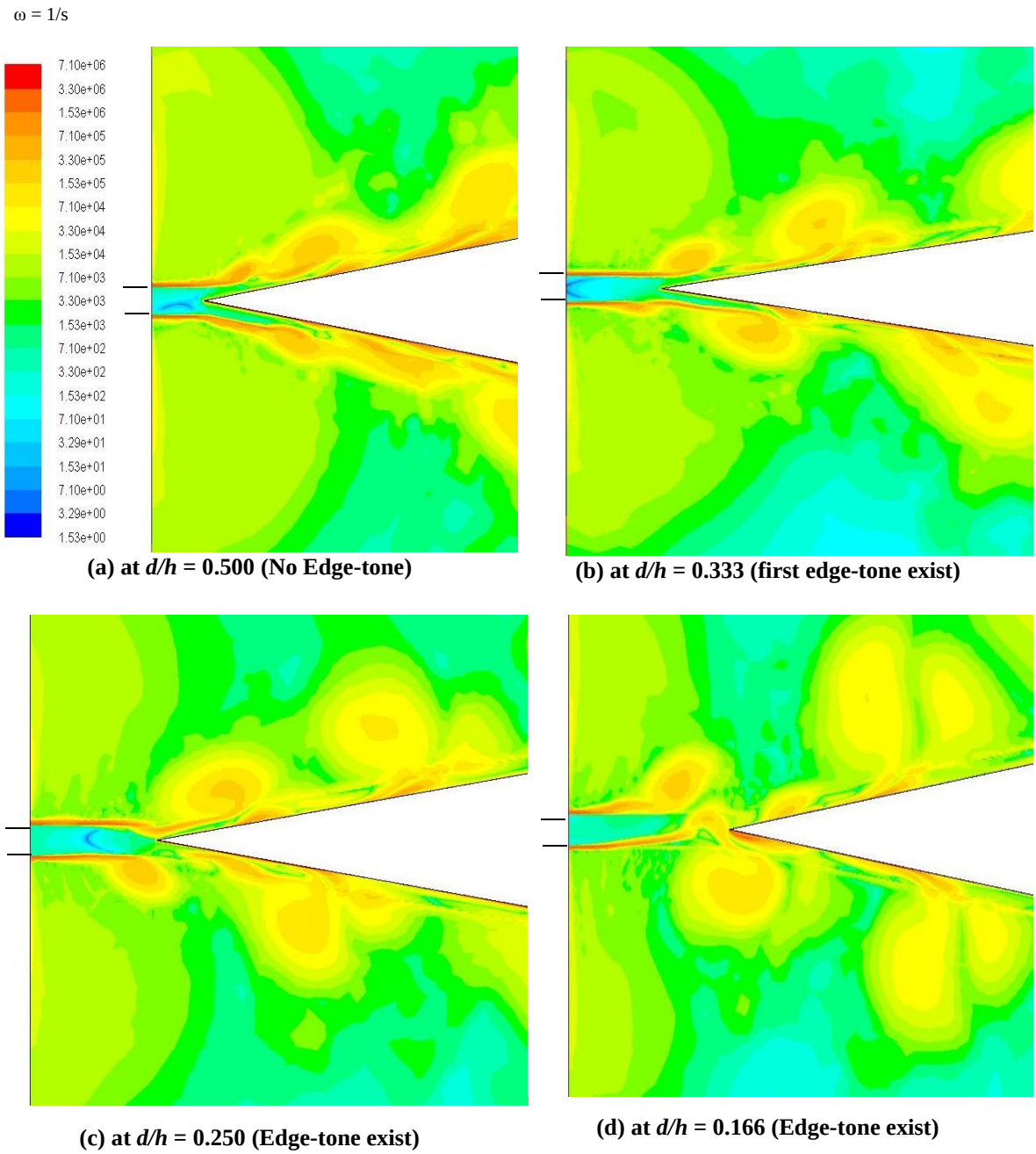

(a) at *d/h* = 0.500 (No Edge-tone)

(b) at *d/h* = 0.333 (first edge-tone exist)

(c) at *d/h* = 0.250 (Edge-tone exist)

(d) at *d/h* = 0.166 (Edge-tone exist)

Figure 5-33: Vorticity contours for *M* = 0.87 at different stand-off distances

5.4 Feedback Loop Path Study

Many researchers have investigated whether the upstream propagation path is inside the jet or outside the jet. Some mentioned upstream propagation happens inside the jet [7] while other researchers like Kwon [8] and Karamcheti *et.al* [11] mentioned it happens outside the jet. In this section, clarification of upstream propagation path is addressed. To

know how the upstream propagation functions, two methods have been carried out. In the first method, secondary coaxial flow, U_s (half of the speed of main jet, U_j) set-up is created in the same direction along with the main jet exit flow as shown in Fig. 5-34. It is based on the experimental method of Sheplak *et.al* [49]. If the upstream propagation is outside from the jet stream, then the secondary flow will disturb the propagation that will result in the reduction of edge-tone frequency and amplitude. In the other method, two small plates are inserted at the middle of the stand-off distance without disturbing the downstream propagation as shown in Fig. 5-35. It is based on the experimental method of Karamcheti *et.al* [11]. If the upstream propagation lies outside of the jet stream, then the plates will disturb the propagation that will eventually decrease the edge-tone frequency and amplitude as indicated by Eq. (2.4).

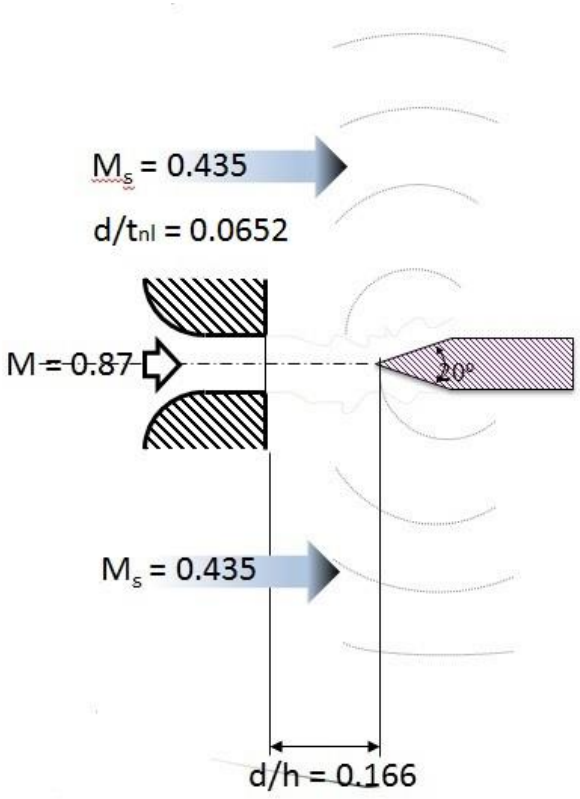

Figure 5-34: Schematic of secondary flow method at *d/h* = 0.1666, Mach number of the main jet = 0.87 and Mach number of secondary flow = 0.435

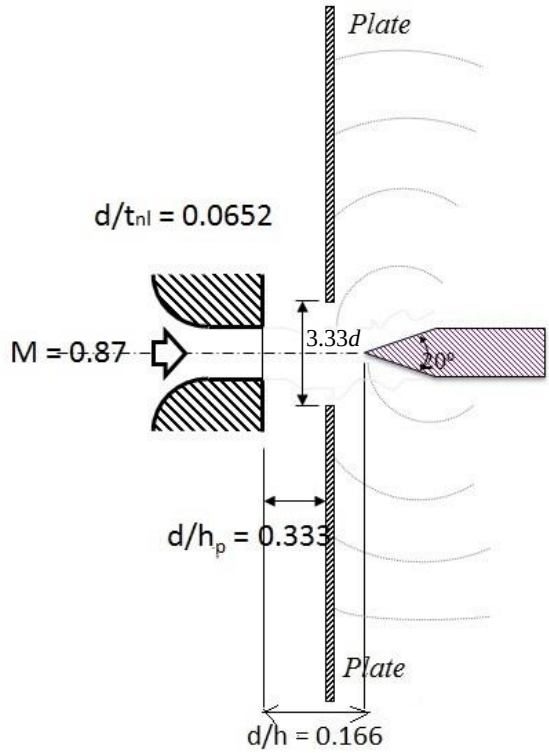

Figure 5-35: Schematic of inserted plates method at *d/h* = 0.1666, d/l_t = 0.0652, two plates of length 0.495 *m* is placed at *d/h* = 0.333 and Mach number of the main jet = 0.87

In both of the above cases the edge-tone frequency decreased significantly as shown in Fig. 5-36, which illustrates that the acoustic feedback path lies outside of the jet stream. Both methods are considered to confirm the reduction in edge-tone frequency. The flow-field results from both the methods are shown in Fig. 5-37 and Fig. 5-38. When comparing the flow-field results with that of baseline jet in Fig. 5-2, in the secondary coaxial flow oscillations (shown in Fig. 5-37) it is evident that the secondary coaxial flow shields the main jet from the near field acoustic disturbances similar to to the method of Sheplak *et al.* [49]. While in the flow-field results of other case in which the plates are inserted normal to the jet centreline (shown in Fig. 5-38), the formation of large scale structures is weaken in the jet flow due to disrupting the upstream propagating acoustic waves that interrupt the feedback loop similar to the method of Karamcheti *et al.* [11] and

Elavarasan *et al.* [50] . Edge-tone frequencies are calculated from the above two methods and presented in Table 5-6. The cases have *d/h* = 0.1666, 20° angle of wedge and jet Mach number of 0.87. Edge-tone frequencies decreased in the two methods compared to the validated case.

Table 5-6: Cases studied for different methods for feedback loop path study

Model	The computed edge-tone frequency (Hz)	Amplitude of the computed edge-tone frequency (dB)	% change in the edge-tone amplitude with the baseline case (Hz)
Baseline case	3333	160.9	0
Baseline case with secondary flow	2539	147.9	8.07
Baseline case with inserted plates	1424	150.2	6.65

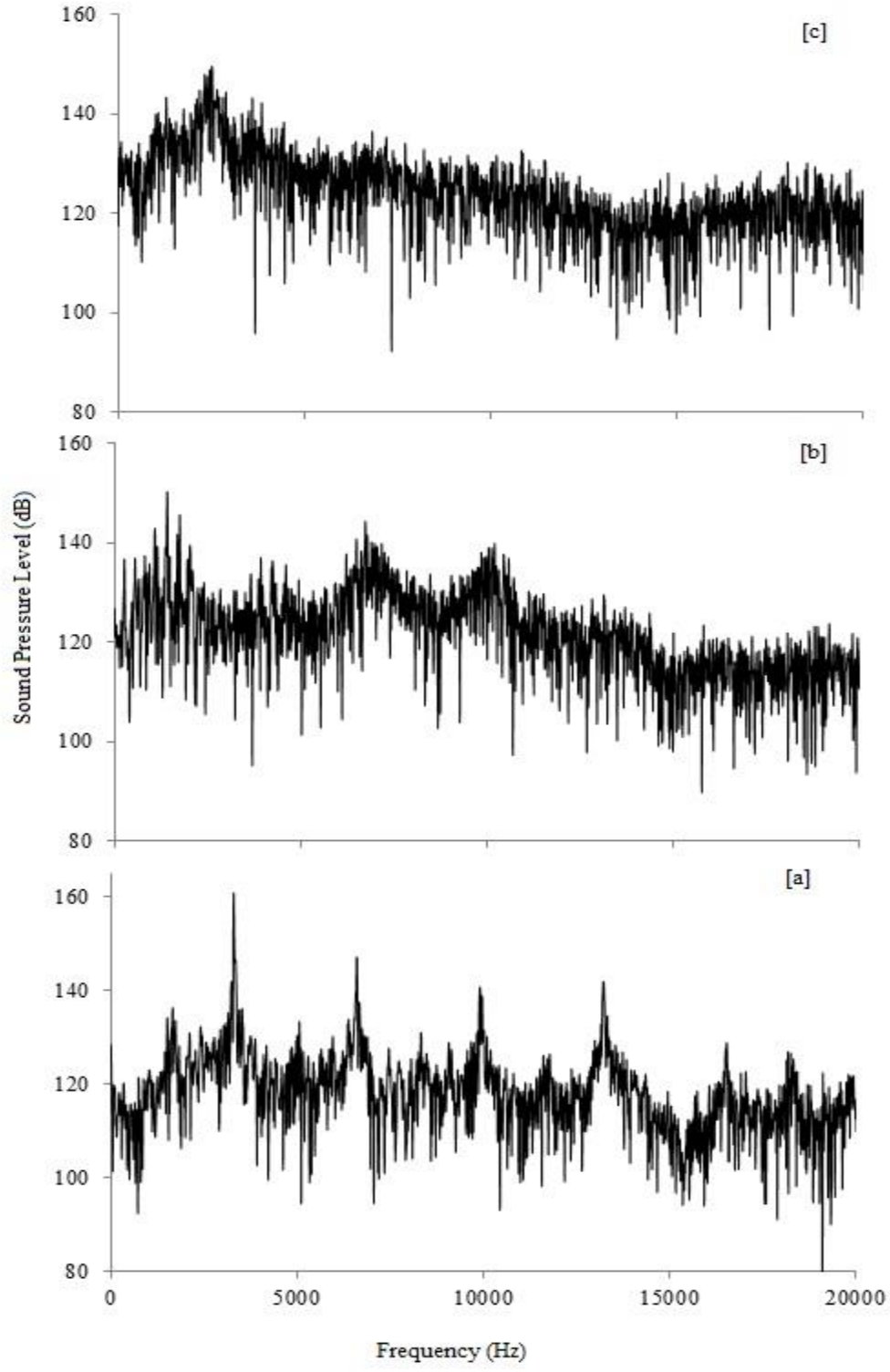

Figure 5-36: SPL spectra for different cases at *d/h* = 0.1666 and *M* = 0.87 and wedge angle 20°; [a]baseline case; [b]baseline case with plates inserted method; and [c]baseline case with secondary flow method

p in *pa*

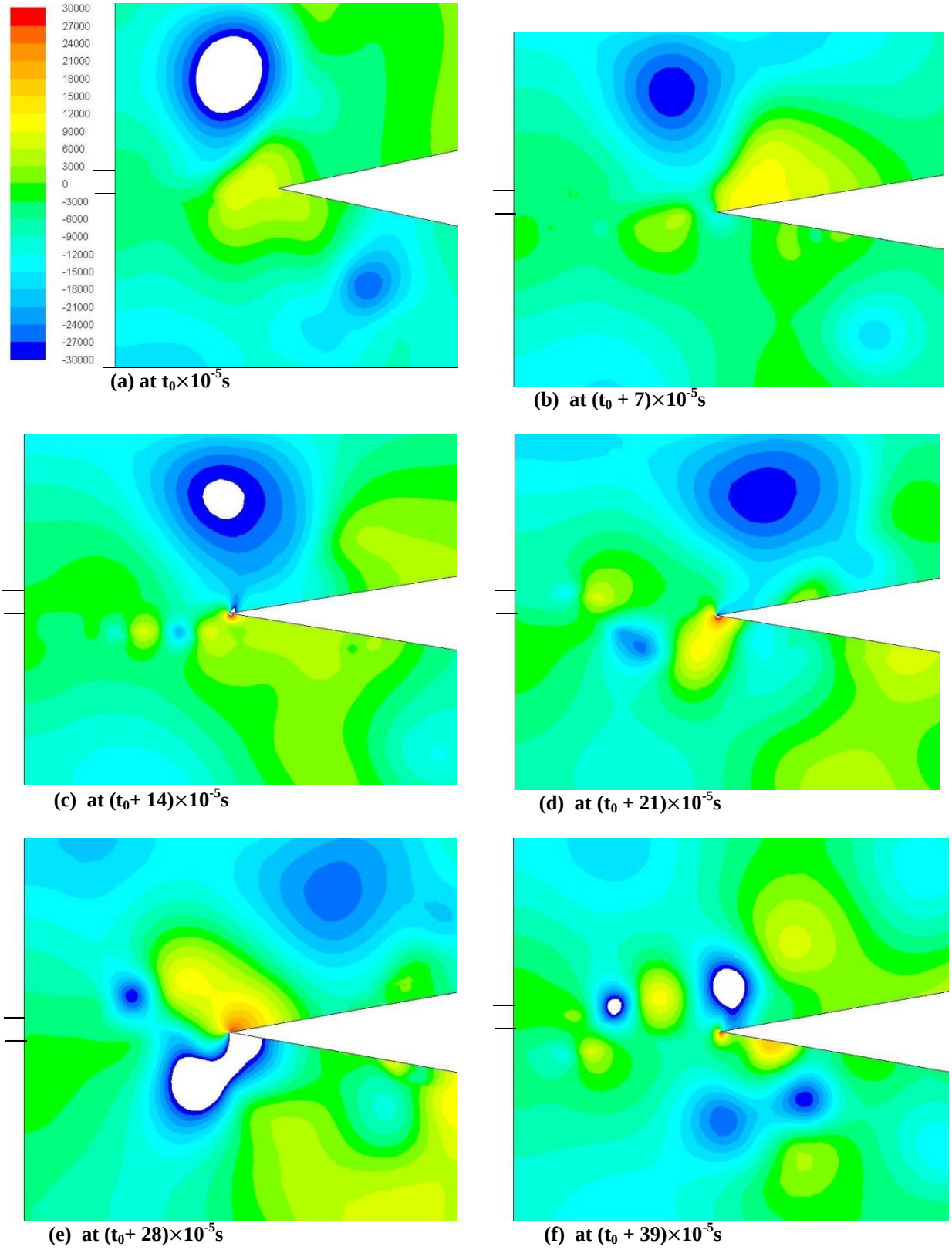

(a) at $t_0 \times 10^{-5}$s

(b) at $(t_0 + 7) \times 10^{-5}$s

(c) at $(t_0 + 14) \times 10^{-5}$s

(d) at $(t_0 + 21) \times 10^{-5}$s

(e) at $(t_0 + 28) \times 10^{-5}$s

(f) at $(t_0 + 39) \times 10^{-5}$s

Figure 5-37: Static pressure contours of secondary flow model at *d/h* = 0.1666, Mach number of the main jet = 0.87 and Mach number of secondary flow = 0.435

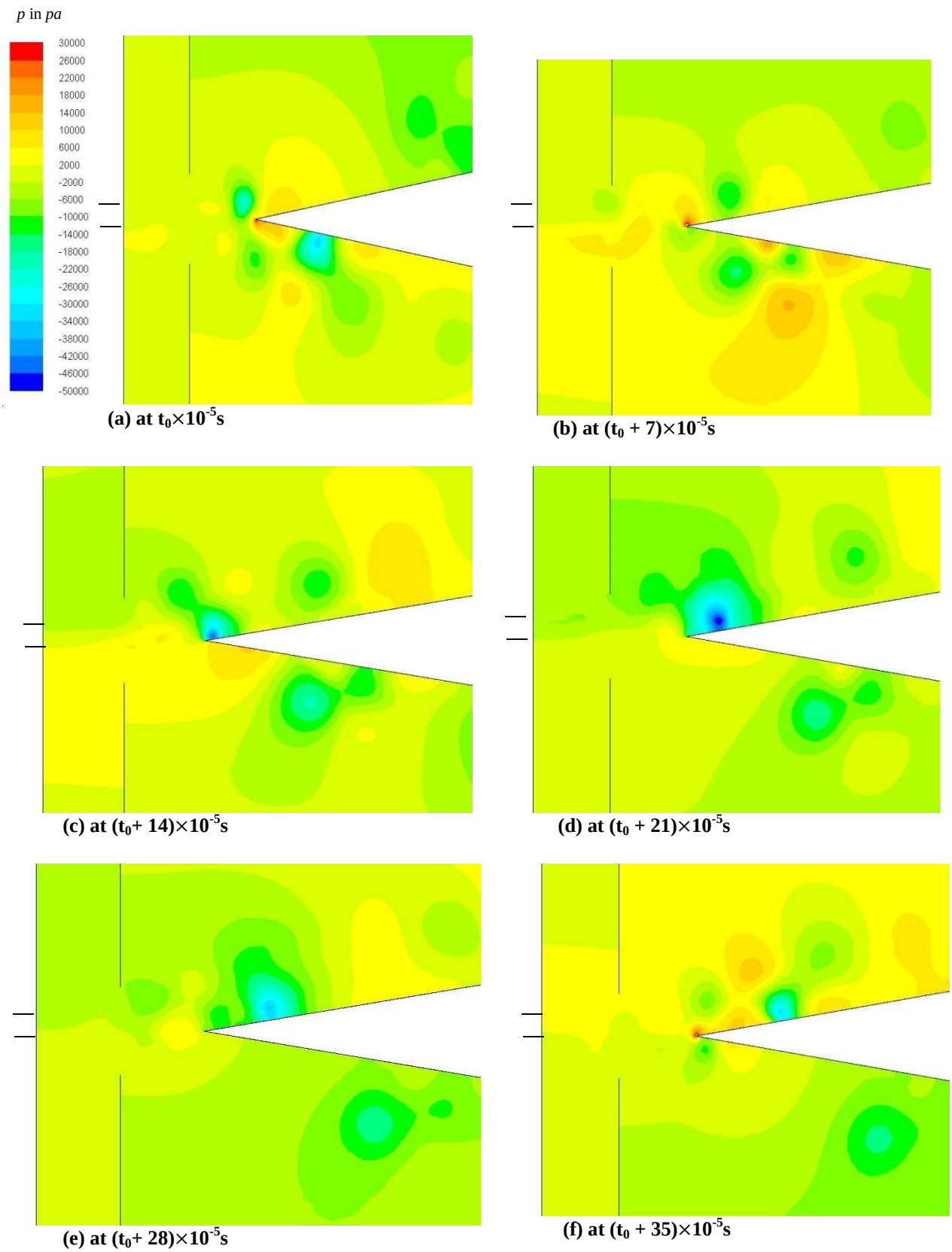

(a) at $t_0 \times 10^{-5}$s

(b) at $(t_0 + 7) \times 10^{-5}$s

(c) at $(t_0 + 14) \times 10^{-5}$s

(d) at $(t_0 + 21) \times 10^{-5}$s

(e) at $(t_0 + 28) \times 10^{-5}$s

(f) at $(t_0 + 35) \times 10^{-5}$s

Figure 5-38: Static pressure contours for plates inserted model at *d/h* = 0.1666, Mach number of the main jet = 0.87

5.5 Edge-tone Suppression

The aim of the present investigation is to propose a technique to suppress the edge-tone amplitude to avoid the sonic fatigue failure of any the nearby structure [51]. Since the edge-tone is a loud noise with high amplitude, it could lead to structural damage. Edge-tone is suppressed by Karamcheti *et al.* [11] who claimed that the edge-tone can be reduced and stopped by placing single or double plates normal to the centerline of the undisturbed jet in the outside flow region. They even proposed locations required to stop edge-tone. The plates restrict the upstream propagating acoustic waves that causes weakening of feedback loop which results in edge-tone suppression. Edge-tone can be suppressed by any active or passive control methods which make the feedback loop incomplete. To reduce supersonic impingement tones, many passive control methods for example Karamcheti *et al.*[11] placed two plates normal to the centerline of the jet, Glass [52] and Poldervaart *et al.* [53] used similar passive control techniques, Elavarasan *et al.* [50] introduced a control plate near the nozzle exit and active control methods for example Sheplak *et al.* [49] used high speed co-flow to shield the main jet from the near-field acoustic disturbances, Shih *et al.* [54] used counter flow near the nozzle exit to suppress screech tones in non-ideally expanded jets, Alvi *et al.* [55] used a circular array of supersonic microjets around the periphery of the main jet at the nozzle exit to modify the nozzle shear layer, Rayan *et al.* [56] introduced a microjet inside the jet plume to modify the shear layer. These methods have been studied over the years to stop the feedback loop.

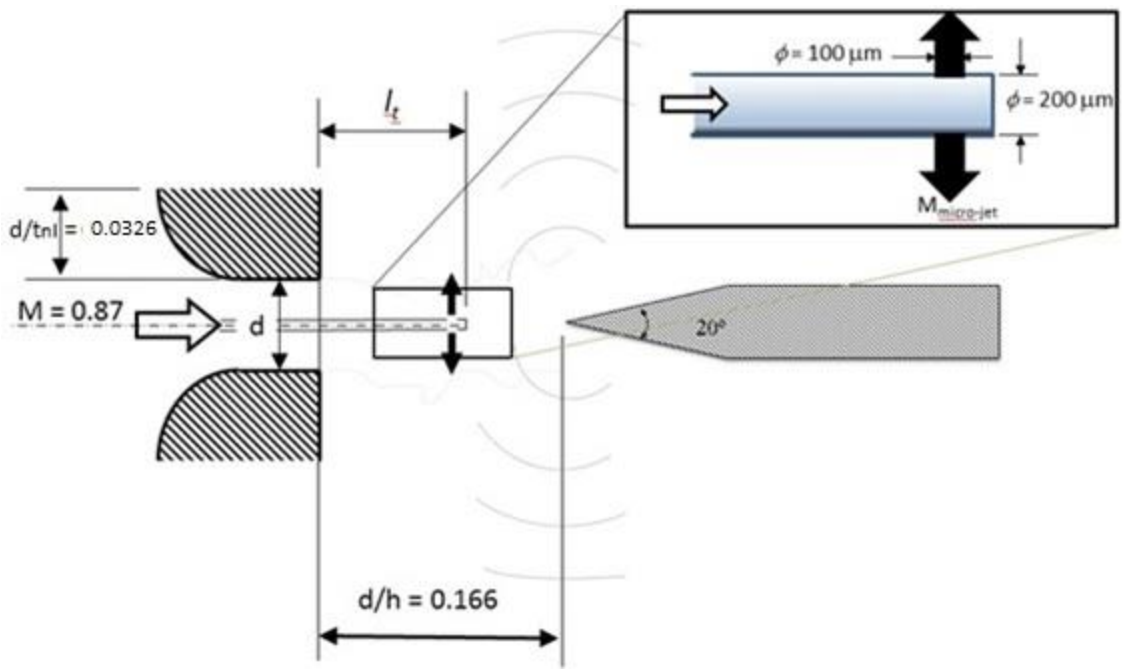

Figure 5-39: Schematic of microjet injection from a tube of length l_t

The method in Ryan *et al.* [56] introduces microjet inside the jet plume to modify the shear layer thereby reducing the jet noise effectively. Due to their miniature size and mass flow rate, microjets are better option to inject anywhere in the fluid in form of steady or pulsed jets to alter the shear layer. In this present study, two microjets with diameter of 100 micrometer are introduced inside the high speed edge-tone test case as shown in Fig. 5-39. Microjets are injected at different Mach numbers, specifically; 0, 0.87, 1, and 1.42 at d/l_t = 0.300, d/h = 0.1666, the central insertion tube diameter of 200 micrometer and the main jet at exit Mach number of 0.87. For supersonic microjet, Mach number is equal to 1.42 and it is achieved by adjusting the microjet exit pressure to make the microjet injection chocked at the exit. Consequently the exit speed is a sonic speed and it can expands outside the tube to reach as maximum as M = 1.42. Central insertion tube diameter is selected to provide the required mass flow rate of gas for microjet injections at its end and it is presented in Table 5-7. Velocity contours and comparison of SPL is shown in Fig. 5-40 and Fig. 5-41, respectively.

Table 5-7: Mass flow rate of microjets for different speeds

Microjet Mach Number	Mass Flow Rate (kg/s)
0	0
0.87	0.03814
1	0.04475
1.42	0.069

It is observed from the velocity contours from Fig. 5-40 (c), (d) and (e), that the jet shear layer is forced to shift or bulge outward in the vicinity of the microjet injection. It is clear from Fig. 5-41 that the cases with different speeds of microjet injection suppressed the edge-tone amplitude due to their interaction with the main jet shear layer. The results proved that microjet injection inside the jet plume has almost the same effect on reducing edge-tone amplitude as the 'no microjet injection' case, in which the edge-tone amplitude is suppressed. No microjet injection case suggested that central insertion tube plays a vital role in reducing the edge-tone amplitude. To study the effect of the tube length, different central insertion tube lengths, d/l_t, specifically; 0.500, 0.375 and 0.300 is considered for simulations with main jet at M = 0.87, and d/h = 0.1666. Comparison of SPL is shown in Fig. 5-42, which proves that central insertion tube reduces the amplitude of edge-tone. The suppression mechanism can be explained as follows: When the central insertion tube 'without microjet injection' is introduced inside the jet plume, it disturbs the jet oscillations in the flow-field. In the edge-tone feedback loop, the jet oscillation completes one cycle at a time that is equivalent to the reciprocal of edge-tone frequency. Since the central insertion tube disturbs the jet oscillation, it weakens the feedback loop which results in reduction of edge-tone amplitude. A schematic of central insertion tube mechanism is presented in Fig. 5-43.

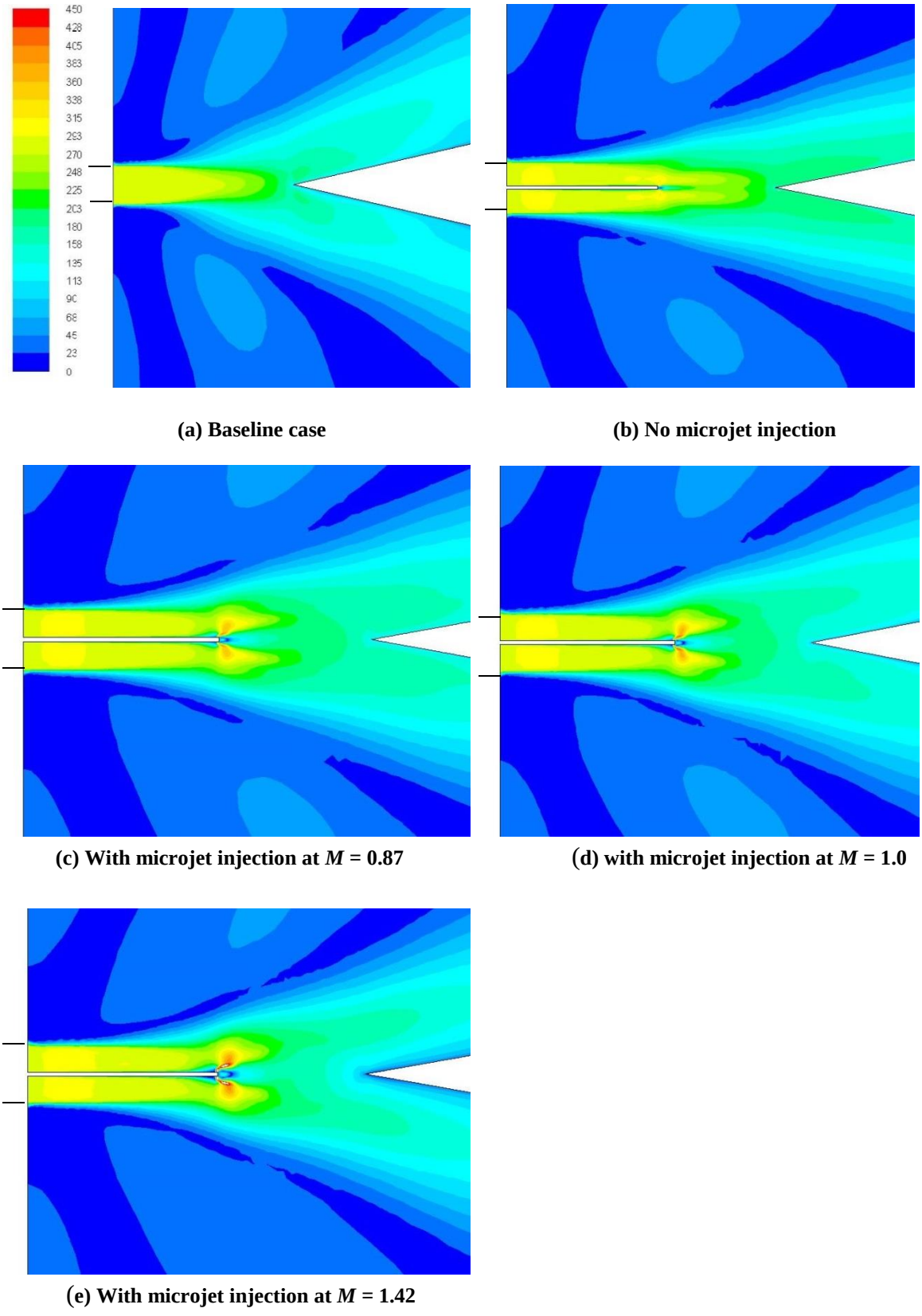

(a) Baseline case

(b) No microjet injection

(c) With microjet injection at M = 0.87

(d) with microjet injection at M = 1.0

(e) With microjet injection at M = 1.42

Figure 5-40: Velocity contours for baseline case and main jet at M = 0.87, d/h = 0.166 and d/l_t = 0.300 with different microjet speeds

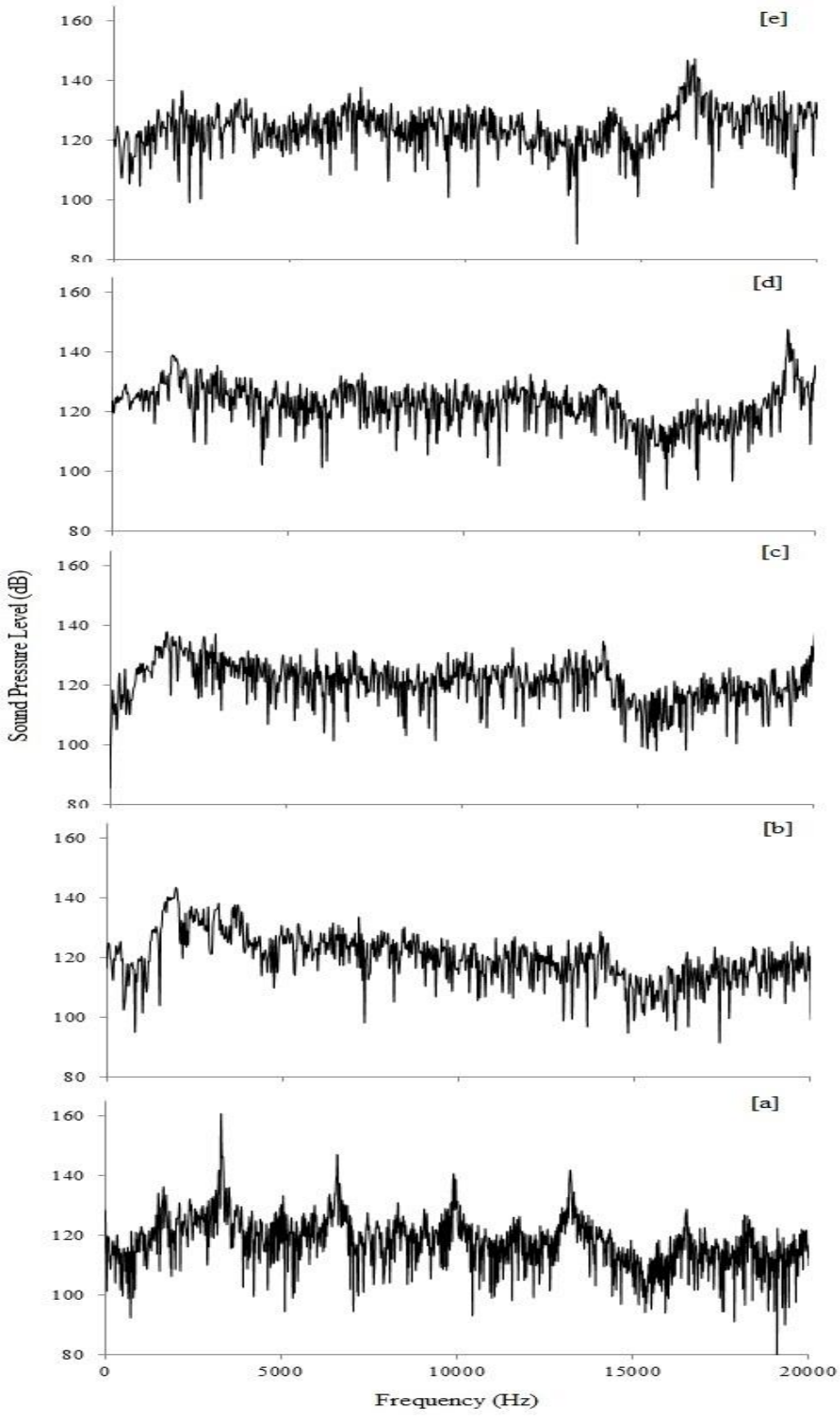

Figure 5-41: Comparison of SPL for main jet at M = 0.87, d/h = 0.166 and d/l_t = 0.300 with different microjet speeds, specifically; [a] Baseline Jet, [b] No microjet injection, [c] Microjet at M = 0.87, [d] M = 1 and [e] M = 1.42.

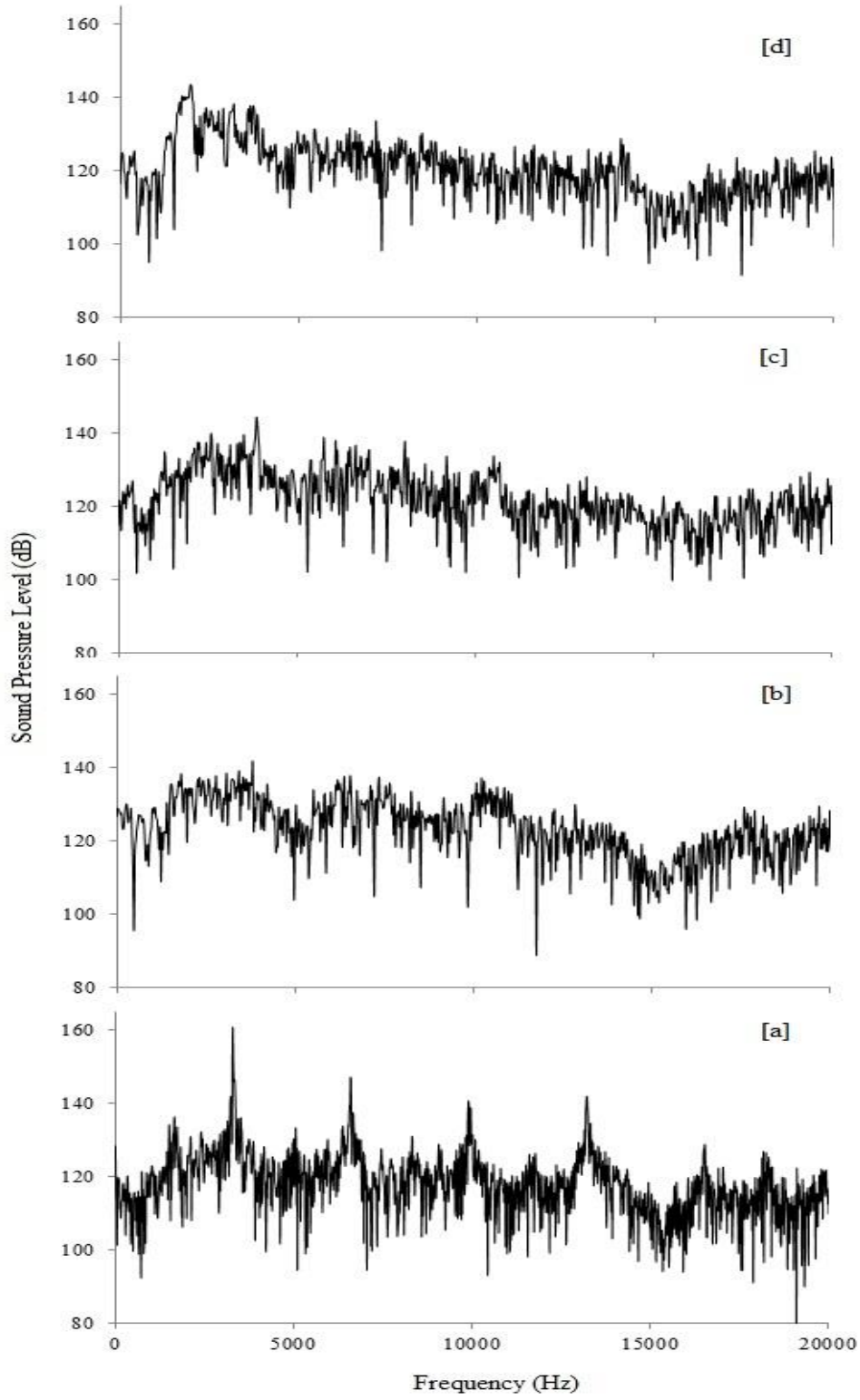

Figure 5-42: Comparison of SPL for main jet at M = 0.87, d/h = 0.1666, and different lengths of central insertion tube without microjet injection, d/l_t, specifically; [a] Baseline jet (l_t = 0 *mm*), [b] 0.500, [c] 0.375, and [d] 0.300

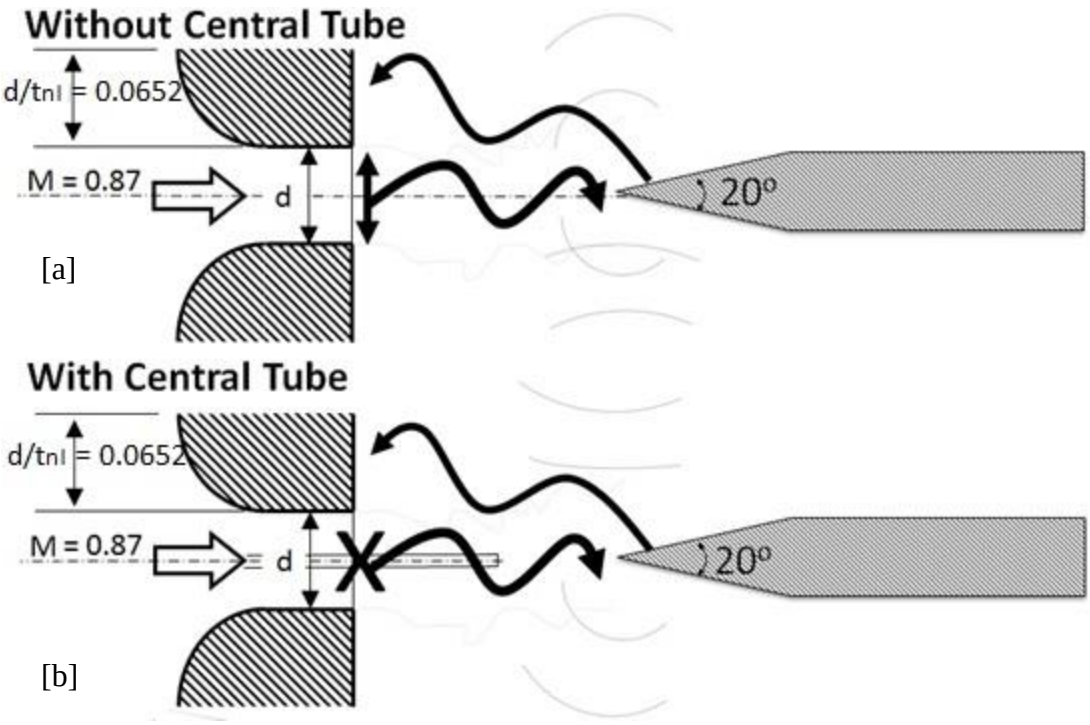

Figure 5-43: (a) Schematic of baseline jet flow oscillation (b) Schematic of central insertion tube effect 'without microjet injection' on flow oscillation

The phase variation along the centerline for the high speed baseline jet edge-tone case is studied in detail and it is presented in Fig. 5-21. It increased along the stand-off distance from nozzle exit to the wedge tip. When the central insertion tube 'without microjet injection' is inserted into the jet plume, it cuts the shear layer interaction between both the edges of nozzle lip throughout its length *(d/l_t).* The separated shear layer is forced to flow and interact in the remaining stand-off distance *(i.e. $d/h - d/l_t$)*, thereby reducing the flow oscillations as seen in Fig. 5-43 [b]. It also affects the phase variation along the stand-off distance. It functions similar to the splitter plate used to control the vortex shedding in cylinder-plate cofiguration models [57, 58]. Central insertion tube limits the jet oscillations in the flow-field of edge-tone system that results in the suppression of edge-tone amplitude as shown in Fig. 5-43 and above all no microjet injection is needed.

This control approach is very successful in disrupting the flow oscillations which led to dramatic reductions in the edge-tone amplitude (17 dB) when a tube of length, d/l_t = 0.375 is inserted into the jet plume having Mach number of 0.87. To understand the relation between the stand-off distance and central insertion tube length, different lengths of central insertion tubes are placed inside the jet plume for two different stand-off distances, *d/h*, specifically; 0.1428 and 0.0869. A summary of simulated cases are shown in Fig. 5-44 along with reduction percentage of SPL compared to the baseline case. As the length of central insertion tube decreases, the edge-tone amplitude increases and percentage reduction decreases.

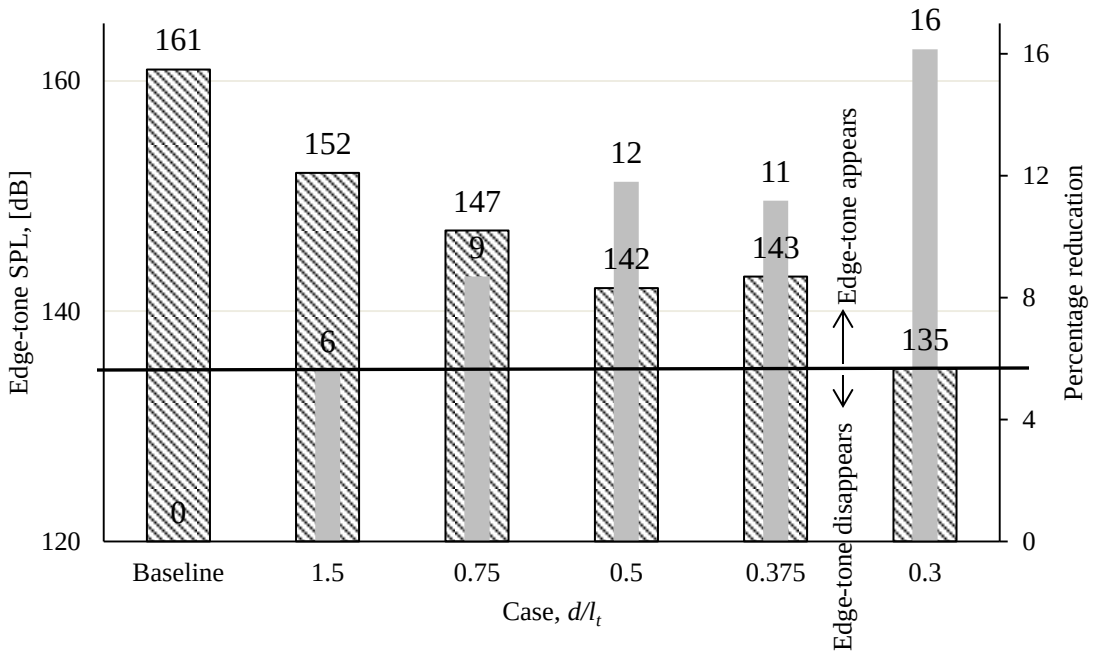

Figure 5-44: Edge-tone suppression cases: SPL reduction

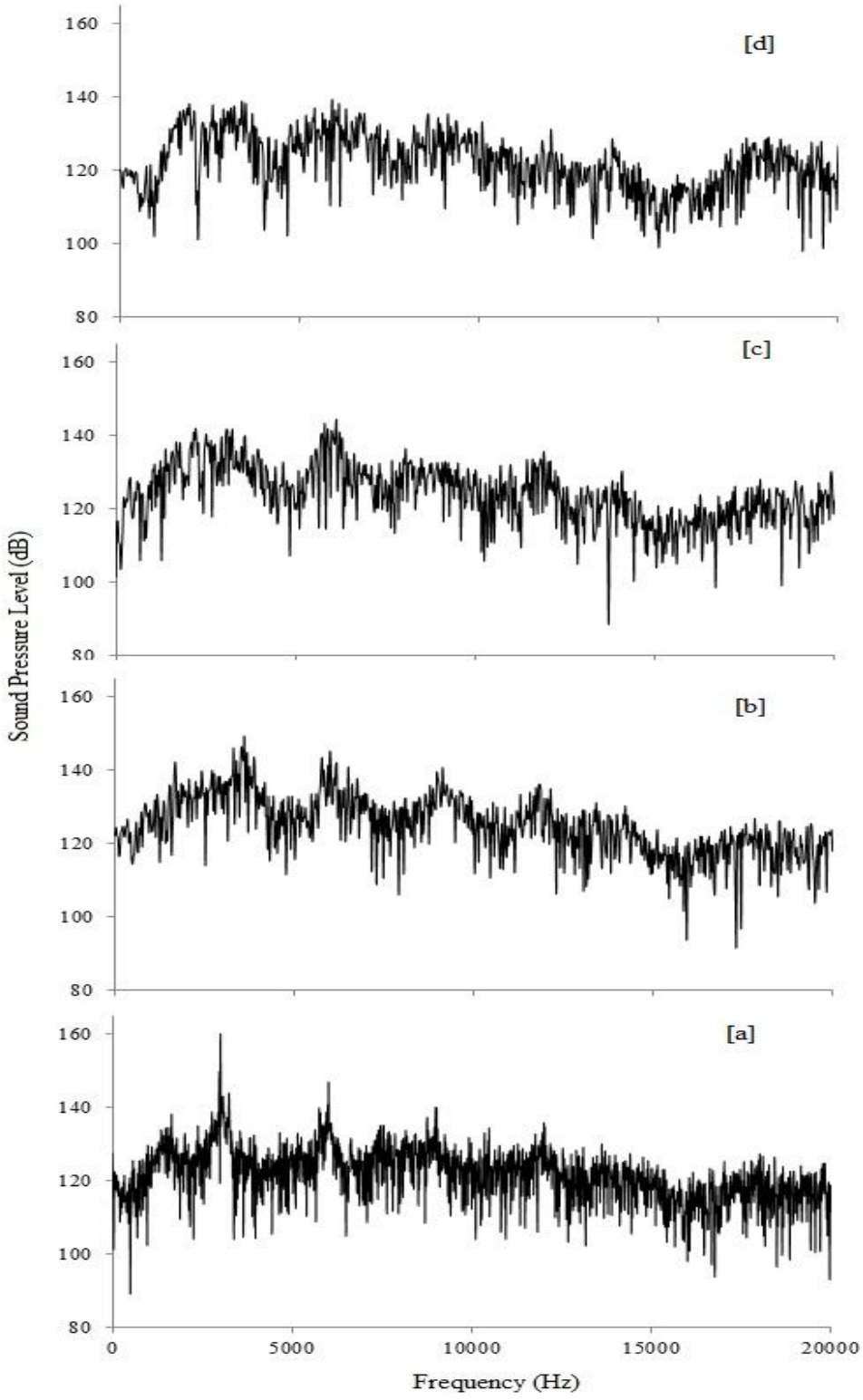

Figure 5-45: Comparison of SPL for main jet at M = 0.87, d/h = 0.1428, and different lengths of central insertion tube without microjet injection, d/l_t, specifically; [a] Baseline jet (l_t = 0 *mm*), [b] 0.750, [c] 0.500, and [d] 0.375

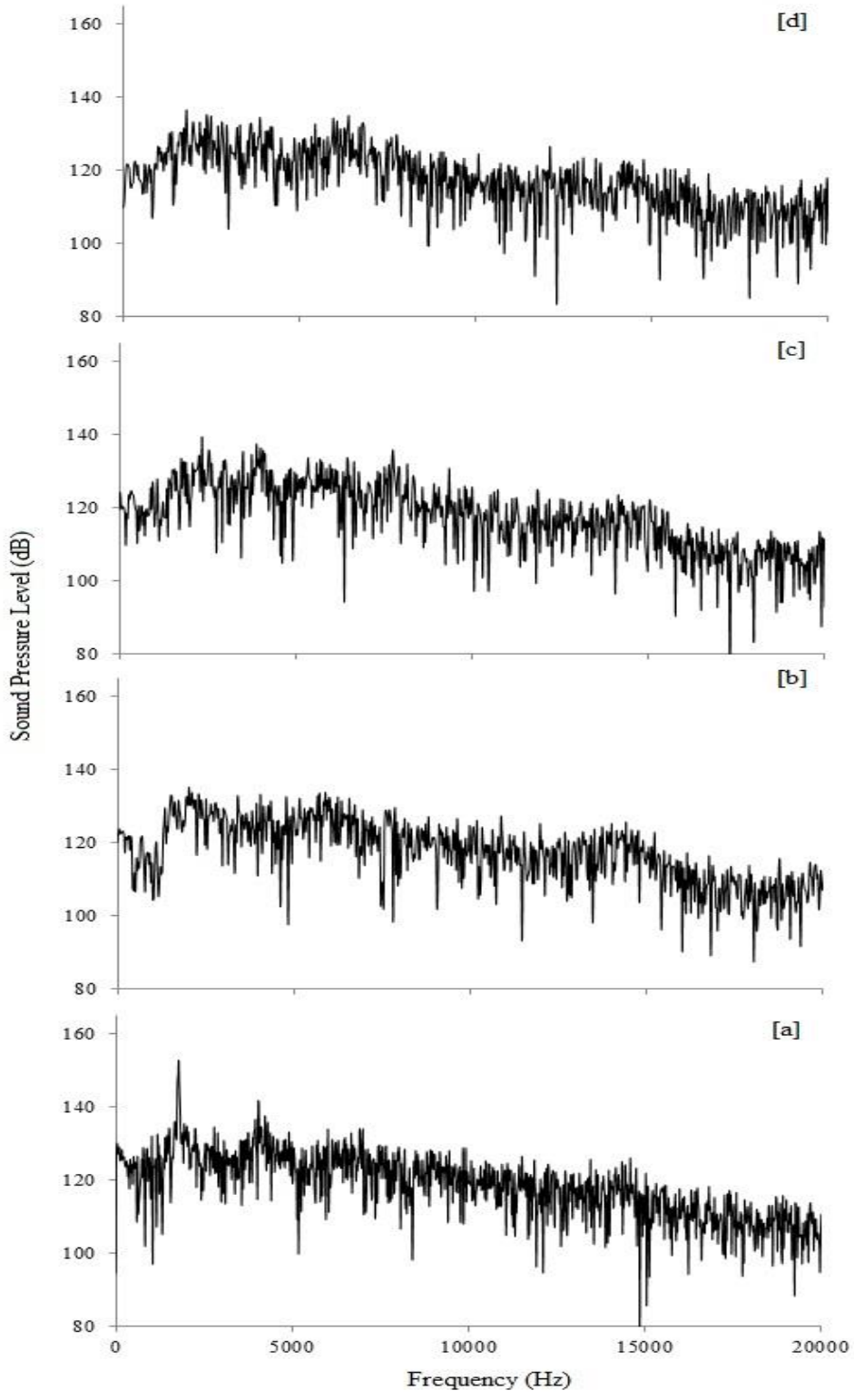

Figure 5-46: Comparison of SPL for main jet at M = 0.87, d/h = 0.0869, and different lengths of central insertion tube without microjet injection, d/l_t, specifically; [a] Baseline jet (l_t = 0 *mm*), [b] 0.375, [c] 0.300, and [d] 0.250

Fig. 5-45 shows the SPL for the case of wedge located at *d/h* of 0.1428, with baseline jet, and with central insertion tubes of different lengths, d/l_t, specifically; 0.750, 0.500, and 0.375. From thesis results the edge-tone amplitude is suppressed when the central insertion tube of length, d/l_t = 0.500, inserted into the jet plume, which is 28.57 percent of the stand-off distance. From Fig. 5-42 also it is evident that when the central insertion tube of length, d/l_t = 0.500, is inserted into the jet plume the edge-tone is suppressed which is 33.33 percent of the stand-off distance. Fig. 5-46 shows the SPL for the case of wedge located at *d/h* of 0.0869, with baseline jet, and with central insertion tubes of different lengths, d/l_t, specifically; 0.375, 0.300 and 0.250. From thesis results, when the central insertion tube of length, d/l_t = 0.300, is inserted into the jet plume the edge-tone is suppressed which is 28.9 percent of the stand-off distance. So as the central insertion tube length increases the edge-tone amplitude decreases by limiting the flow oscillation. When the central insertion tube length reaches around 30 percent of the stand-off distance, the edge-tone is suppressed dramatically.

CHAPTER 6

CONCLUSIONS AND FUTURE RECOMMENDATIONS

6.1 Conclusions

In the present study, the edge-tone generated due to high speed jet-edge system is computationally studied. Two dimensional, compressible, unsteady Navier-Stokes commercial code, Fluent, is employed. The results of both laminar and turbulent flows are reported. Parametric studies are conducted to study the effects of compressibility, edge shape, shear layer thickness and nozzle lip thickness on both the edge-tone frequency, amplitude and the associated flow-field. The flow-fields associated with stand-off distance around the minimum breadth are characterized. The numerical computations are also conducted to reveal the feedback loop path whether it is inside or outside the jet. Finally a technique to suppress the edge-tone is proposed and assessed. Below a summary of the main conclusion is presented.

Compressibility effect or jet Mach number study on edge-tone showed that the edge-tone frequency increases as the Mach number increases. Because, the increase of Mach number results in reducing the downstream propagation time (T_1) and the total time of upstream and downstream propagation (T_1+T_2) which leads to the increase of edge-tone frequency.

Wedge angle effect study on edge-tone confirmed that two stages occurred with the increase in stand-off distance the frequency decrease for the 20° and 60° wedge angles in a similar way. In the special case of wedge angle 180° (i.e., impingement on a flat plate), the first stage is the same as the previous two cases. However, the second stage is occurred at lower frequencies range. The reason behind this change in behavior for the second stage in case of jet impingement is not clear.

Velocity profile effect study on edge-tone confirmed that phase lag value is -0.1 for high speed jets. The edge-tone frequency decreased gradually as shear layer thickness increased. Because greater momentum thickness indicates greater mixing of jet is achieved in the flow-field. As the momentum thickness increases, convective speed of jet disturbance decreased along the stand-off distance. It indicates that downstream propagation time, T_1, increases from Eq. (2.5) which causes the edge-tone frequency to decrease as indicated by Eq. (2.4).

Nozzle lip thickness sensitivity study on edge-tone revealed that edge-tone frequency decreased as nozzle lip thickness increased. Thicker nozzle lip generates more intense reflected waves by interacting between incident upstream propagating waves and nozzle lip wall which results in greater momentum thickness. As the nozzle lip thickness increases convective speed of jet disturbance decreases. It increases the downstream propagation time which results in the reduction of edge-tone frequency as indicated by Eq. (2.4).

The flow-field associated with stand-off distance around the minimum breadth is analyzed. The study pointed out that as the stand-off distance decreases, shear layers generated at both edges of nozzle lip are not impinging on the wedge tip. It resulted in no

vorticity generation from the wedge tip which caused the cessation of the edge tone.

Feedback loop path study on edge-tone illustrated that the upstream propagation lies outside the jet stream since the edge-tone frequencies and amplitude decreased considerably in both methods (8.07 % from secondary coaxial flow method and 6.65 % from plate's inserted method). Both the secondary coaxial flow method and inserted plate method disturbed the upstream propagation significantly that caused the incomplete feedback loop.

In edge-tone suppression study, microjets are injected inside the jet plume to alter the shear layer as well as without microjet injection. Results indicated that microjet injection has the same effect on suppressing the edge-tone like the central insertion tube (*i.e.,* without microjet injection). The mechanism of suppressing the edge-tone for the central insertion tube could be described as follows; by inserting the tube inside the jet plume, it suppresses the shear layer interaction between both the edges of nozzle lip throughout its length *(d/l_t)*. The communication between the shear layers is only possible in the remaining stand-off distance *(i.e. $d/h - d/l_t$)* thereby reducing the flow oscillations. It functions similar to the splitter plate used to control the vortex shedding in cylinder-plate configuration models. It limits the flow-field oscillation which results in the suppression of edge-tone amplitude. This passive control approach is very successful in disrupting the flow oscillations which led to dramatic reductions in the edge-tone amplitude (17 dB) when a central insertion tube of length, d/l_t = 0.375 is introduced into the jet plume having Mach number of 0.87 87 or its length is 30% of the stand-off distance between the nozzle exit and edge tip.

6.2 Future Work

The present investigation is limited to fewer parameters but still more study need to be done to answer many unanswered raised questions. Although some important findings are made, these questions are:

- What is the effect of third dimension on edge-tone characteristics?
- Is there any correlation between the minimum breadth and the stability of shear layer of the jet? Same applied to mode switching in 180^{o} wedge angle compared with 20^{o} and 60^{o} cases.
- Derive any correlations or criterion to reduce edge-tone?

REFERENCES

[1] Stanek, M.J., Raman, G., Ross, J.A., Odedra, J., Peto, J., Alvi, F., and Kibens, V., "High Frequency Acoustic Suppression – The Role of Mass Flow and the Notion of Superposition," *8th AIAA/CEAS Aeroacoustics Conference and Exhibit,* Colorado, June 17-19, 2002.

[2] Andronow, A.A., Chaikin, C.E., "Theory of Oscillations," Princeton Univ. Press, New Jersey, 1949.

[3] Stoker, J.J., "Nonlinear Vibrations in Mechanical and Electrical Systems," Interscience Publishers, Inc., New York, 1950.

[4] Woolley, J.P., and Karamcheti, K., "A Study of Narrow Band Noise Generation by Flow over Ventilated Walls in Transonic Wind Tunnels," Technical Report, TR-73-0503, AFOSR, 1973.

[5] Rockwell, D. and Naudascher, E., "Self-Sustained Oscillations of Impinging Free Shear layers," *Ann. Rev. Fluid Mech.,* Vol. 11, 1979, pp. 67-94.

[6] Zaman, K.B.M.Q., and Hussain, A.K.M.F., "The Free Shear layer Tone Phenomenon and Probe Interference," *Journal of Fluid Mechanics*, 87(349-383), 1978.

[7] Lepicovsky, J., and Ahuja, K.K., "Experimental Results on Edge-tone Oscillations in High Speed Subsonic Jets," *AIAA Journal,* Vol. 23, No. 10, 1985. pp. 1463-1468.

[8] Kwon, Y., "Feedback Mechanism of Low-Speed Edge-tones," *KSME International Journal,* Vol. 12, No. 4, 1998, pp. 701-708.

[9] Ibrahim, M.K., "Experimental and Theoretical Investigations of Edge-tones in High

Speeds," *Journal of Fluid Science and Technology,* Vol. 8, No. 1, 2013. doi: 10.1299/jfst.8.1

[10] Brown, G. B., "The Vortex Motion Causing Edge-tones," *Proceedings of the Physical* Society, Vol. 49, 1937, pp. 493-507.

[11] Karamcheti, K., Bauer, A., Shields, W.L., Stegen, G., and Woolley, P.J., "Some Features of an Edge-tone Flow-field," NASA SP-207, 1969.

[12] Powell, A., "On Edge-tones and Associated Phenomena," Acustica, 3, 1953, pp. 233-243.

[13] Krothapalli, A., Karamcheti, K., Hsia, Y., and Baganoff, D., "Edge-tones in High Speed Flows and Their Application to Multiple Jet Mixing," *AIAA Journal,* Vol. 21, No. 7, July 1983, pp. 937-938.

[14] Lighthill, M.J., "On Sound Generated Aerodynamically. Part I: General Theory," *Proceedings of Royal Society of London,* Series A, Vol. 211, No. 1107, 1952, pp. 564-587.

[15] Uosukainen, S., "Foundations of Acoustic Analogies," VTT Publications 757, VTT Technical Research Centre, Finland, 2011.

[16] Devillers, J.F., Coutier-Delgosha, O., "Influence of the Nature of the Gas in the Edge-tone Phenomenon," *Journal of Fluids and Structures* 21, 2005, pp. 133-149. doi: 10.1016/j.jfluidstructs.2005.07.003

[17] Nonomura, T., Muranaka, H., and Fujii, K., "Analysis of the Relation between Vortex Generation in the Jet Wake and Induced Edge-tone," *Proceedings of the 3rd International Conference on Vortex Flows and Vortex Models,* ICVFM2005, Yokohama, Japan, November 21 – 23, 2005.

[18] Powell, A., "Vortex Action in Edge-tones," *Journal of the Acoustical Society of America*, Vol. 34, No. 2, 1962, pp. 163-166. doi: 10.1121/1.1909164

[19] Curle, N., "The Mechanics of Edge-tones," *Proceedings of Royal Society of London*, Series A, Vol. 216, No. 1126, 1953, pp. 412-424.

[20] Howe, M.S., "Contributions to the Theory of Aerodynamic Sound with Application to excess Jet Noise and the Theory of the Flute," *Journal of Fluid Mechanics*, Vol. 71, Part 4, 1975, pp. 625-673.

[21] Dougherty, N.S., Liu, B.L., and O'Farrell, J.M., "Numerical Simulation of the Edge-tone Phenomenon," NASA Contractor Report 4581, 1994.

[22] Powell, A. and Unfried, H., "An Experimental Study of Low Speed Edge-tones," University of California, Los Angeles, Issue 64, Report No. 49, 1964

[23] Loh, C.Y., "Near Field Trailing Edge-tone Noise Computation," *AIAA Journal*, 2003-0365.

[24] Hardin, J.C., "Solution Comparisons: Category 4," in "Second Computational Aero-acoustics (CAA) Workshop on Benchmark Problems," NASA CP-3352, June, 1997.

[25] Heinemann, H.J., Lawaczeck, O., and Buterfisch, K.A., "Karman Vortices and their Frequency Determination in the Wakes of Profiles in the Sub and Transonic Regime," Sumposium Transonicum II, Goettingen, Germany, Sept. 1975, pp. 75-82.

[26] Bamberger, A., Bansch, E., and Siebert, K.G., "Experimental and Numerical Investigation of Edge-tones," *ZAMM Z. Angew. Math. Mech.*, Vol. 84, No. 9, 2004. pp. 632-646. doi: 10.1002/zamm.200310122.

[27] Holger, D.K., Wilson, T.A., and Beavers, G.S., "Fluid Mechanics of the Edge-tone," *Journal of the Acoustical Society of America*, Vol. 62, No. 5, 1977, pp. 1116-1128.

doi: 10.1121/1.381645

[28] Segoufin, C., Fabre, B., and Lacombe, L., "Experimental Investigation of the Flue Channel Geometry Influence on Edge-tone Oscillations," *Acta Acustica united with Acustica*, Vol. 90, No. 5, September, 2004. pp. 966-975.

[29] Nonomura, T., Muranaka, H., and Fujii, K., "Computational Analysis of Various Factors on the Edge-tone Mechanism using High Order Schemes," *Proceedings of Fluids Engineering Division Summer Meeting and Exhibition*, USA, June 19-23, 2005, pp. 145-153. doi: 10.1115/FEDSM2005-77220

[30] Nonomura, T., Muranaka, H., and Fujii, K., "Computational Analysis of Mach Number Effects on Edge-tone," *36th AIAA Fluid Dynamics Conference and Exhibit*, San Fransico, California, 5-8 June 2006. doi: 10.2514/6.2006-2876

[31] Nonomura, T., Muranaka, H., and Fujii, K., "Computational Analysis of Mach Number Effects on Edge-tone Phenomenon," *AIAA Journal*, Vol. 48, No. 6, June 2010. doi: 10.2514/6.2006-2876

[32] Paal, G., and Vaik, I., "Unsteady Phenomena in the Edge-tone," *International Journal of Heat and Fluid Flow* 28, 2007, pp. 575-586.

[33] Paal, G., and Vaik, I., "Frequency and Phase Characteristics of the Edge-tone," *Acoustics'08,* EAA, Paris, June 29-July 4, 2008, pp. 753-758.

[34] Kaykayoglu, R., Rockwell, D., "Unstable Jet-Edge Interaction, Part 1. Instantaneous Pressure Fields at a Single Frequency," *Journal of Fluid Mechanics*, Vol. 169, August 1986, pp. 125-149.

[35] Vaik, I., Ali, I., Escobar, M., Kaltenbacher, M., Becker, S., and Paal, G., "Two and Three Dimensional Coupling in the Noise Prediction of the Edge-tone," *ICSV14,*

Cairns, Australia, 9-12 July 2007.

[36] Vaik, I., "Flow and Acoustics of the Edge-tone Configuration," Ph.D Thesis, Budapest University of Technology and Economics, Hungary, 2013.

[37] Takahashi, K., Miyamoto, M., Ito, Y., Takami, T., Kobayashi, T., Nishida, A., and Aoyagi, M., "Numerical Analysis on 2-D and 3-D Edge-tones in terms of Aerodynamic Sound Theory," *Proceedings of 20th International Congress on Acoustics,* ICA, Sydney, Australia, 23-27 August 2010.

[38] Anderson, J., Degrez, G., Degroote, J., Dick, E., Grundmann, R., and Vierendeels, J., "Computational Fluid Dynamics An Introduction," third edition, John F. Wendt (Ed.), Belgium, 2009.

[39] Reddy, J.N., "Principles of Continuum Mechanics: A Study of Conservation Principles with Applications," June, 2010.

[40] Krothapalli, A., Baganoff, D., and Karamcheti, K., "An Experimental Study of Multiple Jet Mixing," Stanford University, Stanford, California, JIAA TR-23, 1979.

[41] Scott-Pomerantz, C.D., "The k-epsilon Model in the Theory of Turbulence," University of Pittsburgh, 2004.

[42] Shih, T.H., Liou, W.W., Shabbir, A., and Zhu, A., "A new ke eddy-viscosity model for high Reynolds number turbulent flows – model development and validation," *Computers Fluids,* Vol. 24, No. 3, 1995. pp. 227-238.

[43] Knowles, K., Ritchie, S.A., and Lawson, N.J., "An Experimental and Computational Investigation of a 3-D, l/h = 5, Transonic Cavity Flow," *3rd International Symposium on Integrating CFD and Experiments in Aerodynamics,* USA, 20-21 June, 2007.

[44] Ffowcs-Williams, J.E., and Hawkings, D.L., "Sound Generation by Turbulence and

Surfaces in Arbitrary Motion," Philosophical Transactions of the Royal Society, London, 1969.

[45] Brentner, K.S., and Farassat, F., "An Analytical Comparison of the Acoustic Analogy and Kirchhoff Formulation for Moving Surfaces," NASA Langley Research Center, Hampton, Virginia, 1997.

[46] Hirsch, C., "Numerical Computation of Internal and External Flows," Vol. 2, John Wiley and Sons, 1990. pp. 385.

[47] Buhler, S., Obrist, D., and Kleiser, L., "Near-Field and Far-Field Acoustics of Laminar and Turbulent Nozzle-Jet Flows," *19th AIAA/CEAS Aeroacoustic Conference,* Berlin, Germany. May 27-29, 2013.

[48] Nakamura, Y., Furukawa, T., "Numerical Simulation of Sound Emission from Supersonic Jet," *Notes of Numerical Fluid Mechanics,* Vol. 78, 2001. pp. 350-365.

[49] Sheplak, M., Spina, E.F., "Control of High Speed Impinging Jet Resonance," *AIAA Journal*, Vol. 32, No. 8, 1994. pp. 1583-1588.

[50] Elavarasan, R., Krothapalli, A., Venkatakrishnan, L., Lourenco, L, "Suppression of Self-Sustained Oscillations in a Supersonic Impinging Jet," *AIAA Journal*, Vol. 39, No. 12, 2001. pp. 2366-2373.

[51] Raman, "Supersonic Jet Screech: Half-Century from Powell to the Present," *Journal of Sound and Vibration,* Vol. 225, No. 3, pp. 543-571.

[52] Glass, D., "Effect of Acoustic Feedback on the Spread and Decay of Supersonic Jets," *AIAA Journal,* Vol.6, No.10, 1968. pp. 1890-1897.

[53] Poldervaart, L.J., Wijnands, A.P.J., Moll, L.N., and Voorthuisen, E.J.V., "Modes of Vibration," *Journal of Fluid Mechanics,* Vol. 78, 1976. pp. 859-862.

[54] Shih, C., Alvi, F.S., Ishington, D., "Effects of Counterflow on the Aeroacoustic Properties of a Supersonic Jet," *Journal of Aircraft*, Vol. 36, No. 2, 1999. pp. 451-457.

[55] Alvi, F.S., Shih, C., Elavarasan, R., Garg, G., Krothapalli, A., "Control of Supersonic Impinging Jet Flows using Supersonic Microjet," *AIAA Journal*, Vol. 41, No. 7, 2003. pp. 1347-1355.

[56] Caeti, R.B., and Kalkhoran, I.M., "Jet Noise Reduction via Fluidic Injection," *AIAA Journal*, Vol. 52, No. 1, 2014. pp. 26-32.

[57] Ozono, S., "Flow Control of Vortex Shedding by a Short Splitter Plate Asymmetrically Arranged Downstream of a Cylinder," *Physics of Fluids*, Vol. 11, No. 10, 1999.

[58] Wu, J., and Shu, C., "Numerical Study of Flow Characteristics Behind a Stationary Circular Cylinder with a Flapping Plate," *Physics of Fluids*, Vol. 23, 073601, 2011.

APPENDIX A

Ffowcs-Williams and Hawking's (FWH) Equation Derivation

The continuity and momentum equations of the Navier-Stokes equation can be written as:

$$\frac{\partial \rho}{\partial t} + \sum_{i=1}^{3} \frac{\partial \rho v_i}{\partial x_i} = Q \tag{A1}$$

$$\frac{\partial \rho v_i}{\partial t} + \sum_{j=1}^{3} \frac{\partial \rho v_i v_j}{\partial x_j} = F - \frac{\partial p}{\partial x_i} + \sum_{j=1}^{3} \frac{\partial \tau_{ij}}{\partial x_j} \qquad (i = 1 \ldots 3) \tag{A2}$$

Where ρ is the density, v_i is the i^{th} velocity component, p is the pressure, Q is a mass source (mass per unit volume, per unit time), F is an external force density (force per unit volume) acting on the fluid (such as the gravitational force) and τ_{ij} denotes the elements of the stress tensor. Let us suppose a uniform reference state where the density is ρ_0, the pressure is p_0 and the speed of sound is a_0 and let us notate the perturbations defined as the deviation from this reference state as $\rho' = \rho - \rho_0$ and $p' = p - p_0$. Now, let us take $\frac{\partial(1)}{\partial t} - \sum_{i=1}^{3} \frac{\partial(2)}{\partial x_i} - a_0^2 \sum_{i=1}^{3} \frac{\partial^2 \rho'}{\partial x_i^2}$, thus:

$$\frac{\partial^2 \rho}{\partial t^2} - a_0^2 \sum_{i=1}^{3} \frac{\partial^2 \rho'}{\partial x_i^2} - \sum_{i=1}^{3}\sum_{j=1}^{3} \frac{\partial \rho v_i v_j}{\partial x_i \partial x_j} = \frac{\partial Q}{\partial t} - \sum_{i=1}^{3} \frac{\partial F_i}{\partial x_i} + \sum_{i=1}^{3} \frac{\partial^2 p}{\partial x_i^2} - \sum_{i=1}^{3}\sum_{j=1}^{3} \frac{\partial^2 \tau_{ij}}{\partial x_i \partial x_j} - a_0^2 \sum_{i=1}^{3} \frac{\partial^2 \rho'}{\partial x_i^2} \tag{A3}$$

As ρ_0 and p_0 are independent of time and space, thus with the notation of:

$$T_{ij} = \rho v_i v_j + (p' - a_0^2 \rho')\delta_{ij} - \tau_{ij} \tag{A4}$$

Eq. (A4) is called Lighthill's stress tensor, where δ_{ij} is the Kronecker delta, we conclude to Lighthill's famous equation:

$$\frac{\partial^2 \rho'}{\partial t^2} - a_0^2 \sum_{i=1}^{3} \frac{\partial^2 \rho'}{\partial x_i^2} = \frac{\partial Q}{\partial t} - \sum_{i=1}^{3} \frac{\partial F_i}{\partial x_i} + \sum_{i=1}^{3} \sum_{j=1}^{3} \frac{\partial^2 T_{ij}}{\partial x_i \partial x_j} \tag{A5}$$

This actually the wave equation completed with source terms on the right hand side and it is exact since it is deduced from the Navier-Stokes equations without any assumptions. The terms on the right hand side are called monopole, dipole and quadrupole source terms, respectively. But the applicability is limited due to some assumptions considered for this formulation. They are:

- The sound generated by the fluid flow is radiated into free space
- The sound generated by the fluid flow is weak (i.e. it has negligible interaction of acoustic phenomenon on fluid flow).
- The sound generated by the flow-field is not sensitive to the fluid.

Hence, Lighthill's acoustic analogy is a good option for analyzing the energy that escaped from subsonic fluids as acoustic energy. But it is not a good option for analyzing the change in characteristics of sound generation in transitions to supersonic flow where shock waves are combined with high frequency emission.

FWH analogy is an extended version of Lighthill's analogy which can be applied for bounded flows. It considers the effect of solid boundaries by calculating the source distribution of surface monopole and surface dipole. Hence it is developed from the same

assumptions of Lighthill's analogy. The important point is to manage the interactions of solid surfaces which are directly related in the sound generation, e.g., rotors of helicopters, propellers of airplane, turbofan engines, and turbines. Hence, FWH analogy has significantly more potential applications than the previous analogies and the derivation of the equation is mentioned in detail in Ref [16] Appendix (J). Thus we conclude to famous FWH equation

$$\frac{1}{a_0^2}\frac{\partial^2 p'}{\partial t^2}-\nabla^2 p'=\frac{\partial^2}{\partial x_i \partial x_j}\left[T_{ij}H(f)\right]-\frac{\partial}{\partial x_i}\left[\left(P_{ij}n_j+\rho u_i(u_n-v_n)\right)\delta(f)\right]+\frac{\partial}{\partial t}\left[\left(\rho_0 v_n+\rho(u_n-v_n)\right)\delta(f)\right]$$

------- (A6)

APPENDIX B

The steps to find phase lag value, *p*, can be summarized as follow:

1. Obtain the fluctuation of lateral velocity components along the centerline of jet at *x/h*, specifically; 0, 0.16, 0.33, 0.50, 0.66, 0.83 and 1.
2. Calculate $\theta/2\pi$ value from nozzle exit to other point (*i.e.*, *x/h* = 0 and *x/h* = 0.16) using the autocorrelation code in MATLAB which is reported below.
3. Using Eq. (5.1) calculate the convective speed of jet disturbance.
4. Using Eq. (2.5) calculate the value of downstream propagation time.
5. Similarly, from *x/h* = 0 to *x/h* = 1, calculate the total value of downstream propagation time.
6. Using Eq. (2.5) calculate the value of upstream propagation time.
7. Using Eq. (2.4) calculate the phase lag value.

Autocorrelation for High Speed Jets

% *xcorr* demo

$\underline{r}$ = *xcorr*($\underline{x}$,$\underline{y}$) calculates the cross-correlation of two discrete-time sequences, *x* and *y*. It measures the similarity between *x* and shifted (lagged) copies of *y* as a function of the lag. If *x* and *y* have different lengths, the function appends zeros at the end of the shorter vector so it has the same length as the other.

The true cross-correlation sequence of two jointly stationary random processes, x_n and y_n, is given by

$$R_{xy}(m) = E\left\{x_{n+m}y_n^*\right\} = E\left\{x_n y_{n-m}^*\right\} \tag{B1}$$

where $-\infty < n < \infty$, the asterisk denotes complex conjugation, and E is the expected value operator. *xcorr* can only estimate the sequence because, in practice, only a finite segment of one realization of the infinite-length random process is available.

By default, *xcorr* computes raw correlations with no normalization:

$$\widehat{R}_{xy}(m) = \begin{cases} \sum_{n=0}^{N-m-1} x_{n+m}y_n^*, m \geq 0, \\ \widehat{R}_{yx}^*(-m), m < 0, \end{cases} \tag{B2}$$

The output vector, c, has elements given by

$$c(m) = \widehat{R}_{xy}(m-N), m = 1, 2, ..2N-1. \tag{B3}$$

In general, the correlation function requires normalization to produce an accurate estimate.

```
% signals
Fs = 100000;                % Sampling frequency
T = 1/Fs;                     % Sample time
L = 4096;                    % Length of signal
t = (0:L-1)*T;               % Time vector
s1 = x1;
```

```
s2 = x2; % s1 lags s2 by 0.35s
subplot(2,1,1);
plot(t,s1,'r',t,s2,'b');
grid
title('signals')
% Now cross-correlate the two signals
x = xcorr(s1,s2,'coeff');
tx = [-(L-1):(L-1)]*T;
subplot(2,1,2)
plot(tx,x)
grid
% Determine the lag
[mx,ix] = max(x);
lag = tx(ix);
hold on
tm = [lag,lag];
mm = [-1,1];
plot(tm,mm,'k')
hold off
%
% Note that the lag is only as close as the time resolution.
% i.e. actual = -0.35, calculated = -0.34
S = sprintf('Lag = %5.2f',lag);
title(S)
lag
lag/%(period of edge-tone)
```

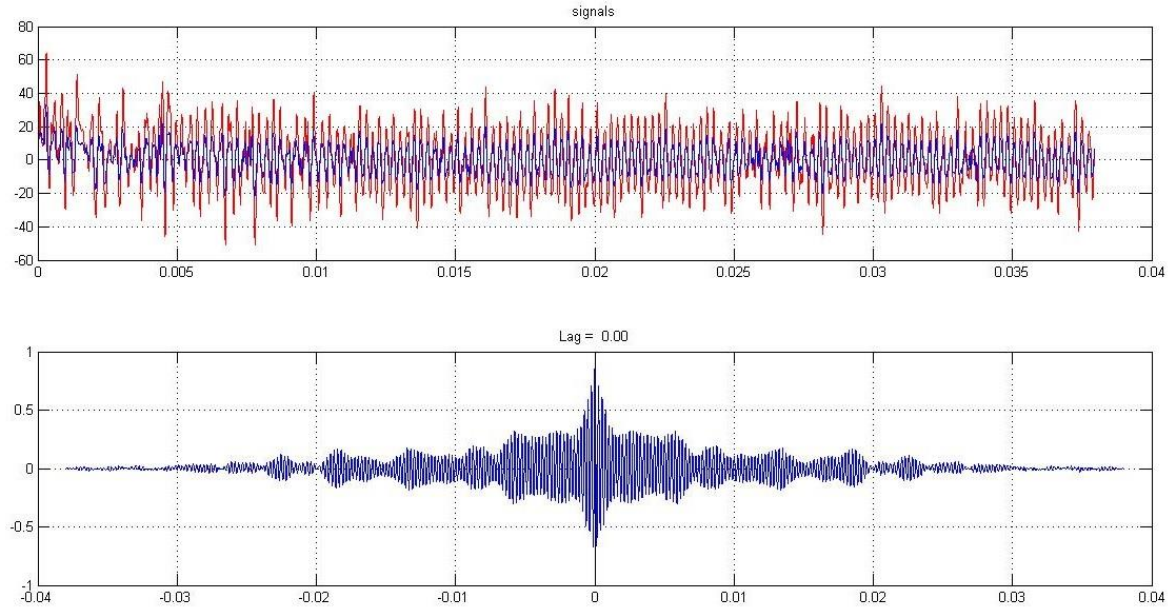

Figure B-1: Phase lag between *x/h* = 0.16 and *x/h* = 0.33 for the case of momentum thickness 0.1 R

Using the above MATLAB code, phase lag between the lateral velocity components at *x/h* = 0.16 and *x/h* = 0.33 is shown in Fig. B-1. The lateral velocity fluctuations of two signals at two different locations are depicted in the top half of the figure in blue and red lines. Then the correlation between the two signals are calculated and it is plotted in the bottom half of the figure. Thus the phase lag between the two signals is calculated using the above code and reported at the center of the figure.

VITAE

Name : Mohamed Yunus Mohamed Ismail

Nationality : India

Date of Birth : 04/06/1989

Email : mohdyunus5@gmail.com

Address : 3/119, Thaikkal Village, Veppanthattai Tk,

Perambalur Dt, Tamil Nadu, India. Pin – 621 105

Academic Background :

- M.Sc. Aerospace Engineering, King Fahd University of Petroleum and Minerals (KFUPM), Dhahran, Saudi Arabia

  (GPA: 3.43 out of 4) May, 2014.

- B.E. Aeronautical Engineering, Anna University, Chennai, India.

  (GPA: 7.9 out of 10) May 2010.

Publications :

- Ibrahim, M.K., **Ismail, M.Y.M.,** and Al-Garni, A.Z., ***"Numerical Investigation of High Speed Jets – Generated Edge-tones,"*** 10^{th} European Fluid Mechanics Conference, Denmark, Sept 14-18, 2014.
- Ibrahim, M.K., **Ismail, M.Y.M.,** and Al-Garni, A.Z., ***"Numerical Study on Parameters Affect Edge-tones in High Speed Jets for both Laminar and Turbulent Flows,"*** Transactions of the Japan Society for Aeronautical and Space Sciences. [To be submitted].

- **Ismail, M.Y.M.,** Ibrahim, M.K., and Al-Garni, A.Z., ***"Computational Analysis of Phase Lag in High Speed Jet Edge-tones and its Suppression,"*** International Journal for Numerical Methods in Engineering. [To be submitted].